ENGINEERING THE MACRO-NANO INTERFACE:

DESIGNING THE DIRECTED SELF-ASSEMBLY AND INTERFACIAL

INTERACTIONS OF GOLD NANOPARTICLE MONOLAYERS

by

MICHAEL L. JESPERSEN

A DISSERTATION

Presented to the Department of Chemistry
and the Graduate School of the University of Oregon
in partial fulfillment of the requirements
for the degree of
Doctor of Philosophy

March 2008

University of Oregon Graduate School

Confirmation of Approval and Acceptance of Dissertation prepared by:

Michael Jespersen

Title:

"Engineering the Macro-Nano Interface: Designing the Directed Self-Assembly and Interfacial Interactions of Gold Nanoparticle Monolayers"

This dissertation has been accepted and approved in partial fulfillment of the requirements for the degree in the Department of Chemistry by:

Darren Johnson, Chairperson, Chemistry
James Hutchison, Advisor, Chemistry
David Johnson, Member, Chemistry
Marina Guenza, Member, Chemistry
Paul Wallace, Outside Member, Geological Sciences

and Richard Linton, Vice President for Research and Graduate Studies/Dean of the Graduate School for the University of Oregon.

March 22, 2008

Original approval signatures are on file with the Graduate School and the University of Oregon Libraries.

An Abstract of the Dissertation of

Michael L. Jespersen for the degree of Doctor of Philosophy

in the Department of Chemistry to be taken March 2008

Title: ENGINEERING THE MACRO-NANO INTERFACE: DESIGNING THE

DIRECTED SELF-ASSEMBLY AND INTERFACIAL INTERACTIONS OF

GOLD NANOPARTICLE MONOLAYERS

Approved: _____

James E. Hutchison

Gold nanoparticles in the 1-2 nm core diameter size regime have generated a great deal of interest due to their size-dependent electronic, optical, and catalytic properties. A number of proof-of-concept experiments have demonstrated that small metal nanoparticles can be integrated into single electron transistors and optical waveguides. Still, reliable incorporation of gold nanoparticles into devices requires practical methods for their assembly on surfaces. Additionally, surface modification methods must be developed in order to control interparticle interactions and nanoparticle-environment interactions for use in sensing and catalysis.

In this research, nanoparticle-substrate interactions were utilized to assemble surface-bound gold nanoparticle monolayers with interesting electronic and catalytic properties. Gold nanoparticles (1.5 nm diameter) with a thiol ligand shell containing

phosphonic acid terminal functionality were synthesized and assembled selectively onto hafnium-modified silicon dioxide substrates through bonding of the terminal phosphonate to Hf(IV) surface groups. By increasing the surface coverage of Hf, it was possible to assemble monolayers of gold nanoparticles dense enough to exhibit nonlinear current-voltage properties across a 5-μm electrode gap at room temperature. Moreover, by taking advantage of the selectivity of this ligand shell for ZnO over SiO_2, small gold nanoparticles were utilized as catalysts for selective growth of patterned, vertical ZnO nanowire arrays.

In addition to engineering nanoparticle-substrate interactions, new surface modification methods were introduced to manipulate the interaction of the as-deposited gold nanoparticle monolayers with the environment. For example, thiol-thiol ligand exchange reactions were carried out on the surface-bound nanoparticle monolayers by immersion in dilute thiol solutions. Contact angle and XPS measurements indicate that the upper, surface-exposed phosphonic acid ligands are replaced by incoming thiol ligands. TEM measurements indicate that nanoparticle monolayers remain surface-bound and are stable to this exchange process, as the average particle size and surface coverage are preserved. As another example, the ligand shell can be partially removed by UV/ozone treatment to expose bare gold cores to the surrounding environment. On metal oxide substrates, this approach activates the particles for room temperature oxidation of carbon monoxide to carbon dioxide.

This dissertation includes both my previously published and my co-authored materials.

CURRICULUM VITAE

NAME OF AUTHOR: Michael L. Jespersen

PLACE OF BIRTH: Newcastle, Wyoming

DATE OF BIRTH: March 11, 1979

GRADUATE AND UNDERGRADUATE SCHOOLS ATTENDED:

> University of Oregon
> University of Wyoming

DEGREES AWARDED:

> Doctor of Philosophy in Chemistry, 2008, University of Oregon
> Master of Science in Chemistry, 2004, University of Oregon
> Bachelor of Science in Chemistry, 2001, University of Wyoming

AREAS OF SPECIAL INTEREST:

> Surface chemistry
> Nanoscale materials
> Chemical self-assembly
> Chemical and structural characterization of surfaces

PROFESSIONAL EXPERIENCE:

> Graduate Research Assistant, Department of Chemistry, University of Oregon, Eugene, Oregon, 2002-2008

> Research Intern, Rohner AG, Pratteln, Switzerland, 2001

> Research Assistant, Department of Chemistry, University of Wyoming, Laramie, Wyoming, 2000-2002

GRANTS, AWARDS AND HONORS:

National Science Foundation IGERT Fellow, 2003-2006

Rebecca Raulins Award for Undergraduate Research, 2001

PUBLICATIONS:

Jespersen, M. L.; Inman, C. E.; Kearns, G. J.; Foster, E. W.; Hutchison, J. E. Alkanephosphonates on Hafnium-Modified Gold: A New Class of Self-Assembled Organic Monolayers. *J. Am. Chem. Soc.* **2007,** *129,* 2903-2807.

Smalley, A. L. E.; Jespersen, M. L.; Johnson, D. C. Synthesis and Structural Evolution of RuSb$_3$, a New Metastable Skutterudite Compound. *Inorg. Chem.* **2004,** *43,* 2486-2490.

ACKNOWLEDGMENTS

Throughout my graduate school experience, I have had the privilege of working with a number of talented researchers. I must first acknowledge my graduate advisor, Professor James E. Hutchison. Jim is a seemingly endless source of ideas and enthusiasm, and I am grateful that I was able to pursue my own ideas with his encouragement. Jim's optimism sometimes leads to wakeboarding injuries. Hopefully I acted with enough urgency when his enthusiasm resulted in a concussion to help preserve his scientific insights for several classes of graduate students to come.

All of my colleagues in the Hutchison laboratory have helped to make my time here an enjoyable one. Evan Foster provided a great deal of mentorship during my first few years in the lab, and I benefited greatly from his creativity. Christina Inman is a dedicated and meticulous researcher, and my work was strongly influenced by her example early on in my graduate career. I enjoyed working on several projects with Greg Kearns and Jennifer Dahl, who were both sources of great advice in the laboratory and instigators of several ill-advised antics at Rennie's Landing and other venues. I was fortunate to collaborate with our guests from Sony in Japan – Shuji Goto, Shinichi Uesaka, and especially Dr. Daisuke Ito, with whom I worked closely during his tenure in our laboratory. I am grateful for his insights and his friendship.

There is not enough space here to thank the rest of the Hutch lab members for making the laboratory a great place to work. Lallie McKenzie has been a good friend and

a helpful coworker with whom I had many productive discussions about my research over the past several years. I must thank Matt Carillo, Sam Lohse, Nick Liebrecht, Pat Haben, and Josh Razink for participating in many fruitful discussions in the Hutch Lab bullpen. Scott Sweeney, Carmen Lisowski, and John Miller all contributed their insights to my work. It is easy to leave graduate school behind, but leaving a great group of co-workers and friends is not.

Much of the surface analysis in this dissertation is the result of my work with the staff of CAMCOR. Steve Golledge trained me on XPS and assisted me in collecting all the TOF-SIMS data discussed in this dissertation. Kurt Langworthy was always helpful in maintaining the TEM and SEM, as well as training me in both these techniques. I must also thank Dr. Mark Engelhard at Pacific Northwest National Laboratory and Dr. Loren Reith at the University of Utah for helping me out when our XPS was out of commission.

Finally, I must thank my family for their endless support throughout graduate school and my entire education. I'm especially happy that Danna decided to move all the way from Chicago to join me for the last couple years of my time in Oregon and for the rest of the journey afterwards.

TABLE OF CONTENTS

Chapter   Page

LIST OF FIGURES

LIST OF TABLES

LIST OF SCHEMES

CHAPTER I

INTRODUCTION:

SELF-ASSEMBLY, INTEGRATION, AND CHARACTERIZATION OF

NANOPARTICLE MONOLAYERS

General Introduction

In 1959, Nobel laureate Richard Feynman delivered his now-famous lecture,

"There is Plenty of Room at the Bottom," in which he stated, "The principles of physics,

as far as I can see, do not speak against the possibility of maneuvering things atom by

atom."[1] Credited with introducing the concept of nanotechnology, Feynman proposed

that researchers could achieve a paramount level of control over matter by assembling

synthetic structures one atom at a time. Perhaps the first practical manifestation of this

concept came in 1981 when Gerd Binning and Heinrich Rohrer demonstrated scanning

tunneling microscopy (STM) for microscopic imaging of surface structures with atomic

scale resolution.[2] These initial experiments led others to eventually direct individual

atoms and molecules with scanning probe tips to build more complex structures.[3-6]

Although we currently do not possess the tools necessary to produce large numbers of

devices and novel structures atom-by-atom in parallel, these experiments have inspired

researchers to assemble structures of nanometer-scale materials in new and useful ways.

Nanomaterials are broadly defined as structures having one dimension below 1000 nm in size.[7] It is in this size regime that materials begin to exhibit unique size-dependent properties that differ from those observed in the bulk and from those observed in individual atoms or molecules. There are thousands of examples of nanomaterials composed of traditional metals, semiconductors, and insulators, and formed into a variety of interesting structures, including nanoparticles,[8, 9] nanowires,[10, 11] nanotubes,[12] and nanoprisms,[13, 14] to name a few. These materials encompass a broad range of sizes, but it is in the 1-30 nm size regime that nanomaterials begin to exhibit properties that vastly differ from those of their bulk counterparts due to quantum effects and as a result of their large surface area-to-volume ratios. The research presented in this dissertation is focused on the development of two-dimensional assemblies of gold nanoparticles, so we will here consider gold nanoparticles as one example of a class of nanomaterials that differs markedly in behavior from the bulk material.

Bulk gold is commonly known for its luster and malleability, as evidenced by its use for centuries in jewelry, coinage, and works of art.[15] It has a high thermal conductivity and melts at approximately 1064 °C.[16] Gold also possesses a very low electrical resistivity and is extremely resistant to corrosion. Consequently, it has been widely used as an ideal contact material in electronics and in microelectromechanical switching components.[17] When the dimensions of gold are reduced to the nanoscale, however, its properties hardly resemble those of the bulk. For example, instead of being non-reactive like bulk gold, nanoscale gold has shown excellent low-temperature

catalytic activity.[18-20] This and other differences in behavior can be attributed to electronic effects and surface effects.

The most well known examples of size-dependent properties of gold nanoparticles are their unique optical and electronic properties. The electronic structure of a gold nanoparticle differs significantly from that of its bulk counterpart, evidenced by the presence of sharp absorbances in the UV-visible spectra of undecagold (Au_{11}) clusters,[21] the observation of broad plasmon resonances in gold nanoparticles over 2 nm in diameter,[22] and the size-dependent change in color observed in solutions of gold colloids.[23] Furthermore, in contrast to the high electrical conductivity the bulk material, a single gold nanocrystal exhibits a size-dependent energetic barrier to single-electron charging that is a result of its extremely small capacitance.[24, 25] This phenomenon, known as the Coulomb blockade to electron transport, will be examined in more detail in the following section because the electron transport properties of gold nanoparticles are one of the primary drivers for study of metal nanoparticle assemblies.

The surface-to-volume ratio of a gold particle increases significantly as the size of a gold nanocrystal is reduced, and the properties of nanoparticulate gold reflect this phenomenon. As the diameter of the particle decreases, the number of gold atoms that reside at the surface of the nanoparticle represent a far greater percentage of the overall composition than they do in the bulk material. The surface is also curved, and the atoms at the surface are not as constrained as they are in the bulk metal. As a result, gold nanoparticles show decreased melting temperature with decreased diameter compared to macroscale gold.[26-28] The nature of the surface will also have a profound impact on the

solubility and interfacial properties of nanoparticulate gold. Modification of nanoparticle surfaces with self-assembled monolayers (SAMs) of ω-functionalized thiols has been demonstrated through direct incorporation during the synthesis and through ligand exchange reactions.[29-33] Depending on the ω-functionality, SAM-functionalized gold nanocrystals are soluble in a variety of common solvents. Terminal functionality can also be incorporated in order to design specific reactivities for analytes in solution and for particular surfaces.[34-36] It is this aspect of gold nanoparticles that makes them interesting candidates for the active components in nanoscale devices fabricated by bottom-up assembly processes.

Bottom-up assembly is often cited as one of the key approaches to accessing the unique properties of nanomaterials, but it has long been a familiar concept in materials synthesis. One needs to look no further than the chemical synthesis industry to realize that organic chemists have been building materials atom by atom for well over a century. Molecule-by-molecule assembly has also seen large-scale implementation over the past several decades, evidenced by the multitude of polymers in common use that are synthesized one monomer unit at a time. Likewise, bottom-up assembly is very important to the fabrication of nanomaterials and nanoscale devices, because structures on the nanometer scale are too small to be manipulated efficiently and in parallel with the tools at our disposal.[7] It is certain that the development of nanotechnology for large-scale applications will rely heavily on the assembly of materials from the bottom up, cluster-by-cluster, and layer-by-layer.

In this chapter, Coulomb blockade will be discussed as one example of the many size-dependent properties of metal nanoparticles that have spawned a significant interest in the development of nanoparticle arrays by self-assembly processes. Some initial single-nanoparticle proof-of-concept experiments, including the self-assembly of single electron transistors, will be discussed. Both the successful operation and the drawbacks of single particle assemblies set the stage for the study of nanoparticle monolayer assemblies. A brief survey of methods for nanoparticle monolayer formation is then provided. Following this overview of nanoparticle assemblies, the components essential to our strategy for nanoparticle monolayer formation are described, including synthesis of functionalized gold nanoparticles, self-assembled monolayer systems important to our approach, the tunable interactions in nanoparticle monolayers derived from our self-assembly technique, and some of the analytical methods used for characterization of nanoparticle monolayers. Finally, this background is followed by a general overview of the remainder of the dissertation.

Coulomb Blockade

The most attractive fundamental feature of single electron devices is the ability to precisely control the movement of a very small number of electrons or even a single electron.[25] Consider the case of a neutral metal nanoparticle with a 1.5-nm diameter core, isolated between two electrical contacts by two tunnel junctions, which can be an insulating ligand shell or a dielectric material (Fig. 1.1(a)). If the gold island is charged

with one electron, an electric field will be produced on its surface, described by the following equation:

$$E = \frac{1}{4\pi\varepsilon_0}\frac{e}{r^2}, \quad (1.1)$$

where e is the charge of an electron, ε_0 is the dielectric constant of the tunnel barrier, and r is the radius of the metal island. Movement of one electron onto the sphere under vacuum results in an enormous electric field on the surface of the particle, approximately equal to 2.6 GVm^{-1}. Consequently, additional electrons are strongly repelled from the particle. If additional energy is put into the system in the form of an electrostatic potential, it is possible to overcome this repulsion to add a second electron, a third electron, and so forth.[24, 25] As a result, the charge versus voltage characteristic of this system should resemble a step function because the total charge on the particle can only increase in single electron increments (Fig. 1.2).

As stated in the previous section, much of the recent interest in metal nanoparticles, specifically gold nanoparticles, stems from their interesting and potentially useful size-dependent electronic properties. Small metal nanoparticles exhibit a barrier to single electron charging that gives rise to nonlinear current-voltage characteristics. This is attributed to the extremely small capacitance (C) of an isolated metal nanoparticle, which can be expressed as a function of the nanoparticle core radius as follows:

$$C = 4\pi\varepsilon_0 r \quad (1.2)$$
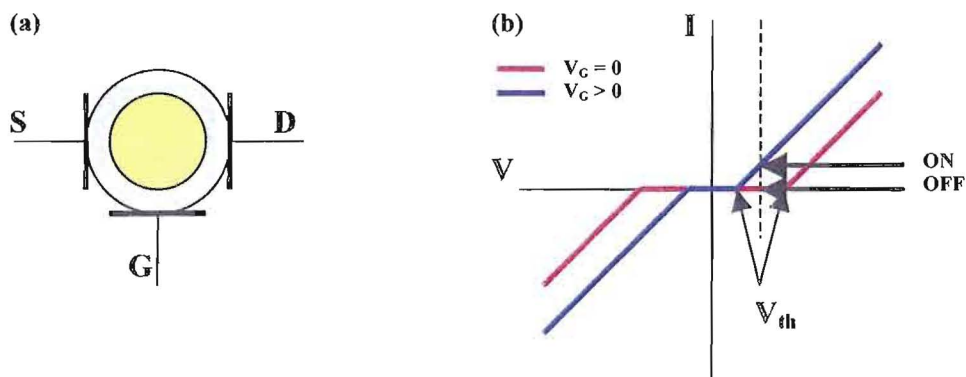
Figure 1.1. Schematic of an ideal nanoparticle SET, with source, drain, and gate contacts. (a) The gold core is isolated from the contacts by two tunnel junctions, which could be a ligand shell, dielectric material, or both. (b) Illustrated nonlinear current-voltage curve for a nanoparticle SET, where application of a positive gate bias lowers the charging energy (and thus the threshold voltage V_T) for the onset of tunneling current. The SET can be switched from the off state to the on state by variation of the gate bias.

Thus, a 1.5-nm gold nanoparticle has a capacitance of 8.3 x 10^{-20} F under vacuum conditions. The energetic barrier to placing an electron onto the isolated gold particle can be expressed as the charging energy (E_C), a function of the capacitance of the particle.

$$E_C = \frac{e^2}{2C} \quad (1.3)$$

The charging energy for an isolated 1.5-nm gold nanoparticle in a vacuum is 1.5 x 10^{-19} J. By comparison, the thermal energy of an electron at room temperature (k_BT) is approximately 4.1 x 10^{-21} J. Consider again the configuration shown in Figure 1.1(a). Since the charging energy of the gold nanoparticle is approximately 36 k_BT, there will be a barrier to single electron charging at room temperature, or Coulomb blockade, persisting until the applied bias overcomes E_C, thus allowing an electron to tunnel onto the particle.
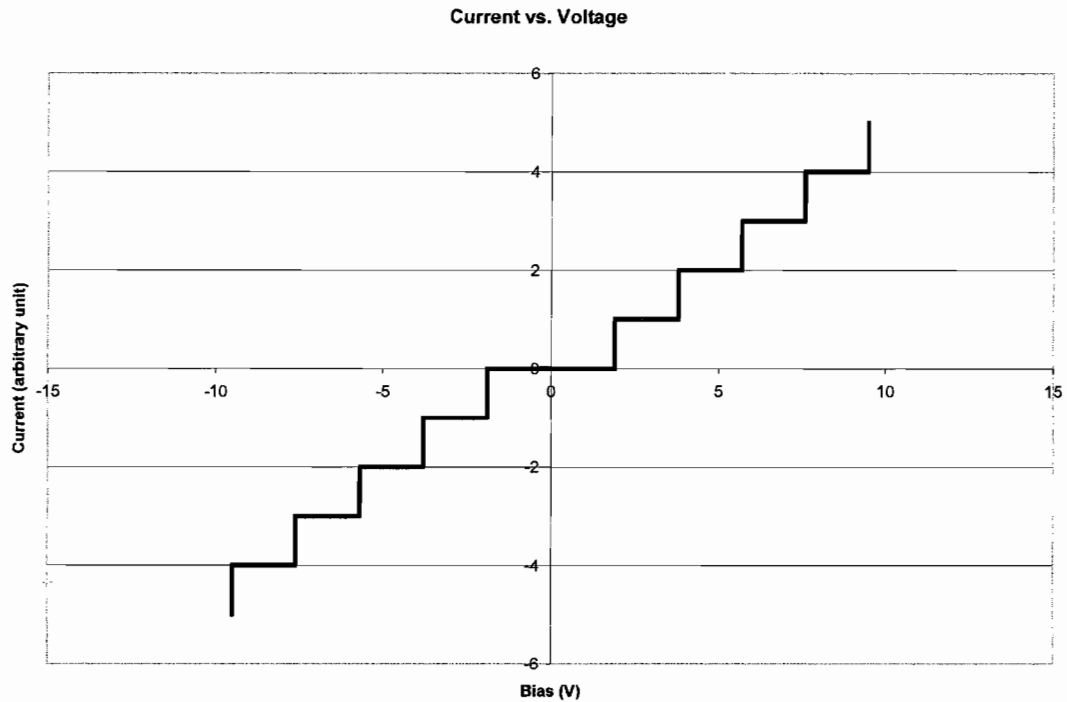
Current vs. Voltage

Figure 1.2. Ideal current-voltage curve for an isolated 1.5-nm gold nanoparticle under vacuum with no thermal energy in the system. The current increases incrementally, in concert with the incremental tunneling events that transfer electrons onto the particle.

To determine the applied bias equal to the charging energy in this system, it is useful to describe the capacitance of the system as a function of the applied bias, as shown:

$$C = qV, \quad (1.4)$$

where q is the stored charge. The amount of charge stored in the capacitor is quantized according to the following relationship:

$$n = \frac{q}{e}, \quad (1.5)$$

where n is the number of electrons. It follows that when $n = 1$ (as is the case when $V = E_C$), q is equal to e. Substitution into equation 1.4 gives the ideal threshold voltage V_{th} for the onset of tunneling in the system:

$$V_{th} = \frac{e}{C} \quad (1.6)$$

This relationship gives an ideal threshold voltage of approximately 1.9 V for a 1.5 nm gold sphere in a vacuum. Adding a third lead as a gate contact to the system allows for manipulation of the capacitance of the particle, thus enabling a reduction in its charging energy. It follows that the reduced charging energy will result in decreased magnitude of the Coulomb blockade regime and new threshold voltage, Vth'.

Applying the aforementioned principles to a 1.5-nm gold nanoparticle in a vacuum should allow for the observation of transistor-like behavior in a single-electron device. Sweeping the bias between source and drain to potentials beyond V_{th} in the absence of a gate potential should result in a current-voltage curve like that shown in Figure 1.1(b), with the onset of current occurring at the ideal threshold voltage. Application of a positive gate bias will reduce the voltage required to match the charging energy, so the onset of current occurs at V_{th}'. The application of a static potential between source and drain allows for switching between on and off states for the device, simply by changing the gate potential.

Studies of Coulomb Blockade. In 1968, Giaever and Zeller published a study on the superconductivity of tin particles embedded in an oxide layer (Fig 1.3).[37] Because there was a relatively thick aluminum oxide layer between the particles and between the Al contacts, the only way for current to flow in the system was by electron tunneling through the oxide and onto the tin particles. These experiments yielded an unexpected result. The authors noted that for particles with an average radius of approximately 7 nm, there was a large current suppression at very low applied biases. In addition, the zero-bias resistance decreased with increasing temperature. Giaever and Zeller concluded that the zero-bias resistance was caused by inclusion of small metal particles with extremely small capacitance within the insulating layer, resulting in a barrier to single electron charging that must be overcome in order to pass current through the system. This initial work has inspired many experiments investigating the current-voltage properties of small metal nanoparticles and a great deal of interest in developing nanoparticle-based devices that exhibit Coulomb blockade.
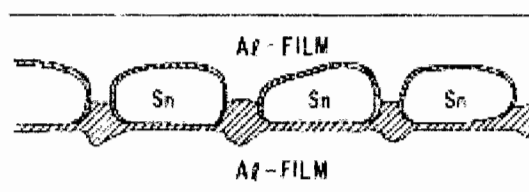
Figure 1.3. Schematic of the system studied by Giaever and Zeller. Tin droplets are embedded in a layer of aluminum oxide, so the only mechanism of current flow through the system between top and bottom aluminum contacts is by tunneling through the oxide layer and onto the tin particles. Reproduced with permission from *Physical Review Letters* **1968,** *20,* 1504-1507. Copyright 1968 by the American Physical Society.

More recent work in this field has relied on scanning probe techniques to address single nanoparticles on conductive substrates. For example, Andres et al. demonstrated room temperature Coulomb blockade through single nanoparticles self-assembled onto dithiol-modified gold.[38] This was one of the first examples of room-temperature electrical characterization of single gold nanoparticles, but the use of an STM tip to address single particles is cumbersome. It is difficult to imagine more complex circuits involving nanoparticle-based components based on scanning probe contacts, and it would be more convenient to fabricate nanoparticle electronic devices using in-plane electrodes.

A single-electron transistor produced by bottom-up assembly has been demonstrated by Klein et al. (Fig. 1.4).[39] Here, gold leads were patterned using a combination of optical and electron beam lithography. The gold leads were functionalized with 1,6-hexadecanethiol to link 5.5-nm CdSe nanocrystals. A number of nanocrystals can be observed between the contacts (Fig 1.4). The contacts were deposited on a degenerately doped silicon wafer, which served as the gate for tuning the charge state of the nanoparticle. This device exhibited Coulomb blockade at 4.2 K, far below room temperature. Low temperatures are required to observe Coulomb blockade in particles of this size because their charging energies are lower than in 1-2 nm particles. By the same self-assembly process described for the CdSe SET, gold nanoparticle-based SETs were fabricated. These devices utilized 5.8-nm gold nanoparticles and exhibited current-voltage behavior consistent with Coulomb blockade at 77 K.[40]
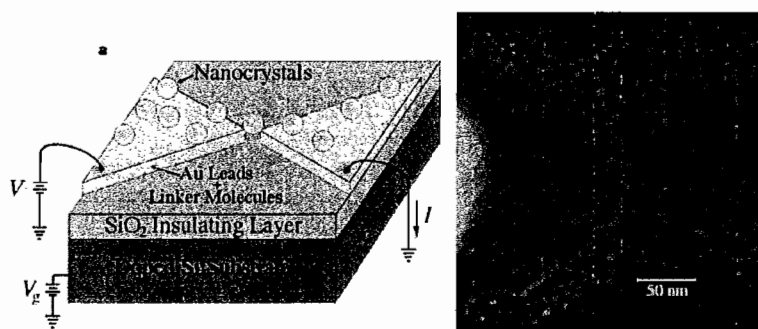
Figure 1.4. Schematic representation of the ideal CdSe SET device structure. (left) A field emission scanning electron micrograph of one device shows a number of 5.5 nm CdSe nanocrystals between the patterned gold contacts (right). Reprinted by permission from Macmillan Publishers Ltd.: Klein, D. L.; Roth, R.; Lim, A. K. L.; Alivisatos, A. P.; McEuen, P. L. *Nature* **1997**, *389*, 699-701, copyright 1997.

The single electron transistors fabricated by the Alivisatos group serve as very useful proof-of-concept experiments. These devices, however, are not useful in large-scale applications for a number of reasons. The CdSe SET was studied at 4.2 K, and the Au SET was characterized at 77 K. These temperatures are far too low for practical device operation. Furthermore, it is not possible to observe Coulomb blockade in nanoparticles with diameters on the order of 5 nm at room temperature because the charging energy is less than the thermal energy. Additionally, the gate voltage required to initiate the onset of current in these devices is greater than 6 V.[39] This is much higher than the maximum bias applied between source and drain within the zero current region for the device. Consequently, such devices could not be used as integrated circuit components because the activation of one such SET would not be enough to drive additional identical devices in sequence. This assembly strategy is also extremely susceptible to failure in the presence of random offset charges in the substrate. Since the active components in these SETs were single nanoparticles, the presence of a trapped

charge in the substrate would disrupt the functionality of the device. Moreover, the working device yield reported for this bottom-up assembly method (approximately 5%)[39] is too low for large-scale, parallel fabrication.

A number of requirements for practical, nanoparticle-based electronics emerge from the drawbacks of these experiments. Small nanoparticles (1-2 nm) will be needed because the charging energy of the nanoparticles must be much greater than the thermal energy at room temperature for practical operation. Two-dimensional assemblies will also be required in order to strengthen the device characteristics in the presence of random offset charges in the underlying substrate, which can be difficult to completely eliminate. Bottom-up assembly strategies will be necessary to reproducibly fabricate very large numbers of devices in parallel and in high yield.

Finally, it should be pointed out that although electronics applications are a strong driving force for the study of nanoparticle assemblies, the development of bottom-up assembly strategies for nanoparticles should broadly apply to the assembly of nanomaterials for a range of applications to be mentioned in upcoming sections of this introductory chapter and the remainder of this dissertation. The following section summarizes a few assembly strategies that have been investigated for the formation of two-dimensional gold nanoparticle arrays.

Assembly of Two-Dimensional Nanoparticle Arrays

Advantages of 2D Assembly. Two-dimensional arrays of nanoparticles offer a number of considerable advantages over their single-particle counterparts. Compared to single-nanoparticle devices, two-dimensional arrays are more robust towared defects such as trapped charges in the device substrate. Random offset charges can be difficult to completely remove, and one trapped charge could function as a gate electrode in a single-particle system, decreasing the threshold voltage for tunneling and taking the particle out of the current suppression regime at low applied potentials.[25] A monolayer of nanoparticles, on the other hand, offers multiple charge transport pathways. In the presence of a few trapped charges that take a small number of particles out of current suppression at room temperature, the device can still function as designed. As long as there is not an uninterrupted low-energy pathway between electrodes arising from charge disorder in the substrate, the current-voltage characteristics will be dominated by those particles exhibiting Coulomb blockade of electron transport (Figure 1.5), and a threshold voltage for the onset of current flow should be observed.

In addition to their enhanced stability toward trapped charge disorder, two-dimensional arrays are also considerably more tolerant of structural disorder than single-particle arrangements or one-dimensional arrays. The presence of a single void in a linear assembly of particles, for example, would certainly prevent electron transport across an electrode gap. Two-dimensional assemblies, on the other hand, can still participate in electron transport, even in the presence of a significant area fraction of voids, due to the large number of continuous transport pathways (Fig. 1.5(b)). Such

voids may arise from polydispersity in the component nanoparticles (Fig. 1.5(c)) or from defects in the crystalline order of the film. In either case, nanoparticle monolayers should maintain their nonlinear current-voltage properties despite various forms of disorder.
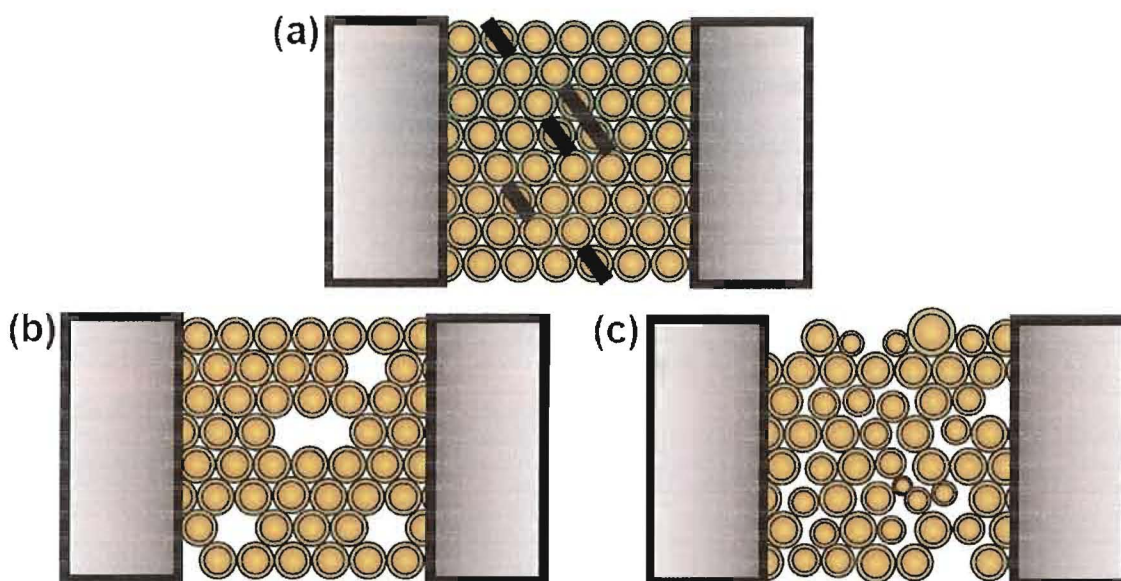
Figure 1.5. Schematic illustrations (top-down) of a 2D array of gold nanoparticles between metal electrodes (a) in a close-packed structure with several particles taken out of current suppression by trapped charges in the substrate (represented by black bars); (b) with voids as structural defects; (c) with a high degree of structural disorder caused by polydispersity in the component nanoparticles. Despite the disorder illustrated in each of the examples, it should be possible to observe nonlinear current-voltage properties in these systems due to the large number of charge transport pathways available.

Because single-particle devices are difficult to reliably assemble and contact electronically, their formation is typically low-yield. In the CdSe SET fabricated by Alivisatos et al., which was assembled by random attachment of CdSe nanocrystals to electron beam-patterned gold electrodes through a dithiol linker, working device yields

(~5%) were impractically low for large-scale production.[39] Other approaches to

contacting nanoparticles are inconvenient and require expensive instrumentation,

including the aforementioned use of an STM tip to manipulate one particle at a time.[38]

Two-dimensional arrays of particles, in contrast, can easily be patterned into arrays that

are 20 nm or less on a side by conventional lithographic methods. Given the powerful

approach of directed self-assembly, it should be possible to use surface chemical

interactions to assemble very large numbers of devices simultaneously while controlling

the positioning of nanoparticles on the target substrate. This presents an attractive and

feasible route to high throughput assembly of nanoparticle-based electronic or optical

devices. To this end, a number of surface modification and nanocrystal assembly

strategies have been developed and studied in recent years.

Langmuir-Blodgett and Langmuir-Schaefer Techniques. Uniform, close-

packed monolayer arrays of 5-nm alkanethiolate-functionalized gold nanoparticles have

been produced by a microcontacting printing technique.[41, 42] This procedure consists of

two steps, the first of which being the self-assembly of a uniform monolayer of

nanoparticles on an air-water interface. The particle film on the water subphase is

transferred intact to a poly(dimethylsiloxane) (PDMS) stamp according to the Langmuir-

Schaefer method (Fig. 1.6). The nanoparticle film is then transferred to a solid substrate

by establishing conformal contact between the PDMS stamp and the target substrate.

Multilayer nanoparticle arrays can be assembled on the stamp one layer at a time,

allowing adjacent layers to be composed of different types of particles, depending on the

application. Well-ordered, centimeter-scale arrays of nanoparticles have been formed by

this approach. Furthermore, patterned monolayers and multilayers of particles have been

successfully demonstrated.
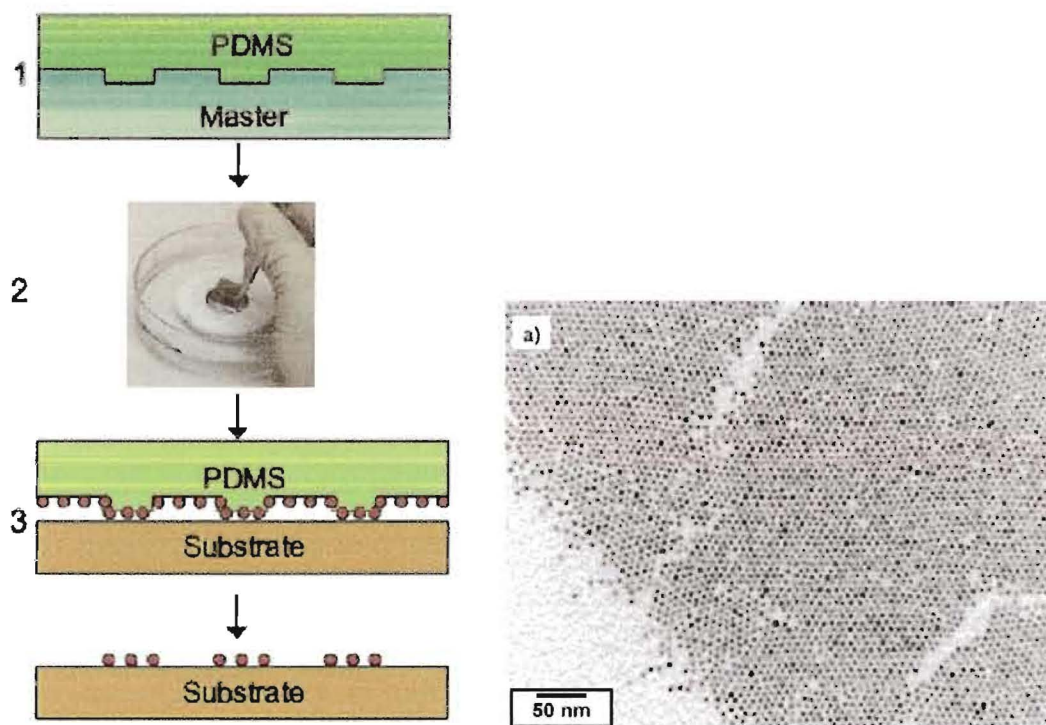
Figure 1.6. Schematic of the microcontact printing and transfer procedure for formation of uniform, close-packed nanoparticle arrays. A Langmuir-Blodgett film of alkanethiolate-protected gold nanoparticles is formed on a water subphase and transferred to the target substrate using a PDMS stamp. This approach produces well-ordered monolayers of nanoparticles, but defects on the macroscale are difficult to avoid, as shown in the TEM image at right. Reproduced with permission from Santhanam, V.; Andres, R. P. *Nano Letters* **2004,** *4,* 41-44. Copyright 2004, American Chemical Society.

One drawback to this technique is the difficulty in achieving defect-free, uniform

arrays on the macroscale. Great care must be taken in the formation of well-ordered LB

films of nanoparticles, and multilayers tend to form at the periphery of these films.

Defects can propagate through the transfer step, and it is common to find relatively large

defects in the crystalline order of microcontact-printed nanoparticle arrays (Fig 1.7).[41, 42] In addition, it is difficult to imagine a large-scale production process for nanoparticle arrays that relies on uniform LB assemblies of particles that extend for several centimeters. The monolayer films of particles reported by Santhanam et al. are based on 5-nm gold cores with an alkanethiolate ligand shell, and LB assembly methods for well-ordered nanoparticle monolayers in this size range have been reported previously.[38] Reports on the formation of close-packed LB films of gold nanoparticles in the 1-2 nm size regime, however, are far fewer.[43] The decrease in van der Waal's forces with decreasing core size can partially explain this difficulty in achieving long-range crystalline order. Even in systems in which ligand interactions favor ordering, several nucleation sites may exist, and it is necessary to apply external driving forces to induce order in small nanoparticle arrays. This has been demonstrated by Brown et al. through the formation of LB films of 1.4-nm amphiphilic gold nanoparticles, requiring multiple compression-relaxation cycles to increase the average grain size of ordered arrays (Fig 1.7).[43] Clearly, formation of well-ordered LB arrays of 1-2 nm gold nanoparticles presents a challenging problem requiring advanced fabrication techniques, with limited degrees of success. While the LB films reported by Brown et al. show crystalline order, there is a significant fraction of voids and dislocation defects that disrupt the continuity of these films.
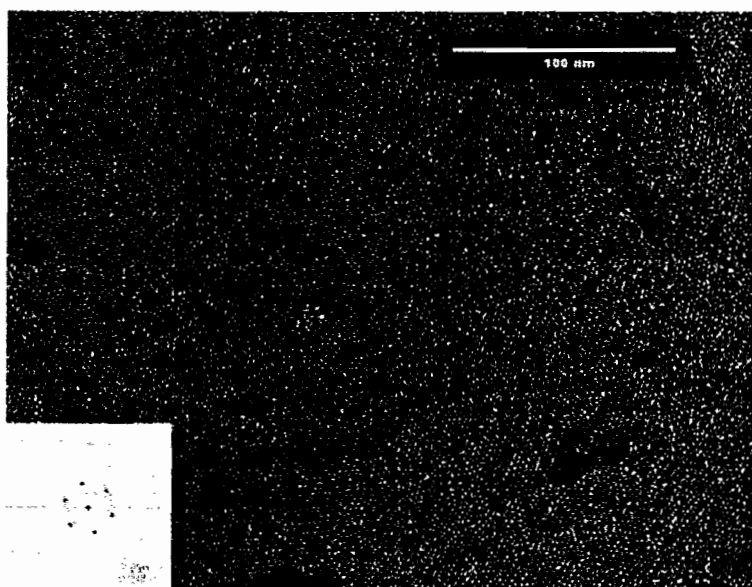
Figure 1.7. TEM image of a LB monolayer of 1.4-nm gold nanoparticles formed in a LB trough after three compression-relaxation cycles. Despite hexagonal close-packed ordering throughout most of the grain shown, several defects and voids are clearly evident. Reproduced with permission from Brown, J. J.; Porter, J. A.; Daghlian, C. P.; Gibson, U. J. *Langmuir* **2001,** *17,* 7966-7969. Copyright 2001, American Chemical Society.

Kinetically-Driven Self-Assembly. More recently, highly-ordered, extended arrays of 2-3 nm alkanethiolate-protected gold nanocrystals have been obtained by addition of excess ligand to a solution of nanoparticles to isolate the soluble particles at the air-solvent interface.[44, 45] Rapid evaporation of the solvent assists the segregation of nanoparticles at the air-liquid interface because the velocity of the interface is faster than diffusion of the nanoparticles in this case. The excess ligand in solution facilitates an attractive interaction between the particles and the air-liquid interface. The net result is the formation of a saturated, two-dimensional solution of nanoparticles at the air-liquid interface, from which nucleation and growth of nanoparticle islands progresses, until adjacent islands coalesce.[44] This ordered, two-dimensional film is deposited onto the

target substrate when the solvent has completely evaporated, leaving nanoparticle monolayers with excellent long-range order over macroscopic dimensions (Fig. 1.8). These monolayers have served as exceptional model systems for the investigation of electron transport across nanoparticle arrays between in-plane electrodes.[45] Despite these advantages, it is required that the target substrate be compatible with the conditions for self-assembly from solution. This strategy also calls for rapid solvent evaporation and may be difficult to reproduce conveniently over macroscopic scales. The presence of excess free ligand is required, which may introduce unwanted impurities in the deposited nanoparticle layer.
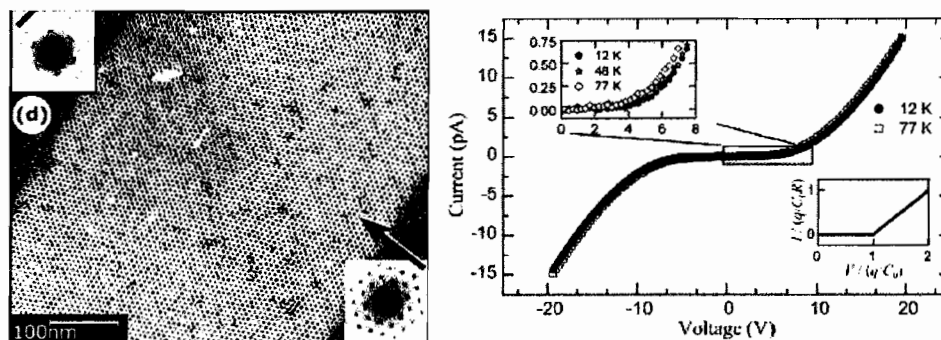
Figure 1.8. TEM image of a high-quality, 2D nanoparticle array formed by kinetically-driven self-assembly from a rapidly evaporating solution of dodecanethiolate-protected gold nanocrystals containing excess free ligand (left). These monolayers serve as exceptionally well-ordered test structures for observation of electron transport in metal nanocrystal arrays with in-plane electrodes (right). Reproduced with permission from Parthasarathy, R.; Lin, X.-M.; Jaeger, H. M. *Physical Review Letters* **2001,** *87,* 186807. Copyright 2001, by the American Physical Society.

Template-Assisted Adsorption of Nanoparticles. Much effort has been directed toward the development of simple bottom-up assembly techniques that use specific surface chemical interactions to guide the assembly of metal and semiconductor

nanoparticles onto patterned target regions on a variety of substrates.[46] Template-assisted

strategies involve the modification of the target solid substrate by mixed SAMs, which

spontaneously guide the assembly of nanoparticles to patterned regions. This strategy for

selective nanoparticle monolayer formation has been demonstrated through the use of

microcontact-printed, patterned SAMs of ω-functionalized thiols (-NH$_2$ or –SH terminal

groups) on gold (Fig 1.9)[47] and through electrochemical modification of organosilane

SAMs on SiO$_2$ with an AFM tip to graft gold clusters onto the modified regions.[48] These

patterned nanoparticle films form as poorly-ordered monolayers because the strong

particle-substrate interaction hinders reorganization, and this method does not allow

precise control over interparticle spacing and monolayer density.
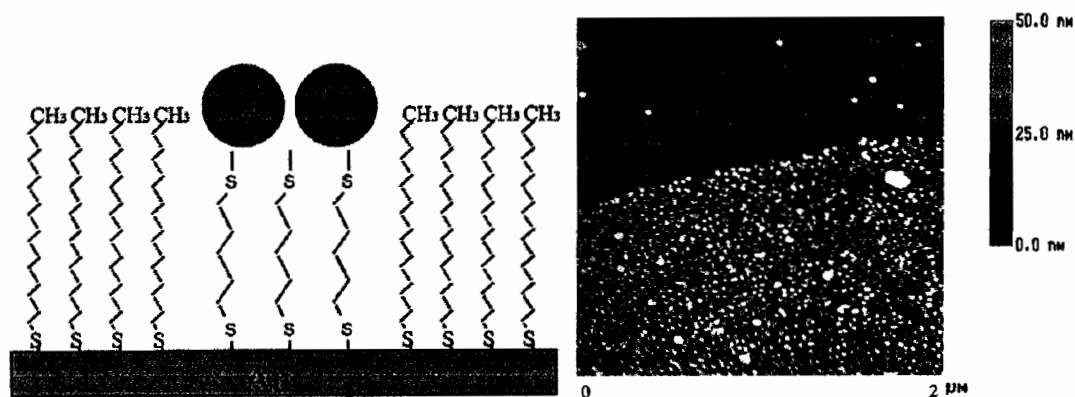
Figure 1.9. Schematic of a patterned, microcontact-printed SAM on gold, with a patterned terminal thiol functionality to direct the assembly of 12-nm gold nanoparticles from solution. The corresponding AFM image of a mixed SAM with adsorbed gold nanoparticles reveals a patterned but poorly-ordered monolayer. Reproduced with permission from He, H. X.; Zhang, H.; Li, Q. G.; Zhu, T.; Li, S. F. Y.; Liu, Z. F. *Langmuir* **2000,** *16,* 3846-3851. Copyright 2000, American Chemical Society.

Covalent Linkage by Ligand-Substrate Interactions. Finally, bottom-up assembly approaches for the fabrication of two-dimensional nanoparticle arrays have emerged based on directed self-assembly, in which the nanoparticle ligand shell contains terminal functionality that forms a covalent linkage with a particular solid substrate.[46] One could envision a broad range of specific surface chemistries that can be utilized to attach nanoparticles to specific substrates. There are many examples in the literature, including selective biorecognition chemistries, such as the adsorption of avidin-functionalized gold colloids onto biotin-modified silicon dioxide,[35] and the incorporation of carboxylic- and phosphonic acids as terminal functionalities in the protecting ligand shells of Au and CdS nanoparticles for covalent attachment to metal and metal oxide surfaces.[49, 50]

Generally, this assembly approach is a simple process for the selective adsorption of nanoparticle films to patterned regions on solid substrates. Since solid surfaces can be patterned with a variety of surface functionalities, it should be possible to direct the assembly of nanoparticles bearing specific functional groups to targeted regions on a variety of substrates. It should also be possible to guide the assembly of different classes of nanoparticles to specific surface patterns using carefully selected surface interactions to obtain complex architectures or mixed nanoparticle systems. The formation of LB films and the use of external driving forces to guide the fabrication of dense nanoparticle monolayers is not necessary for this technique, which instead favors self-assembly from solution. Although this method has not been shown to yield well-ordered nanoparticle monolayers to date, its simplicity makes it attractive for large-scale fabrication of

nanoparticle monolayers. Covalent attachment of nanoparticles to solid substrates through functionalized ligand shells is potentially the most convenient method for assembly of nanoparticle devices that are uniform on a macroscopic scale. Moreover, the bonding of nanoparticles to target surfaces through a ligand shell linker allows for further processing without desorbing the particles.[8] Development of this technique requires careful design of nanoparticles with specific terminal functionalities, while the directed assembly will likely rely on formation of nanoparticle assemblies guided by known surface modification strategies. Our approach to surface-bound nanoparticle monolayer formation is further developed in the next section with a discussion of nanoparticle synthesis and the relevant SAM chemistries.

Nanoparticle Synthesis

Although there are numerous reports of physical methods for the production of gold nanoparticles, including pulsed laser ablation methods[51, 52] and digestive ripening preparations,[53] chemical routes to the preparation of gold nanoparticles have proven to be much more versatile and facilitate the synthesis of products with much narrower size distributions. An important aspect of wet chemical routes to gold nanoparticle synthesis is the ability to incorporate a wide range of stabilizing ligands, which prevent the coalescence of nanoparticles and allow the products to be interfaced in a controlled manner with their environments in solution or on solid supports.

The Turkevich method, first reported in 1951, is one of the most popular chemical routes to the formation of gold colloids.[54] Sodium citrate reduces $AuCl_4^-$ in aqueous

solution to yield gold nanoparticles in the 15-20 nm size range. Excess citrate acts as a stabilizing agent in this case, but few reports of further derivatization of citrate-stabilized nanoparticles with phosphine or thiol ligands exist.[55-57] Consequently, methods to tailor the surface chemistry of these gold nanoparticles for specific applications have been slow to develop. Futhermore, while gold nanoparticles in the 15-20 nm size regime have been suggested as candidate materials for the development of optical waveguides and plasmonics-based devices,[58, 59] the size-dependent electronic and catalytic properties of gold nanoparticles are realized at room temperature in the 1-3 nm size regime. Synthetic access to readily functionalized gold nanoparticles in this size range has progressed rapidly in the past two decades based on the gold salt reduction methods first developed by Turkevich.

Schmid and coworkers first reported the synthesis of a 1.4-nm, triphenylphosphine-stabilized "Au_{55}" cluster in 1981,[60] by reduction of Au(PPh$_3$)Cl using diborane gas at elevated temperatures. This marked a significant step forward in gold nanoparticle synthesis because it provided synthetic access to relatively monodisperse, small (1-2 nm), ligand-stabilized gold nanoparticles. It was later reported that the stabilizing phosphine ligand could be exchanged for a variety of thiols, providing a route to stable, functionalized 1-2 nm gold nanoparticles with tunable solubilities.[29] In 1994, Brust et al. reported a synthesis for gold nanoparticles in the 1-3 nm size range, utilizing a milder reducing agent ($NaBH_4$) in the presence of thiol ligands for the direct functionalization of the product nanoparticles.[30, 31] Furthermore, it was shown that the diameter of the gold cores could be tuned by varying the thiol concentration, giving

synthetic access to a library of thiol-functionalized gold nanoparticles between 1 and 5 nm.[61]

In 2000, the Hutchison lab reported a safer, more versatile synthesis of 1.5-nm, triphenylphosphine-stabilized gold nanoparticles by eliminating the use of diborane gas in favor of sodium borohydride as the reducing agent in a biphasic, modified Brust preparation. This also eliminated the need for rigorously anaerobic conditions because the improved synthesis could be carried out in ambient conditions. A key advantage of this preparation is that the product triphenylphosphine-stabilized nanoparticles are relatively monodisperse intermediates to a seemingly unlimited range of thiol-stabilized gold nanoparticles through ligand exchange reactions, which tolerate a broad range of ω-functionalized thiols.[29, 33]

Ligand Exchange Reactions. The ability to tailor the surface chemistry of nanoparticles is essential to their integration into just about any application. Ligand exchange reactions have been widely used to incorporate a library of alkyl-, aryl-, and ionic thiols into the ligand shells of gold nanoparticles to generate functionalized gold nanoparticles (Fig. 1.10).[32, 33, 62-65] In this research, the organic-soluble triphenylphosphine-stabilized precursors are dissolved in dichloromethane, and the phosphines are exchanged for the water-soluble thiol ligands in biphasic conditions, with 90-200 equivalents of the incoming thiol dissolved in water. The product nanoparticles become soluble in the aqueous phase as the exchange reaction proceeds toward completion. Addition of larger excesses (greater than 300 molar equivalents) of incoming thiol ligand results in decomposition of the nanoparticles.[56] In the case of acidic

incoming thiol ligands like the phosphonic acid-containing thiols used in this research, it

is also important to perform ligand exchange at slightly basic pH because incomplete

ionization of the ω-functional group results in incomplete or slow exchange reactions,

evidenced by the formation of insoluble material as a foamy interphase between the

aqueous and organic fractions. In addition, acidic conditions decompose the PPh_3-

stabilized precursors. In our work, the pH of the aqueous phase was maintained near pH

8 using KH_2PO_4/K_2HPO_4 buffer.[33]

$R =$ -$(CH_2)_nCH_3$ $n = 2, 5, 7, 11, 15, 17$
-p-Ph-OH
-p-Ph-CH$_3$
-p-Ph-Ph
-$(CH_2)_3Si(OCH_3)_3$
-$(CH_2)_nCOOH$ $n = 1, 2, 6, 11$
-$(CH_2CH_2O)_nCH_2CH_2OH$ $n = 1, 2$
-$(CH_2)_2PO(OH)_2$
-$(CH_2)_2NHMe_2^+$ Cl$^-$
-$(CH_2)_2NMe_3^+$ Cl$^-$
-$(CH_2CH_2O)_nCH_2CH_2NMe_3^+$ Cl$^-$ $n = 1, 2$
-$(CH_2)_2SO_3^-$ Na$^+$
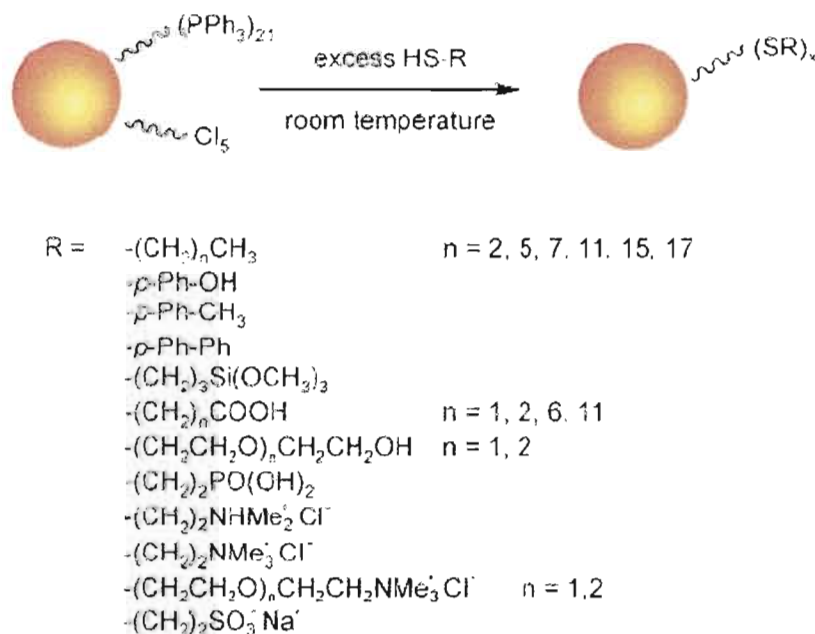
Figure 1.10. Schematic of ligand exchange reactions for PPh_3-stabilized gold nanoparticles, which can incorporate a full range of organic- and water-soluble thiols ligands and tolerate a wide library of ω-functionalities. This approach enables the ready preparation of functionalized gold nanoparticles with tailored surface properties. Reproduced with permission from Woehrle, G. H.; Brown, L. O.; Hutchison, J. E. *Journal of the American Chemical Society* **2005,** *127,* 2172-2183. Copyright 2005, American Chemical Society.

Nanoparticle Purification. Another key aspect of nanoparticle preparation is their purification to generate a monodisperse product free of small molecule contaminantion, including byproducts of the nanoparticle synthesis, residual gold salts, and excess free ligand. Residual free ligand is particularly problematic in formation of nanoparticle assemblies because free ligand in solution competes with functionalized gold nanoparticles for binding sites on target substrates and decreases the surface coverage achievable in both scaffold-directed linear arrays and two-dimensional nanoparticle monolayers formed by directed self-assembly. Previously, gold nanoparticles were purified by gel filtration chromatography, which can be broadly applied to organic- and water-soluble nanoparticles.[33] Water-soluble nanoparticles have also been purified by ultracentrifugation, but this process generally requires at least two centrifugation cycles of at least twelve hours per cycle to reduce free ligand concentration in the supernatant to acceptable levels. Furthermore, the supernatant cannot be completely removed, leaving trace impurities in the product.[33] Gold nanoparticles in this research were purified using a diafiltration procedure applied to gold nanoparticles by the Hutchison laboratory and reported by Sweeney.[66] This serves as the most convenient route to removal of small molecules from solutions of water-soluble nanomaterials.

With the availability of a convenient synthetic route to gold nanoparticles in the 1-2 nm size regime, the ability to tailor their surface properties using ligand exchange reactions, and effective purification strategies for removing excess free ligands, we have the necessary building blocks for nanoparticle assemblies. The following section

discusses how surface properties of these nanoparticles can be used to assemble monolayers of particles and how their various interfacial interactions can be manipulated through careful choice of surface chemistry.

Interfacial Interactions in Nanoparticle Monolayers

There are now a number of well-known syntheses for gold nanoparticles that vary in core size from sub-nanometer clusters to "large" colloids 50 nm or more in diameter. Furthermore, functionalization of these gold nanoparticles has been well studied. Specifically, ligand exchange reactions that tolerate a full range of terminal functional groups have provided synthetic access to a vast library of monolayer-protected nanoparticles. In a sense, the terminal functionality of the ligand shell can be viewed as the mediator between the gold core and its environment in three dimensions. Not only does this tunable end group functionality dictate the solubility of a particular class of particles, but it also governs the interactions of the gold core with surfaces or the gas phase and solution environments. In tandem with the length and composition of the ligand shell, the in-plane interparticle interactions within a nanoparticle assembly can also be manipulated. Figure 1.11 below illustrates the different nanoparticle interfaces that depend on ligand shell thickness and terminal functionality in a one- or two-dimensional arrangement of nanoparticles.
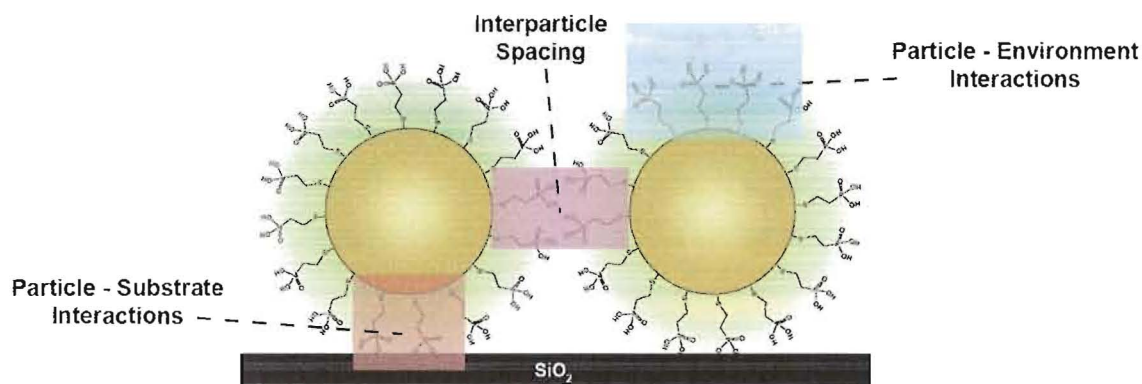
Figure 1.11. Illustration of the tunable interfacial interactions in nanoparticle assemblies. The ligand shell terminal functionality dictates the particle interactions with surfaces and analytes in solution. The ligand shell thickness and terminal group can also dictate the in-plane interactions in an array, especially the interparticle spacing. The ligand shell composition, length, and terminal functional groups all mediate the interactions of the particle with the environment above the plane of the array by passivating the gold core or presenting surface functional groups to the surrounding environment.

Particle-Surface Interactions. As discussed previously, methods for the reliable assembly of nanomaterials onto surfaces is key to their integration into useful device applications by bottom-up self-assembly methods. For example, one-dimensional and pseudo-one-dimensional arrays of nanoparticles have been investigated for use in plasmonic waveguides for optoelectronics applications and as components in nanoelectronic devices by assembly onto biopolymers, including DNA.[36, 67] In these cases, nanoparticles decorated with a ligand shell containing terminal quaternary ammonium functionality are directed onto the negatively-charged, phosphate-containing DNA backbone by electrostatic interactions.

Two-dimensional arrays of particles can also be assembled by utilizing nanoparticle interfacial interactions. Several approaches for two-dimensional assembly have been discussed earlier in this chapter, but it is useful to note a couple examples that

rely on specific particle-substrate interactions. Biorecognition interactions have been utilized to couple avidin-coated colloidal gold particles to biotin moieties on SiO_2-supported lipid bilayers, as demonstrated by Oloffson and co-workers (Fig. 1.12).[35] This approach utilizes 10-20-nm diameter gold nanoparticles and is now well established for the detection of avidin bound to biotin-modified nanoparticles by local surface plasmon resonance measurement. As an introduction to our strategy, Foster et al. demonstrated the directed self-assembly of 1-2 nm gold nanoparticles functionalized with a thiol ligand shell containing terminal phosphonic acid groups onto hafnium-modified silicon dioxide surfaces.[34] This solution self-assembly approach provides ready access to extended gold nanoparticle monolayers that can be targeted to photolithographically patterned regions on an insulating substrate. The strength of this approach lies in its simplicity, and though the nanoparticle monolayers thus formed do not exhibit long-range crystalline order, they are robust due to the strong covalent bond formed between the modified substrate and the phosphonic acid terminal groups. In both examples, the selective chemical interaction of the nanoparticle ligand shell with a modified surface results in the formation of a monolayer of particles bound to the target substrate.

Interparticle Interactions. Interparticle spacing is another aspect of nanoparticle arrays that can be tuned by careful choice of the ligand shell. The length of the ligand shell, its terminal functional groups, and the degree to which the ligand shells on neighboring particles interdigitate will dictate the core-to-core distance in nanoparticle assemblies. This spacing can impact the electronic and optical properties of a
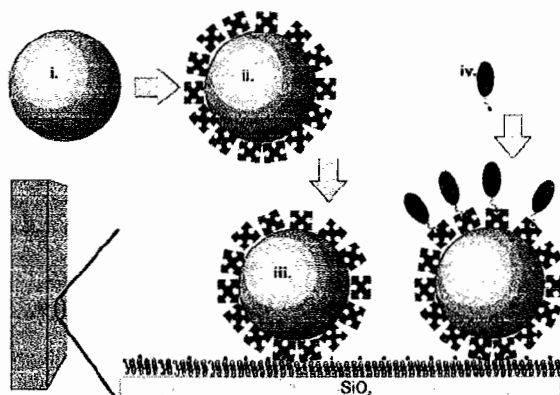
Figure 1.12. Schematic of biorecognition-mediated assembly of colloidal gold nanoparticles. A bare, citrate-stabilized gold nanoparticle (i) is modified with avidin (ii). This modified particle can couple through the avidin shell to biotin moieties (iii) in a biotin-doped lipid bilayer on SiO_2. This immobilized particle layer is also able to bind biotin-modified macromolecules (iv). Reproduced with permission from Olofsson, L.; Rindzevicius, T.; Pfeiffer, I.; Käll, M.; Höök, F. *Langmuir* **2003,** *19,* 10414-10419. Copyright 2003, American Chemical Society.

nanoparticle array. In nanoparticle electronic devices, which operate on the principle of quantum tunneling, the rate at which electrons can tunnel from particle to particle will strongly depend on the interparticle distance. In addition, the degree of plasmon coupling in nanoparticle waveguides is distance-dependent, and the spacing must be carefully controlled in order to realize working devices and study their properties.[58, 59] Control over interparticle spacing in one-dimensional nanoparticle assemblies has been demonstrated by variation of the ligand shell thickness in DNA-templated assembly of 1-2 nm gold nanoparticles.[67] For two-dimensional arrays of nanoparticles formed by Langmuir-Blodgett assembly, increasing the alkanethiol chain length has been shown to aid close-packed ordering of particles while increasing the interparticle spacing. In addition, the ligand shell thickness and composition in these nanoparticle layers has been shown to

impact the electronic properties of arrays of large gold nanoparticles sandwiched between electrodes.[68]

Particle-Environment Interactions. There are relatively few reports on the post-deposition modification of gold nanoparticles in order to tune the interactions nanoparticle monolayers with the environment above the plane of the array. Perhaps the most well-known strategy is that reported for the biorecognition of biotin moieties on avidin-coated gold colloids.[35] Xu et al. also reported the post-deposition modification of bare gold colloids self-assembled onto polymer-templated surfaces by reaction of citrate-capped gold nanoparticles with a range of thiols bearing various terminal functional groups.[69] The water wetting contact angles of these particle arrays are clearly impacted by the choice of incoming thiol ligand. In addition, Liao et al. reported the post-deposition modification of 10-nm gold colloid arrays by thiol exchange reactions to impact only the interparticle spacing.[68] Surprisingly, given the number of articles reporting thiol-thiol place exchange reactions on monolayer-protected gold colloids, thiol-thiol exchange reactions have not yet been employed to tune the interactions of gold nanoparticle monolayers with their surrounding environments.

In order to more thoroughly address the use of surface chemistries to tailor the interfacial interactions of gold nanoparticles, it will be useful to introduce the specific classes of self-assembled monolayers that will be used in this research. By designing the nanoparticle ligand shell to include specific terminal functionalities, it should be possible

to use these bifunctional linkers to participate in formation of two monolayers simultaneously, one on the particle and one on the substrate, while still allowing for subsequent modification of the exposed particle surfaces.

Self-Assembled Monolayers

The formation of self-assembled monolayers (SAMs) on metal, metal oxide, and semiconductor surfaces has been a topic of longstanding interest and the focus of a considerable research effort.[70-72] Though the formation of a single layer of organic adsorbates onto a surface of interest is conceptually simple, the assembly process itself is governed by potentially several interactions, including adsorbate-substrate attachment, intermolecular packing within the adsorbate layer, and interactions of the SAM with the ambient environment. Several adsorbate-surface chemistries have been widely investigated for the tailoring of surface properties on a variety of substrates. Some of the most well-known include: assembly of organic acids (alkylphosphonates and alkylcarboxylates) onto the native oxides of metals such as Ti, Al,[73, 74] and Ag[75]; covalent-polar attachment of thiolates to the metal surfaces of Au,[70, 76] Ag, Pd,[77] Pt,[78] and semiconductor surfaces like InP[79, 80] and GaAs[81]; and monolayer formation mediated by adsorbed water, such as organosilane monolayer assemblies on SiO_2[82, 83] and Au.[84] In this dissertation, we are primarily concerned with the formation of thiol monolayers on gold, especially for the functionalization of gold nanoparticles, and the self-assembly of phosphonic acid monolayers on metal oxides.

Thiol SAMs on Gold. Self-assembled monolayers of organothiolates are the most widely studied class of monolayers, and their assembly has been researched on a broad range of materials, including the surfaces of semiconductors[79-81] and, most notably, the coinage metals (Au, Ag, Cu).[70, 76, 85] Monolayers of organothiols and disulfides are commonly formed by immersion of a freshly evaporated metal surface into a solution of thiol, and a full range of ω-functionalized thiols can be incorporated, enabling the modification of metal surfaces with any surface functionality. We have already discussed gold-thiol SAM chemistry as it relates to our research, specifically in the functionalization of gold nanoparticles with thiol SAMs bearing a wide range of terminal functional groups.

Phosphonic Acid SAMs on Metal Oxides. Alkylphosphonic acids have been shown to assemble readily onto the surfaces of several metal oxides by strong covalent bonding interactions. Due to this stability, thin monolayers of organic acids have been utilized for corrosion inhibition, attachment of bioactive molecules to metal oxides for sensing applications,[86-88] linking of polymers to inorganic templates,[89] modification of dielectric materials in organic thin film transistors,[90] tuning of the ferromagnetic properties of semiconducting materials,[61] and functionalization of metal oxide nanoparticles.[91]

In contrast to monolayers of alkoxysilanes, which assemble as well-ordered islands due to cross polymerization prior to covalent attachment onto metal oxide surfaces,[82, 83] phosphonic acid monolayers assemble randomly onto metal oxides through

covalent bonding of the phosphonic head group and only exhibit ordering after the grafting density of molecules to the surface has reached a threshold value. Continued adsorption of phosphonic acids increases the total van der Waal's interactions between adjacent alkyl chains.[92] Like monolayers of alkanethiols, well-ordered long-chain alkanephosphonic acids demonstrate considerable stability due to the significant van der Waal's interactions between adjacent alkyl chains, giving rise to minimal contact angle hysteresis under a range of pH conditions and preventing the diffusion of aqueous ions to the substrate, thereby imparting corrosion resistance to the underlying metal oxide.[93]

The nature of the bonding interaction between the phosphonic acid head group and metal surfaces or metal ions has been investigated in order to determine whether the phosophonate moiety binds in a bidentate fashion, where both P-O-H groups bind to the metal, or in a tridentate fashion, where the P=O moiety is interrupted to give a P-O-M bond upon elimination of water. Crystal structures of bulk tetravalent metal phosphonates and phosphates show a tridentate bonding configuration exclusively.[94] On metal oxide surfaces, tridentate bonding has been observed through XPS analysis, in which the P=O contribution to the O 1s peak diminishes upon phosphonic acid monolayer assembly.[95] This shift has only been reported on TiO_2,[95] whereas the P=O contribution to the O 1s signal is still observed after phosphonic acid monolayer assembly on Al_2O_3 and Ta_2O_5, indicating a bidentate bonding configuration.

Tetravalent metal cations have been utilized to direct the assembly of phosphonic acid monolayers and multilayers on phosphonate-primed SiO_2, planar gold, and germanium.[94, 96-101] In these cases, a gold, silicon dioxide, or Ge substrate is modified

with a thiol or siloxane monolayer containing a phosphonic acid tail group, upon which a monolayer of Zr(IV) or Hf(IV) cations is self-assembled from solution. Alternating layers of bisphosphonic acids and metal cation species can then be assembled iteratively to deposit multilayers of bisphosphonic acids with metal cation interlayers. One important surface modification technique that has followed from studies of bisphosphonic acid–metal cation multilayer structures is the direct functionalization of silicon dioxide surfaces with tetravalent metal cation species. This method was first reported by Hong et al. in a paper describing the assembly of ordered zirconium 1,8-octanediylbisphosphonate multilayers on zirconium-primed Cab-O-Sil, a high surface area form of silica.[97] It was determined that the multilayers formed by this approach were slightly more well-ordered than those derived from a phosphonate-containing siloxane monolayer as the primer. Studies utilizing hafnium(IV) as a primer layer on Cab-O-Sil have also shown this to be an effective phophonate anchoring technique.[102] This work was extended to planar silicon dioxide substrates by Page and coworkers in a report describing the assembly of hafnium 1,10-decanediylbisphosphonate multilayers on SiO_2.[101] Similar to studies on Cab-O-Sil, multilayers assembled on hafnium-primed SiO_2 were of better quality than those self-assembled onto a primer layer of 3-(hyroxysilylmethyl)propanephosphonic acid. In both of the aforementioned studies, the silicon dioxide surface is modified in aqueous solution of $ZrOCl_2$ or $HfOCl_2$, resulting in a thin hydrous hafnium (or zirconium) oxide film.

Direct modification of planar silicon dioxide substrates with thin layers of zirconium oxide or hafnium oxide by self-assembly from solution offers a number of advantages for advanced materials assembly strategies. In addition to the assembly of

multilayered optical materials,[101, 102] the metal ion layer can be utilized to direct the assembly of bifunctional molecules containing a phosphonic acid head group and a tail group presenting a different functionality. In addition, the hafnium or zirconium layer can be patterned by photolithography for more sophisticated self-assembly schemes. This has been demonstrated by Foster et al. in a report describing the directed self-assembly of gold nanoparticles derivatized with 2-mercaptoethylphosphonic acid (2-MEPA) on hafnium-patterned SiO_2. In this case, gold nanoparticles are stabilized by a thiol monolayer containing a phosphonic acid tail group, which serves as a linker to the hafnium(IV)-modified substrate.[34] This self-assembly strategy is the basis for the research presented in this dissertation.

Orthogonal Self-Assembly Schemes. The development of SAM chemistry has yielded a number of well-described systems that assemble selectively on specific types of surfaces. Selectivity in formation of these molecular assemblies, in tandem with a wide variety of available surface patterning techniques, affords the opportunity for a number of sophisticated self-assembly schemes. In particular, a surface with selectivity for one type of adsorbate can be patterned with a different material that has selectivity for a second type of adsorbate. Based on this configuration, a substrate can be immersed in a solution containing two different adsorbates, or a single bifunctional adsorbate, to simultaneously assemble two different monolayers from a single solution (Fig. 1.13). Several examples of these advanced self-assembly schemes have been reported,[103-105] and these systems show promise for use in molecule-based sensors and molecular electronics.

Based on the combination of rationally-designed nanoparticle building blocks and selective surface chemistries of well-known classes of self-assembled monolayers, we have developed strategies for designing the directed-self assembly and interfacial interactions of gold nanoparticle monolayers. In order to fully study nanoparticle monolayers and their surface properties, a range of characterization techniques are necessary. The next section describes some of the most commonly used analytical methods in our research.
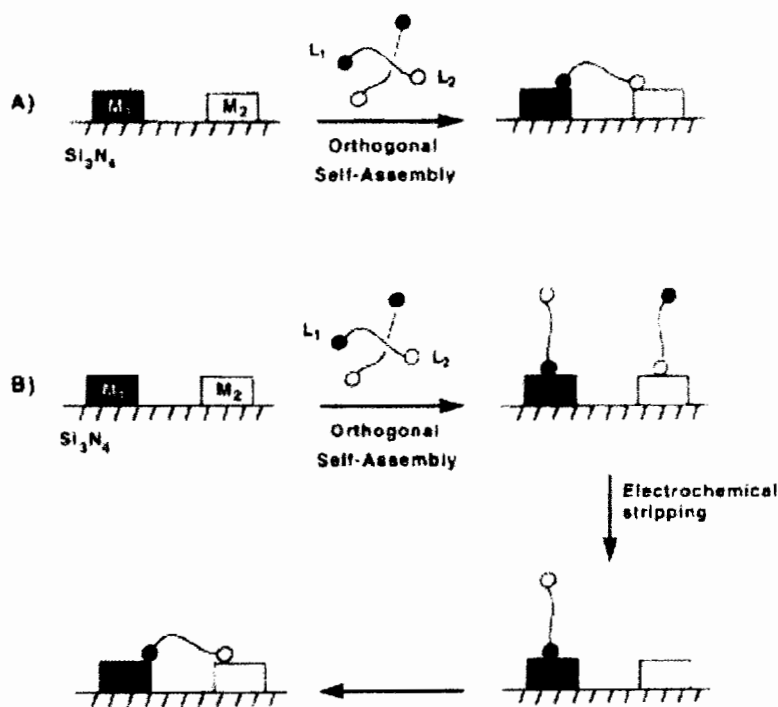
Figure 1.13. Orthogonal self-assembly schemes utilizing bifunctional (L_1-L_2) adsorbates, with each functionality having selective affinity for a different substrate functionality (M_1 or M_2). Reproduced with permission from Gardner, T. J.; Frisbie, C. D.; Wrighton, M. S. *Journal of the American Chemical Society* **1995,** *117,* 6927-6933. Copyright 1995, American Chemical Society.

Characterization of Nanoparticle Monolayers

One of the principal challenges in chemical modification of surfaces and self-assembly of nanostructures is characterizing the products. Since surface chemical processes are generally confined to two dimensions on a single solid substrate, the products of surface modification processes are present in very small amounts. Structural characterization of nanostructures (such as 1-2 nm metal nanoparticles) is also a difficult problem because the physical dimensions of the materials challenge the limits of even the highest-resolution imaging techniques available. It is almost always necessary to utilize several surface analytical techniques in tandem with high-resolution microscopic methods in order to gain a sound understanding of the products from self-assembly processes and surface modification chemistries.

Surface composition analysis of nanoparticle monolayers usually involves X-ray photoelectron spectroscopy (XPS) to obtain information about the elemental composition of the top few surface layers. This analysis can often be refined somewhat by the use of time-of-flight secondary ion mass spectrometry (TOF-SIMS), which yields a wealth of information about surface bonding arrangements and the mass fragments present in the uppermost molecular layers. Structural analysis of nanostructures generally relies on use of transmission electron microscopy (TEM) and scanning electron microscopy (SEM). Contact angle goniometry, as a simple qualitative method, can serve as a rapid assessment of the free energy of surfaces and allows rapid screening of the effectiveness of surface modification chemistries.

X-Ray Photoelectron Spectroscopy. X-ray photoelectron spectroscopy (XPS) is perhaps the most widely used surface analytical method for determining sample composition. Also known as electron spectroscopy for chemical analysis (ESCA), it is popular due to its high information content and its ability to accommodate a very wide range of samples, from planar substrates to powders. In the basic XPS experiment, a sample is placed in a vacuum environment and then irradiated with x-rays of a known wavelength. Energy transfer from the incident x-rays to core level electrons in the sample results in the emission of photoelectrons from the surface region, which can be separated by their kinetic energy and counted with a detector. The measured kinetic energy of the emitted electrons is related to the binding energy inherent in their atomic and molecular environments, the energy of the x-ray source, and the work function of the instrument.[106, 107] The number of electrons counted at a particular binding energy is directly related to the concentration of the type of atom from which those electrons originated. The sampling depth of a typical XPS experiment is approximately 70-100 Å, or the topmost atomic layers of the surface. Because of this surface sensitivity, XPS is well-suited for the characterization of self-assembled monolayers and other thin films.

The most basic XPS experiment will provide a quantitative description of the relative concentrations of all the elements present in a particular sample (except H and He). In general, the area under the most intense peak for each element is measured and normalized utilizing a relative sensitivity factor that depends on the instrument model and is determined from elemental standards.[106, 107] (It is important to choose the most intense

peak for a given element that does not overlap or interfere with peaks from other photoelectrons of similar binding energies emitted from different elements.) These normalized areas are then used to calculate the relative atomic concentrations of each element in a given sample. This simple experiment does not take into account the increased scattering of emitted photoelectrons with increased sampling depth.[106] As a result, the number of photoelectrons escaping from elements residing deeper in the sample is attenuated. Consequently, the overall compositions calculated by this approach are not completely accurate. Still, this method is useful for comparing similar samples to assess the thickness and quality of a thin film. Figure 1.14 shows a sample XPS spectrum from a silicon dioxide substrate modified with a monolayer of hafnium(IV) oxide. Some of the peaks from oxygen, carbon, hafnium, and silicon are noted.
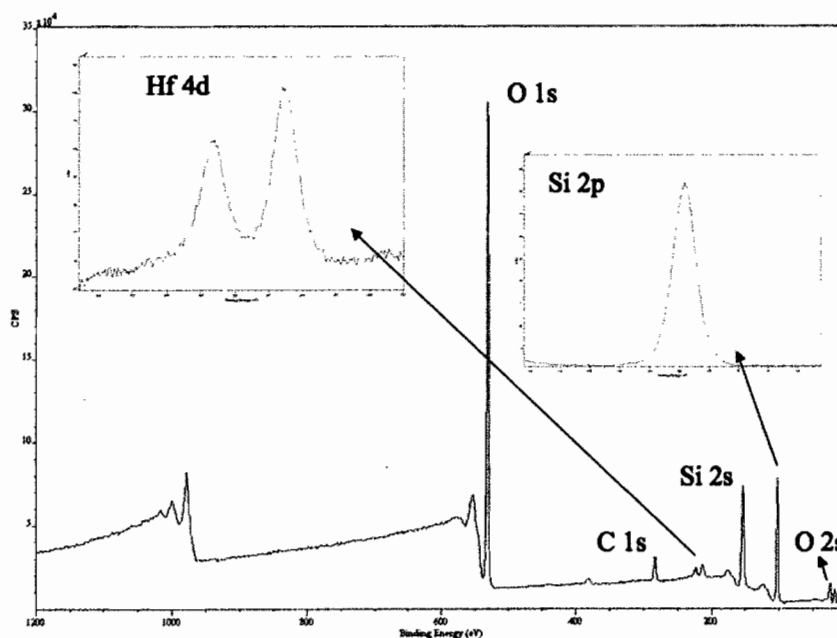
Figure 1.14. XPS spectrum of hafnium-modified thermal SiO_2. Characteristic peaks for oxygen, carbon, silicon and hafnium are shown. The two peaks used for quantitative analysis (Hf 4d and Si 2p) are shown as region scans collected using 0.2 eV steps and 300 ms dwell time.

Time-of-Flight Secondary Ion Mass Spectrometry. Time-of-flight secondary ion mass spectrometry (TOF-SIMS) is an analysis technique that utilizes a primary ion beam to bombard the sample surface, thereby generating secondary elemental or cluster ions that are drawn away from the surface by an electric field and mass analyzed. The primary ion beam commonly consists of O_2^+, Cs^+, or Ar^+ ions, which upon impact, generate a series of collisions in the surface region of a solid sample.[108, 109] A small part of the momentum from the collision cascade may be redirected toward the surface, resulting in the ejection of atomic and molecular fragments from the topmost layers of the surface. The ionized portion of these ejected secondary fragments provides the signal for SIMS.[109]

The most straightforward SIMS experiment presents the secondary ion intensities as a function of the mass of secondary ions accepted by the spectrometer. The mass spectrum thus obtained gives a description of the mass fragments present in the top monolayer of the surface. The mass spectrum for the surface layers can also be collected as a function of position on the surface to generate a SIMS image, which is an especially useful measurement technique for patterned surfaces.[109] Both spectral and imaging modes are known as *static* SIMS techniques. While SIMS is inherently a destructive technique, if a low primary ion flux is used, then it can be shown statistically that no point on the surface layer would be impacted by primary ions more than once.[108, 109] In this case, spectral data can be collected on a timescale much shorter than the lifetime of the surface layer, and the surface is said to be static on the timescale of the measurement. The SIMS

spectra thus obtained can be reasonably assumed to represent the top 1-2 nm of the surface region.

In addition to causing the ejection of mass fragments from the surface layer, the primary ion beam can also be used to sputter the target sample. Sputtering can be used to continuously expose a new surface for SIMS measurement up to a few micrometers deep into the sample, thus enabling the construction of a profile of elemental or cluster concentrations as a function of sputter depth.[108, 109] Depth profiling SIMS, or *dynamic SIMS*, has found wide applications in materials science as a means of characterizing the layer structure of devices and multilayered materials.

Unlike XPS, which is an excellent technique for quantitative analysis of surface compositions, TOF-SIMS does not allow for accurate quantification of surface species. The detection sensitivities for different elements in a single sample and for the same element in different samples vary over several orders of magnitude.[108] Still, semi-quantitative analyses are possible if standards of known composition are employed. TOF-SIMS offers numerous advantages, including excellent sensitivity in the ppb range for most elements, excellent resolution that allows the user to distinguish different isotopes of the same element, and the capability to monitor molecular ions in order to gather chemical bonding information from the topmost surface layers.

Transmission Electron Microscopy. Transmission electron microscopy (TEM) is an indispensable technique for characterizing the size and structure of nanomaterials. It is the most direct method for observation and imaging of nanoparticles and their assemblies. The details of the basic TEM experiment are well-known and have been

described elsewhere,[110] but it is important to focus on those aspects of this analysis technique that apply to characterization of nanoparticle monolayers in our research. Specifically, the choice of TEM substrates and the image analysis methods employed in this work are unique to the Hutchison laboratory.

Most important to analysis of surface-bound nanoparticle monolayers studied in this work is the choice of substrate. Since the substrate of choice for nanoparticle monolayer deposition described in this disseration is thermally-grown silicon dioxide anywhere from a few hundred Angstroms to a few micrometers thick, it is preferred that any TEM analysis utilize the same substrate so that surface treatments and assembly methods can be accurately assessed. Recently, silicon dioxide TEM grids have been developed in our laboratory.[111] The substrates consist of an ultrathin silicon wafer with a thermal oxide layer, which have been etched completely through on one side, leaving a pattern of electron transparent silicon dioxide windows (Fig. 1.15). One of the advantages of this TEM substrate is that it can be treated in the same manner as silicon wafer substrates (including solution processing, plasma treatment, thin film deposition, etc.).

Image analysis techniques are another important consideration for obtaining reliable information from TEM. Typically, a large number of images from different regions on the TEM substrate must be acquired if possible in order to reduce user bias and obtain accurate size analyses. In order to measure nanoparticle sizes from such large
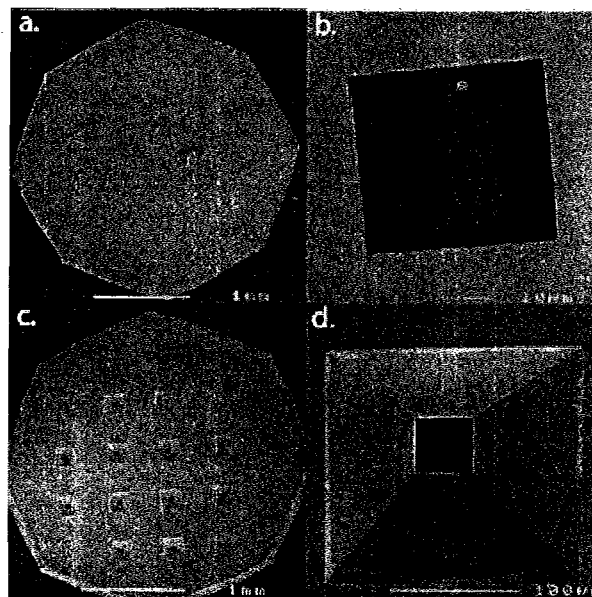
Figure 1.15. SEM images of SiO$_2$ TEM substrates used for structural analysis of gold nanoparticle monolayers. The substrate consists silicon dioxide windows on one side (a,b), and a patterned, selectively etched Si substrate on the underside (c,d). Reproduced with permission from Kearns, G. J.; Foster, E. W.; Hutchison, J. E. *Analytical Chemistry* **2006,** *78,* 298-303. Copyright 2006, American Chemical Society.

samples, software is employed. This requires digital manipulation of images, and care should be taken to avoid over-manipulating a digital image to the point that it no longer accurately represents the original. This is usually accomplished through visual inspection and comparison of the digitally manipulated image to the original scanned image at each step in image processing. In this research, we utilized a series of processing steps to reduce background noise from the substrate and increase the contrast between the nanoparticles and the background. We first automatically adjust the brightness and contrast of the image. Then, a series of filters are used to maximize the contrast. A Gaussian blur removes the granular background noise, and an unsharp mask is used to separate nanoparticles from the smoothed background. The grayscale image is then

converted to a binary image using a threshold filter. We erode the binary structures by one pixel to remove residual single pixel noise and then dilate the structures by one pixel to return them to their original sizes (Fig. 1.16). The particles are then analyzed to obtain average core size and size distribution. In bulk samples of nanoparticles dropcast onto TEM substrates, it is necessary to remove nanoparticles with a circularity factor below 0.85 because drying effects result in the formation of large, irregularly shaped aggregates. In the case of gold nanoparticle monolayers studied in this dissertation, we do not filter the nanoparticles based on circularity because the surface-bound particles generally do not aggregrate, and any observed aggregation is important to consider in assessment of our assembly conditions.

Scanning Electron Microscopy. Scanning electron microscopy (SEM) is a valuable tool for analysis of surface structures and nanomaterials because it provides a wealth of information about surface topography and gives lateral resolution down to a few nanometers. Because electron transparency is not required, the user is not limited to extremely thin specimens as in TEM, but the resolution is not as high.[110] In the SEM experiment, an electron beam is focused on the specimen. The impact of the beam incident on the specimen generates a variety of secondary electron (auger electrons, backscattered electrons, etc.), photon emissions (X-rays, visible photons, etc.), and other radiation (heat), which can be amplified and detected.[112] A strong collected signal produces a bright spot on the detector, while a weak signal produces a dark spot. Several
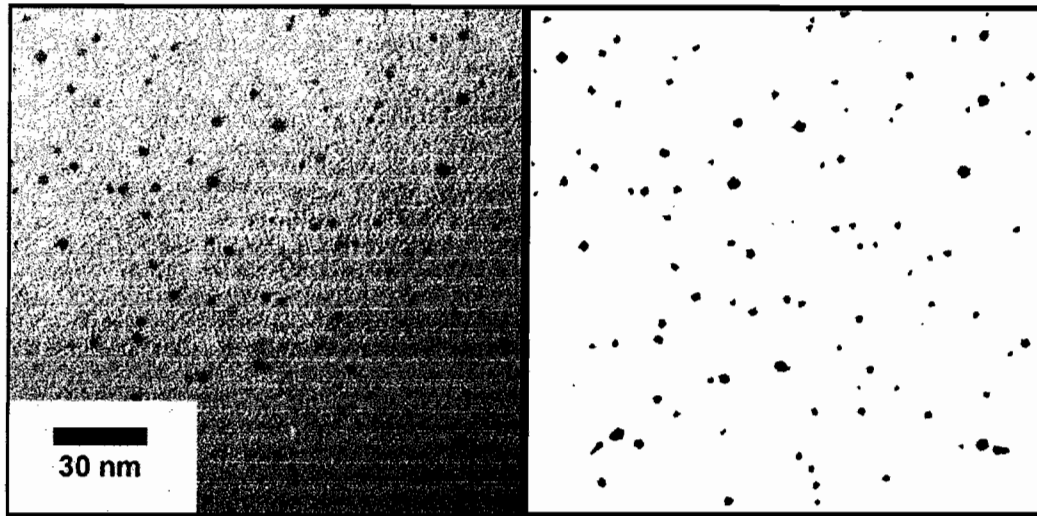
Figure 1.16. TEM images of dispersed gold nanoparticles on a SiO$_2$ TEM grid. The image at left shows the nanoparticles prior to threshold filtering to obtain the binary image at right. The binary image is eroded by one pixel, then dilated, and it closely matches the pre-binary image.

different types of images can be displayed from a given specimen, given suitable detectors, amplifiers, and a display screen for each type of image.

Surface topography of a given specimen is imaged by detection of secondary electrons, which result from inelastic scattering of the incident focused electron beam. As the angle of incidence between the focused electron beam and the surface normal increases, the fraction of secondary electrons produced within the escape depth of the surface also increases. Consequently, as the primary electron beam is scanned over a surface with topography, the local angle of incidence will vary and produce corresponding changes in the secondary electron signal. The end result is the production of light and shadow regions in the displayed image, which can be intuitively interpreted by the operator to understand the surface structure (Fig 1.17).[112] In addition to

measurement of topographic contrast, higher-energy backscattered electrons can be

detected separately and used to map the elemental composition of the specimen.[113]
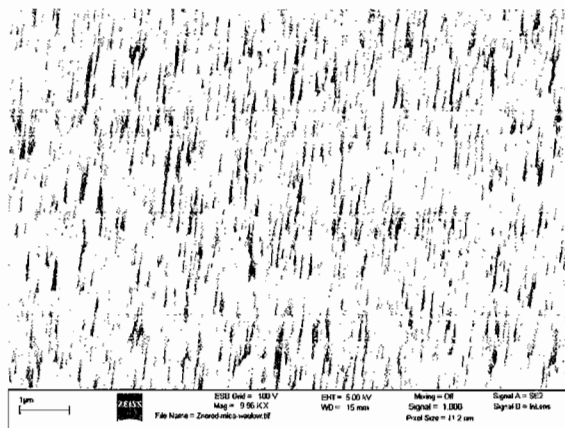
Figure 1.17. SEM image of a ZnO nanowire array. The image shows the surface topography of the vertically aligned nanowires. The scale bar is 1 μm, and the individual nanowires are 40 nm in diameter on average. This image was collected with a Zeiss Ultra Scanning Electron Microscope operated at 5 kV accelerating voltage.

Contact Angle Goniometry. Contact angle goniometry is a fast and simple

method for obtaining information about the surface free energy of a planar substrate.

Generally, a very small volume of water, typically 1 μL, is placed on a solid surface, and

the angle between the substrate surface covered by the drop and the surface of the drop

near the liquid-solid interface is measured. The measured angle is thought to depend on a

complex interplay between the free energies of the solid-liquid, solid-vapor, and liquid-

vapor interfaces. The amount of information obtained from contact angle measurements

can be increased by measuring contact angles as a function of pH of aqueous drops,[93, 114]

the use of liquids other than water as the probe liquid,[115] and the measurement of

advancing and retreating contact angles.[116] For the research described in this dissertation, we employ only a sessile drop of pure water to quickly gain an understanding of the hydrophobicity of the substrate.[117] While contact angle goniometry is generally considered to be a simple, qualitative means of gathering information about the surface free energy of a planar substrate, very small changes in the functionality and composition of the surface can affect its wettability significantly.[115, 118] The contact angles of alkanethiol monolayers on gold, for example, increase with increasing chain length because the increase in total van der Waal's interactions between adjacent chains induce higher degrees of ordering in the monolayer. Thiol monolayers containing hydrophilic surface functional groups (carboxylic or phosphonic acids, for example) give low static contact angles, while those presenting more hydrophobic long alkyl chains or perfluorinated alkyl chains have much higher contact angles. Using this method, we can quickly assess the extent of surface modification processes, as described in Chapter V regarding thiol-thiol ligand exchange reactions on surface-bound nanoparticle monolayers.

Dissertation Overview

Chapter II is a demonstration of orthogonal self-assembly utilizing the two surface chemical interactions most important to the work described in this dissertation: thiolate monolayers on gold and phosphonic acid monolayers on metal oxides. In short, it was discovered that hafnium adsorbed onto a bare gold substrate could be used to assemble high-quality alkanephosphonate monolayers which resist displacement by

thiols. Utilizing this new surface chemistry, patterned substrates were prepared in which a hafnium(IV) species is patterned on gold. Using a bifunctional molecule, 2-mercapto-ethylphosphonic acid (2-MEPA), it was demonstrated that simultaneous formation of two different monolayers could be achieved from the same molecule. The 2-MEPA bound to the hafnium-patterned regions through the phosphonate functionality and to the bare gold regions through the thiol functionality. The unique patterned substrates are characterized by TOF-SIMS imaging. Greg Kearns, Christina Inman, and Evan Foster all contributed to this work.

Chapter III lays the foundation for the nanoparticle monolayer work described throughout the remainder of the dissertation. Small gold nanoparticles with a thiol ligand shell containing phosphonic acid terminal functionality previously had been shown to selectively assemble onto hafnium-modified silicon dioxide substrates. The resulting monolayers appeared dense enough to allow electronic characterization of the planar nanoparticle films, but the initial studies were carried out on native silicon dioxide, which was problematic for electrical measurements. As a result, we opted to use silicon substrates with a thick, thermally-grown silicon dioxide layer to more effectively isolate the nanoparticle layer from the semiconducting bulk substrate. Important differences in the surface compositions of native and thermal silicon dioxides necessitated the development of a surface modification scheme to convert surface siloxane functionality to more reactive surface silanol groups. This was achieved through the use of a physical oxygen plasma etch and wet chemical treatment. Using this surface modification strategy in conjunction with SiO_2 TEM grids, it was shown that surface pre-treatment strongly

impacts surface reactivity with Hf(IV) species in solution and thus has a strong effect on the nanoparticle coverage realized on thermal silicon dioxide. Based on our surface silanol regeneration treatments, we were able to deposit extended surface-bound nanoparticle monolayers dense enough to support electron transport across a micrometer-scale electrode gap. The surface modification strategy, the resulting nanoparticle monolayers, and their electronic properties are described. Evan Foster also contributed to this work.

Chapter IV describes an exciting new application of directed self-assembly of nanoparticle monolayers and how nanoparticle films selectively assembled onto patterned zinc oxide substrates can be used to generate vertical arrays of zinc oxide nanowires. The use of selectively assembled nanoparticles for generating other nanostructures is a marked improvement over previous approaches utilizing spin-cast films of colloidal gold or evaporated gold films as the catalyst. Our technique allows simple, rapid, bottom-up assembly while offering a significant reduction in the amount of gold waste generated. The zinc oxide nanowires synthesized by this approach are well-aligned and of good crystal quality as determined by photoluminescence measurements. I worked closely with Dr. Daisuke Ito, a visiting scholar from Sony Corporation in Japan, on this project.

Chapter V describes a new direction in my research. Rather than focusing on particle-surface interactions in gold nanoparticle monolayers, new strategies were developed in order to manipulate the interaction of nanoparticle monolayers with the environment above the plane of the assembly. Here, a new post-deposition modification approach is described that uses thiol-thiol ligand exchange chemistry to introduce new

surface functionality to phosphonic acid-derivatized gold nanoparticles on hafnium-modified silicon dioxide. Contact angle studies show the change in surface wettability as the hydrophilic phosphonic acid ligand is exchanged for incoming alkanethiols or semi-perfluorinated alkanethiols. In addition, TEM analysis shows the particle monolayers are stable to the exchange process, as the average particle diameter and number of gold cores per unit area are preserved. Composition analysis confirms the extent of surface modification and reveals that the nanoparticles are asymmetrically etched by a large excess of thiol in solution. By this approach, it is shown that a library of incoming thiols can be used to tune the surface properties of the nanoparticle arrays.

Chapter VI is another demonstration that surface modification techniques used for planar gold substrates are applicable to gold nanoparticle monolayers. Using UV-generated ozone, thiolates on the pre-assembled gold nanoparticles are oxidized to physisorbed sulfonates, which are readily rinsed away with water. This treatment yields gold nanoparticle monolayers that are bound to the underlying substrate, but the gold cores are exposed to the surrounding environment. XPS and TEM analysis confirm that the gold nanoparticle layers remain surface-bound after UV/ozone treatment and that the nanoparticles remain in the ideal size range for catalysis even though limited aggregation is observed. This treatment was applied to gold nanoparticle monolayers assembled onto iron oxide powders to show that UV/ozone exposure activates gold nanoparticles to participate in the catalytic conversion of CO to CO_2 at room temperature.

Bridge

During my first year rotation in the Hutchison laboratory, I attempted to produce metal-insulator-nanoparticle-insulator-metal (MINIM) structures based on the incorporation of surface sol gel-derived hafnium oxide as the insulating component. At the same time, Evan Foster was developing a new method for directed self-assembly of gold nanoparticles ligated with thiols containing phosphonic acid terminal functionality and their covalent attachment to hafnium-modified silicon dioxide. Greg Kearns had recently noted the unexpected ability of hafnium species to modify gold surfaces in his attempts to fabricate uniformly hydrophobic interdigitated electrode arrays for biomolecular nanolithography. Due to common research interests, we, along with Christina Inman, investigated alkylphosphonic acid monolayers formed on hafnium-modified gold surfaces. As part of this work, I developed a unique orthogonal self-assembly scheme based on the simultaneous formation of two distinct monolayers from a solution of a single, bifunctional adsorbate. This new surface chemistry on gold is described in Chapter II as a demonstration of the complementary use of thiol SAMs on gold and phosphonic acid SAMs on metal oxides, the two surface chemical interactions that comprise one of the central themes in this dissertation.

CHAPTER II

ALKANEPHOSPHONATE MONOLAYERS ON HAFNIUM-MODIFIED GOLD:

A NEW CLASS OF SELF-ASSEMBLED ORGANIC MONOLAYERS

Introduction

Control over the surface and interfacial properties of materials is essential to their

integration into a wide range of applications, and a variety of surface functionalities are

required to meet the needs of current and future materials modification.[1-6] Self-assembled

monolayers (SAMs) are particularly attractive candidates for materials modification

because they produce well-defined surfaces that can incorporate a wide range of

functionalities without significantly modifying the bulk properties of the underlying

material. While thiol monolayers have been extensively studied for the surface

modification of coinage metals,[1,2,7] it is desirable to discover and develop new surface

chemistries that offer enhanced or orthogonal functions to those of the thiols.

Alkylphosphonate monolayers have been widely investigated for use in the functionalization of metal oxides,[8-10] as well as hafnium-modified silicon dioxide.[11,12] For example, silicon dioxide modified with hafnium(IV) has been used to create patterned, two-dimensional gold nanoparticle arrays.[13] However, the modification of gold substrates with an alkylphosphonate using a hafnium linker has not been previously described. Here we report how hafnium oxychloride or hafnium(IV) chloride can be used to modify gold surfaces and how the resulting film can be employed as a substrate for alkanephosphonate monolayer assembly.

Development of a class of molecular films based upon phosphonate monolayers on gold offers a number of potential benefits that complement the attributes of alkanethiol monolayers on gold. Alkylphosphonate adsorbates assembled on hafnium-modified gold may exhibit enhanced stability. The gold/hafnium/alkylphosphonate chemistry can be used to modify metal and metal oxide surfaces concurrently, such as gold electrodes patterned on a silicon substrate. This makes it ideal for use in the homogeneous functionalization of electrode arrays for numerous electronics applications. The phosphonate chemistry may offer the possibility of patterning gold surfaces with stable domains. Previous work by Imbayashi et al. has shown that when two different thiols are phase separated on a gold substrate, they interdiffuse over time and blur the boundaries between the two functionalities.[14] As long as diffusion does not occur between thiol and alkylphosphonate/hafnium domains, the hafnium/phosphonate chemistry should allow the creation of well-defined boundaries between two different surface functionalities. For example, it could be used as a barrier to prevent diffusion

between adjacent patterned thiol regions on a surface, or to pattern a region on a gold surface before subsequent modification with a thiol adsorbate. Finally, it may be possible to use this assembly chemistry to create monolayers with thiol reactive terminal functionality, such as maleimide groups, which are used for biochip applications.[15,16]

We initially investigated the use of hafnium/alkanephosphonate chemistry to generate a hydrophobic surface between the fingers of interdigitated gold electrode arrays on a silicon dioxide substrate.[11,12] It was thought that this could be accomplished by first selectively modifying the silicon dioxide portion of the substrate with hafnium/n-octadecylphosphonic acid (ODPA), followed by modification of the gold with an alkanethiol. After treating the substrate with only hafnium/ODPA, the entire surface, including the patterned gold region, exhibited uniform hydrophobicity. Subsequent x-ray photoelectron spectroscopic analysis showed the presence of hafnium and phosphorus on the entire surface, including silicon dioxide and gold regions, indicating that the hafnium/ODPA binds to both the glass and gold surfaces. Moreover, the hafnium/ODPA layer was able to block thiol adsorption to the gold upon exposure of the substrate to a solution of allyl mercaptan (see Appendix A).

Following these initial investigations, we explored and characterized these alkanephosphonate monolayer assemblies on hafnium-modified gold. We found that the approach forms alkanephosphonate monolayers that are sufficiently well-ordered and dense to resist displacement by thiols in subsequent treatment steps. The approach allows easy preparation of patterned substrates. In addition, the hafnium-gold chemistry is compatible with and orthogonal to gold-thiol assembly strategies. We demonstrate this

capability by using hafnium-patterned gold surfaces in tandem with the bifunctional molecule 2-mercaptoethylphosphonic acid (2-MEPA) to create a unique patterned surface.

Experimental

Materials. Hafnium dichloride oxide octahydrate (Alfa Aesar; 99.998%), hafnium (IV) chloride (STREM; 99.9+%), n-octadecylphosphonic acid [$CH_3(CH_2)_{17}P(O)(OH)_2$] (Alfa Aesar), allyl mercaptan (Avocado Research Chemicals, Ltd.; 70%), zirconium dichloride oxide octahydrate (Alfa Aesar; 99.9%), Shipley 1818 Photoresist (Shipley Company, Marlborough, MA), and Microposit 351 Developer (Shipley Company) were used as received. 2-Mercaptoethylphosphonic acid [$HS(CH_2)_2P(O)(OH)_2$] was synthesized as previously reported.[13] Methyl alcohol (J.T. Baker; 100.0%) was distilled over magnesium. Deionized water (18.2 MΩ-cm) was purified with a Barnstead Nanopure Diamond system. Absolute ethyl alcohol (Aaper Alcohol and Chemical Company) was sparged with nitrogen for approximately 20 minutes prior to use.

Preparation of Substrates. The Si substrates used in this study were cut from n-type <100> wafers with 10-20 Ω-cm resistivity (University Wafer, Boston, MA). The Si and glass substrates used in this research were cleaned in a piranha solution (7:3 conc. H_2SO_4: 30% H_2O_2) for 15 minutes, rinsed with copious amounts of deionized water, and dried under a stream of argon prior to any assembly chemistry. Gold substrates on both glass and Si were prepared by evaporating 10 nm of chromium to promote adhesion of

the gold layer, followed by 100 nm of gold. The gold-coated substrates were exposed to ozone for 10 minutes in a UV/ozone cleaner supplied with laboratory air at room temperature prior to further modification. Unpatterned monolayers of ODPA on Hf-modified gold were prepared by soaking gold-coated glass slides in either a 5 mM aqueous solution of $HfOCl_2$ for 3 days at 50°C or a 5 mM solution of $HfCl_4$ in methanol for 30 minutes at room temperature. Upon removal from the soaking solution, the substrates were rinsed with deionized water or methanol, dried under a stream of argon, and soaked in a 1 mM ethanolic solution of ODPA for 24 hours.

Photolithographic patterning of the Si substrates was achieved using Shipley 1818 Photoresist. The resist was applied using a dropper and spin-coated onto each gold-coated wafer at a speed of 3,000 rpm for 60 seconds. Solvent was driven off by heating the wafer on an aluminum block at 110 °C for 60 seconds. The substrate was then placed under a pre-fabricated emulsion mask using an OAI Model 200 Contact Mask Aligner and exposed to UV light for 11 seconds (125 W/cm^2). The photoresist patterns were developed by agitating in a mixture of 3.5:1 deionized water: Microposit 351 Developer for 60 seconds. The substrates were rinsed again in deionized water and dried under a stream of nitrogen. The patterned substrates were heated at 120 °C for 1 hour to improve the adhesion of the photoresist to the substrate. Any photoresist residue remaining within the exposed gold regions was removed by an oxygen plasma treatment (300 W, 5 seconds, 400 mT).

Following the oxygen plasma treatment, the substrates were rinsed with deionized water and immediately transferred to a 5 mM aqueous solution of $HfOCl_2$ at 50 °C for

three days. The substrates were then sonicated in water for five minutes to remove any physisorbed material, rinsed with water, and dried with a stream of argon. Photoresist was removed by sonicating the substrates in acetone, followed by a short oxygen plasma treatment as described above. The patterned substrates were then soaked for one hour in a 1 mM ethanolic solution of 2-MEPA. The substrates were finally soaked in a 5 mM aqueous solution of $ZrOCl_2$, sonicated for five minutes in water to remove physisorbed material, and rinsed with water before drying the finished substrates with a stream of argon.

Analysis Techniques. Polarization modulation infrared reflection absorption spectroscopy (PM-IRRAS) studies were performed on a Nicolet Magna-IR 550 spectrometer with dual channel input and equipped with a photoelastic modulation (PEM) accessory (ThermoNicolet, Madison, WI) using 1024 signal-averaged scans with a mirror velocity of 0.9494 cm/sec and a resolution of 2 cm^{-1}. The PEM module consists of beam steering and focusing optics, a wire grid polarizer, a PEM head and controller assembly (Hinds Instruments, Hillsboro, OR), an MCT-A liquid nitrogen cooled detector (ThermoNicolet, Madison, WI), and an SSD Demodulator (GWC Instruments, Madison, WI). For PM-IRRAS, no background spectrum collection is necessary.[17] Baseline normalization[†] was performed using Igor Pro software (Wavemetrics, Lake Oswego, OR).

[†] Baseline normalization was performed using a procedure written for Igor Pro by Robert Corn's group. For more information, see http://corninfo.ps.uci.edu.

X-ray photoelectron spectroscopy measurements were conducted using a Kratos AXIS HSi spectrometer (Kratos Analytical, Chestnut Ridge, NY) with a monochromated Al Kα x-ray source. Contact angle measurements were conducted using a microscope equipped with a goniometer, utilizing the sessile drop method.[18] TOF-SIMS imaging experiments were carried out using an ION-TOF Model IV spectrometer (ION-TOF, Münster, Germany) with a bismuth liquid metal ion gun as the primary ion beam.

Results & Discussion

Building on the intriguing results from our initial XPS studies (see Appendix A), we performed a series of experiments to explore the surfaces resulting from the hafnium/ODPA treatments and to understand why these treatments prevent thiols from binding to the gold surface. By characterizing gold surfaces modified with hafnium followed by ODPA using contact angle goniometry, polarization modulation infrared reflection absorption spectroscopy (PM-IRRAS), and XPS we found that the hafnium linker chemistry allows for self assembly of high quality alkanephosphonate monolayers on gold. We also used gold substrates patterned with hafnium to generate unique surfaces in tandem with gold-thiol assembly methods.

In our assembly strategy, gold substrates are first ozone treated and then soaked in a 5 mM solution of HfCl$_4$ in methanol at room temperature for 30 minutes. After removal from the hafnium solution, the substrates are rinsed with nanopure water for 15 minutes and then soaked in a 1 mM ethanolic solution of ODPA. Control experiments were also performed where the gold substrate was immediately placed in the ODPA

soaking solution after ozone treatment. After soaking in ODPA solutions for 24 hours, the resulting substrates were characterized by contact angle goniometry, PM-IRRAS, and XPS.

ODPA monolayers formed directly on gold yielded a static contact angle of $82 \pm 3°$, whereas the contact angle measured for ODPA monolayers formed on gold with the hafnium linker was $105 \pm 2°$. This suggests the formation of reasonably dense, well-ordered monolayers of ODPA on the hafnium-modified gold. This measurement is in good agreement with contact angles measured for ODPA monolayers on other substrates, including TiO_2 and Ta_2O_5.[19-21]

PM-IRRAS data show two major peaks (Figure 2.1) for ODPA assemblies deposited directly on gold as well as for monolayers formed on gold with a hafnium linker. ODPA monolayers formed on hafnium-modified gold exhibit significantly larger peaks than ODPA monolayers formed on bare gold. This indicates that a monolayer of higher coverage is formed on the hafnium-modified gold, though PM-IRRAS cannot be used to determine the coverages quantitatively. The two peaks at 2922 cm^{-1} and 2851 cm^{-1} correspond to the CH_2 (asym) and CH_2 (sym) peaks, respectively.[22] The shoulder of the CH_2 (asym) peak at 2959 cm^{-1} corresponds to the CH_3 (asym) peak.[22] These peak positions are in good agreement with the IR spectra observed for ODPA monolayers on other substrates.[23] Although the CH_2(asym) peak position is at slightly lower frequency than that normally observed for very dense, well-ordered films, this value for ODPA monolayers on hafnium-modified gold is within range for reasonably well-ordered alkylphosphonate monolayers on metal oxide surfaces.
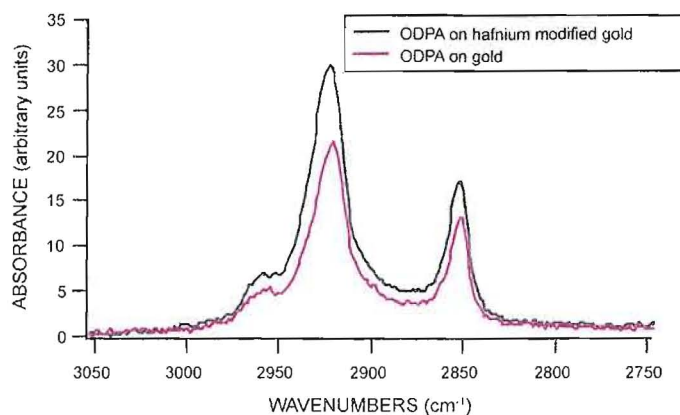
Figure 2.1. PM-IRRAS spectra for octadecylphosphonic acid monolayers formed directly on gold (red line) and on gold modified with a hafnium linker (black line). The spectra are baseline normalized, and although the relative intensities within each spectrum are correct, the absolute spectral intensities cannot be compared between the two spectra.

In order to further clarify the PM-IRRAS data, we attempted to determine the difference in the amounts of ODPA on bare gold and hafnium-modified gold surfaces more quantitatively by utilizing XPS. The XPS data for ODPA monolayers formed on gold with and without the hafnium linker are shown in Figure 2.2. Table 2.1 summarizes the atomic concentration quantification. No phosphorus is observed for ODPA assemblies formed on gold without a hafnium linker present, indicating that the amount of ODPA present on these substrates is below the detection limit of the instrument or that the adsorbate readily desorbs under vacuum. The XPS data for ODPA assemblies formed on hafnium-modified gold show the presence of hafnium, phosphorus, oxygen and a significant amount of carbon. The gold peak is also significantly attenuated. These data indicate that an ODPA monolayer has formed on the hafnium-modified gold. The Hf

$4f_{7/2}$ peak appears between 17 and 18 eV, indicative of the Hf^{4+} chemical state, and no chlorine is observed by XPS, indicating that the surface species formed by hafnium on gold is likely a hafnium oxide.
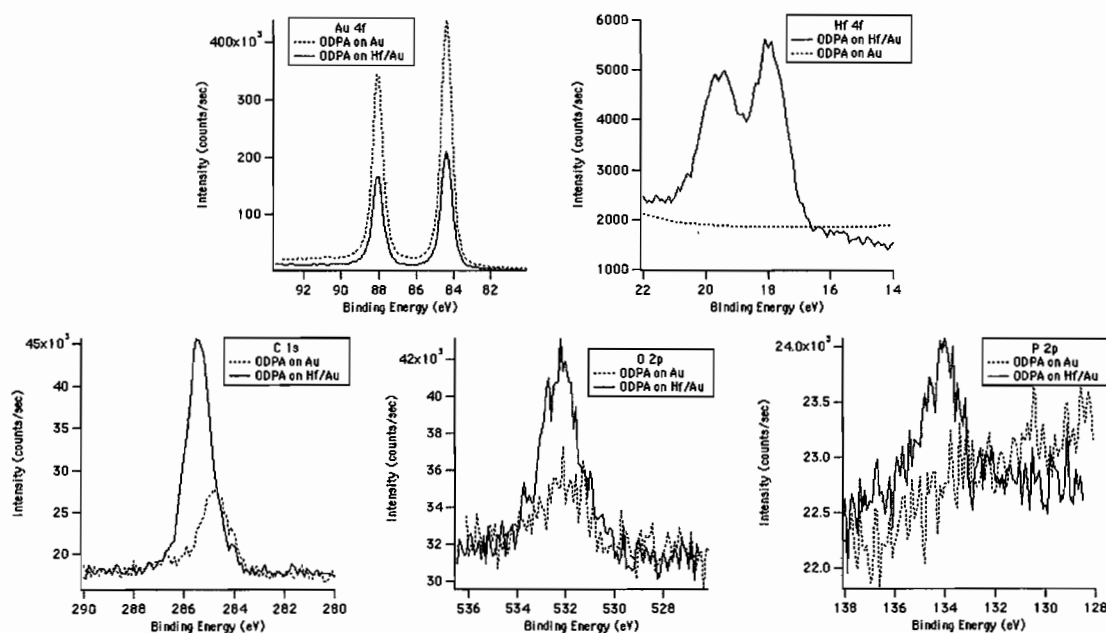
Figure 2.2. XPS spectra for octadecylphosphonic acid (ODPA) monolayers formed directly on gold (dashed line) and on gold modified with a hafnium linker (solid line). The data indicate that the monolayer coverage on the Hf/Au surface is significantly higher.

The contact angle, PM-IRRAS, and XPS data all indicate the presence of a stable ODPA monolayer on hafnium-modified gold. In contrast, XPS and TOF-SIMS data for ODPA deposited on bare gold show nearly undetectable amounts of ODPA on the surface. PM-IRRAS data for ODPA on bare gold indicate the presence of a monolayer structure. Furthermore, contact angle measurements show that the gold substrates

exposed only to an ethanolic solution of ODPA are more hydrophobic than bare gold substrates, indicating the presence of some organic material on the surface. It is possible that either weak binding to the gold allows for ready desorption of ODPA from bare gold under high vacuum in the XPS experiments but not under the ambient conditions of the PM-IRRAS and contact angle studies, or that the small amount of ODPA present in those samples, coupled with the relatively low atomic sensitivity of phosphorus in XPS, makes it difficult to detect. In either case, taken together, these data suggest that there may be small patches of organized ODPA on the bare gold surface, but the majority of the surface is likely unmodified.

Table 2.1. Quantification of XPS data for ODPA monolayers formed on gold with and without a hafnium linker. Values given are relative atomic concentration. In the absence of phosphorous signals for ODPA on gold, we conclude that carbon and oxygen signals recorded for this sample are adventitious.

Monolayer	Au (4f)	P (2p)	C (1s)	O (1s)	Hf (4f)
ODPA on gold	59	0	33	5	--
ODPA on Hf-modified gold	22	6	58	10	2

We were initially surprised that hafnium treatment would facilitate alkanephosphonate binding to gold because the binding of a "hard" cation (Hf(IV)) to a "soft" surface like gold seems unlikely: gold generally prefers soft donor atoms such as sulfur. Although we have not yet been able to fully characterize the bonding between the gold surface and the hafnium linker, given the affinity of hafnium (IV) for oxide surfaces, the higher-than-expected concentration of oxygen by XPS, and the absence of a chlorine signal by XPS, a reasonable hypothesis is that Hf(IV) binds to a gold oxide[24] layer, rather

than directly binding to the "soft" gold surface. The presence of Au-O-Hf fragments in TOF-SIMS spectral studies of these surfaces also supports this hypothesis (Appendix A).

In previous work,[25] it has been shown that two SAMs can be formed independently by simultaneous adsorption of two different adsorbate molecules from a common solution on a substrate consisting of both gold and metal oxide at its surface. Similarly, the attributes of this new surface chemistry make possible a number of sophisticated orthogonal self-assembly schemes, taking advantage of the specificity of phosphonates for Hf/Au and thiols for Au and the relative stability of each interaction. The chemistry shown in Scheme 2.1 highlights the use of the hafnium/gold chemistry to design unique patterned surfaces. The last segment of Scheme 2.1 shows an illustration of the target structure, where the bifunctional molecule 2-mercaptoethylphosphonic acid (2-MEPA) is assembled on a gold substrate that has been patterned with hafnium. We chose a molecule with both thiol and phosphonic acid functionalities to take advantage of the different binding properties of thiols versus phosphonates. We hypothesized that 2-MEPA would bind through the phosphonate functionality on the hafnium-patterned regions of the surface and through the thiol functionality on the bare gold, thus simultaneously forming two different SAMs from a solution containing a single adsorbate molecule. Zirconium is subsequently deposited on the exposed phosphonate groups on the unpatterned portion of the surface for visualization using TOF-SIMS.

In order to test this idea, a clean gold film was patterned by photolithography to expose areas of the surface. The patterned film was briefly treated with oxygen plasma to remove any remaining resist from the exposed areas, and the substrate was subsequently

soaked in an aqueous solution of HfOCl$_2$.[13, †] The photoresist was then stripped with

acetone, and the substrate was soaked in a solution of 2-MEPA. After rinsing with

copious amounts of ethanol the substrate was soaked in an aqueous solution of ZrOCl$_2$ to

mark the regions where the phosphonic acid functionality of 2-MEPA was exposed.

Scheme 2.1. Processing Steps for Fabrication of Hf/Zr Patterned Substrates
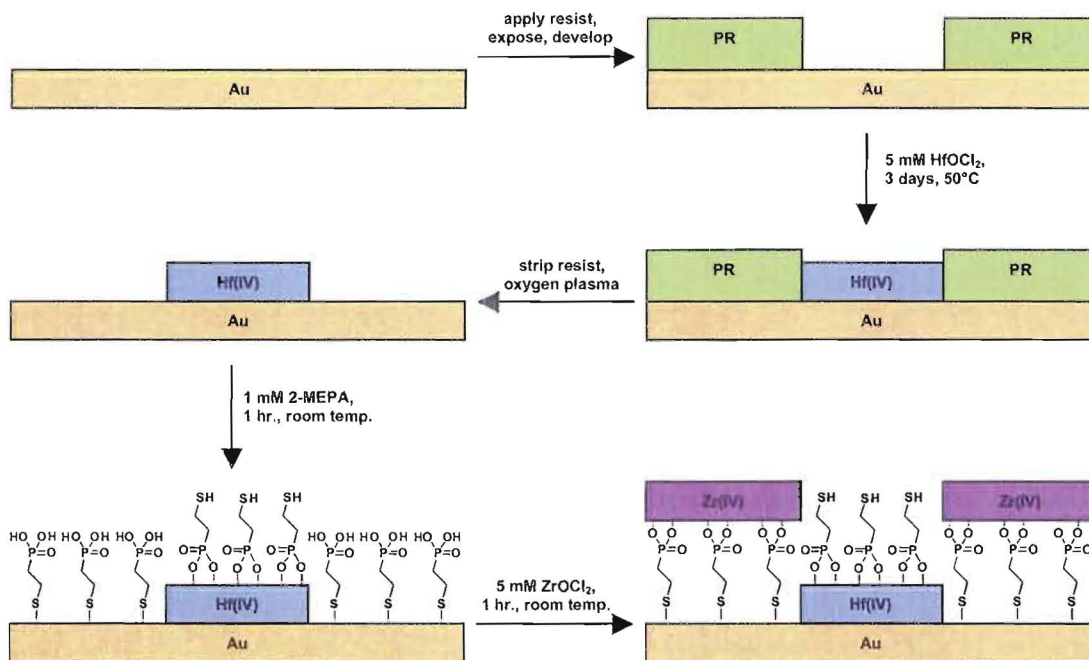
The final structures were imaged by time-of-flight secondary ion mass

spectrometry (TOF-SIMS). The images in Figure 2.3 show ion yields of the HfO, ZrO, S

and PO$_3$ fragments. The patterning of hafnium and zirconium is clearly visible, and the

---

† Hafnium oxychloride was used, rather than hafnium chloride, for hafnium deposition, because methanol would remove the photoresist. No differences in the data obtained for alkylphosphonate monolayers formed on gold surfaces using either of the hafnium solutions were observed by XPS, contact angle, or PM-IRRAS.

ion yields of PO$_3$ and sulfur reflect the difference in orientation of 2-MEPA between the

hafnium-functionalized areas and the bare gold.
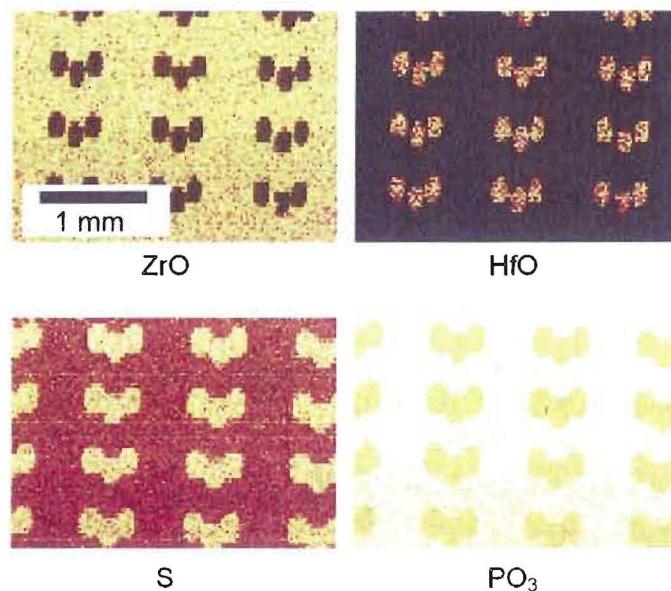
Figure 2.3. TOF-SIMS imaging data from patterned sample. The bright areas correspond to higher ion yields. In the images for S and PO$_3$, the presence of both fragments is detected over the entire surface; however, the differences in intensity between the patterned regions and the surrounding surface reflect the difference in the orientation of 2-MEPA on those areas of the substrate.

Conclusions

In summary, we have described a strategy that can be used to easily assemble

stable alkanephosphonate monolayers on gold using a hafnium linker molecule, opening

up the possibility of functionalizing gold surfaces with a new class of organic

monolayers. We have also described how this chemistry can be used to create patterned

gold surfaces. In the process, we have shown that the gold-hafnium assembly strategy is

compatible with gold-thiol chemistry and that the two strategies can be used in a

complementary manner to create uniquely patterned and functionalized surfaces. We are currently exploring the nature of the surface interactions, how this assembly approach can be employed to attach other metal oxide-binding adsorbates to gold surfaces, and whether these monolayers can be used as etch resists.

Bridge

Having demonstrated the principle of orthogonal self-assembly using bifunctional thiol-phosphonates, we developed a method of forming gold nanoparticle monolayers that simultaneously utilizes both of the self-assembled monolayer chemistries described in Chapter II. Evan Foster had previously developed a system of nanoparticle monolayer formation in which small gold nanoparticles (d_{core} = 1.5 ± 0.5 nm) protected with a thiol ligand shell containing terminal phosphonic acid functionality are assembled onto hafnium-modified silicon dioxide substrates. Although this previous work was carried out on native silicon dioxide, we wanted to form the nanoparticle films on thermally grown silicon dioxide for electrical characterization. Thermal silicon dioxide is a much less reactive surface than the native oxide. Chapter III describes our method for activating thermal silicon dioxide surfaces for the formation of extended, high-density gold nanoparticle monolayers. We demonstrate the effectiveness of this approach by TEM imaging of nanoparticle monolayers formed on silicon dioxide TEM grids and by demonstrating electron transport supported by these monolayers across micron-scale in-plane electrode gaps.

CHAPTER III

SURFACE MODIFICATION STRATEGY FOR THE FORMATION OF EXTENDED,

HIGH-DENSITY GOLD NANOPARTICLE MONOLAYERS ON THERMALLY

GROWN SILICON DIOXIDE

Note: Portions of Chapter III are expected to appear in an upcoming publication, co-authored by Jespersen, M. L., Foster, E. W., and Hutchison, J. E. The first author designed experiments and carried out all of the experimental work described in this chapter. The author also composed the manuscript corresponding to Chapter III. E. W. Foster carried out the initial development of the sample preparation method described herein as well as some preliminary analysis. Both E. W. Foster and J. E. Hutchison provided experimental and editorial guidance. All materials syntheses and most of the analyses were carried out at the University of Oregon, with some analysis performed at the Surface Characterization and Nanofabrication Lab at the University of Utah.

Introduction

Metal nanoparticles are a particularly interesting class of materials due to their unique size-dependent electronic,[1-4] optical,[5-7] and catalytic properties.[8-14] The size-dependent electronic properties of metal nanoparticles in the 1-2 nm size range have inspired many studies of single electron transistors produced by bottom-up assembly methods, in which the active device region consists of an individual particle or a very small number of particles.[15,16] Though such test structures serve as useful proofs of concept, they have shown limited promise for practical development of nanoelectronic

devices because it is difficult to produce large numbers of functional devices of this sort in parallel. Random assembly methods used to isolate small numbers of nanoparticles between electrodes result in low device yields and are not yet feasible for high-throughput device fabrication. Additionally, the presence of trapped charges in the substrate under the active device area have been predicted to disrupt the functionality of these devices.[17,18] In order to take advantage of the unique electronic properties of metal nanoparticles, reliable methods are required for their assembly on surfaces and for precise control over their positioning.

Two-dimensional arrays of metal nanoparticles offer a number of advantages over single-particle test structures. Because two-dimensional assemblies of nanoparticles present multiple parallel charge transport pathways, the presence of a small number of trapped charges in the underlying substrate should not significantly affect device characteristics.[17,18] Monolayers of nanoparticles are also patternable within current lithographic capabilities. Therefore, surface chemical interactions can be utilized to reliably guide the assembly of nanoparticles onto chemically patterned regions on a substrate and enable simultaneous bottom-up assembly of very large numbers of devices.

Several groups have reported methods for the assembly of two-dimensional metal nanoparticle arrays on planar substrates. Langmuir-Blodgett (LB) methods, for example, have been shown to form dense monolayers of 1-2 nm gold nanoparticles with short-range ordering.[19] A variation on this method for nanoparticle assembly is the transfer of pre-assembled LB films of particles from a water subphase to a target substrate by microcontact printing.[14,20] This approach separates self-assembly and integration onto the

target substrate through the use of a transfer step, thus eliminating contamination or processing issues arising from incompatibility of the target substrate with the conditions required for self-assembly from solution. These studies incorporated 5-nm gold nanoparticles, while formation of well-ordered LB films of 1-2 nm gold nanoparticles that extend over the macroscale has proven to be challenging.[19] More recently, others have investigated the direct formation of highly-ordered nanoparticle monolayers by a kinetically-driven self-assembly process.[21,22] This approach generates close-packed, two-dimensional arrays of nanoparticles that have proven to be excellent model systems for the study of electron transport in nanoparticle monolayers with in-plane electrodes.[22] Despite the advantages of the assembly strategies mentioned here, they are somewhat more complicated than directed self-assembly processes because they require excess free ligand, application of external forces, or far-from-equilibrium conditions (e.g., rapid solvent evaporation). For these reasons, it may be difficult to implement these assembly strategies for large-scale device fabrication.

For device applications, it is desirable to integrate nanoparticle arrays by self-assembly directly onto the target substrate in one step with a high degree of selectivity. Directed self-assembly processes are also compatible with current lithographic schemes, so it should be possible to integrate bottom-up assembly schemes for nanoscale materials into established semiconductor device processing methods. Self-assembly of functionalized nanoparticles onto lithographically-patterned susbstrates has been shown to generate extended, high-density gold nanoparticle monolayers.[23] Our approach utilizes gold nanoparticles stabilized with a thiol ligand shell containing terminal phosphonic acid

functionality, which assemble readily onto hafnium-modified SiO_2 to yield dense monolayers of chemically anchored gold nanoparticles. Based on our initial TEM analysis of these films, we hypothesized that the nanoparticle monolayers thus obtained were dense enough to support charge transport across an electrode gap, using in-plane electrodes patterned by shadow evaporation. Since the native oxide layer on silicon is very thin (27-30 Å), it was difficult to measure the current-voltage properties of the system without penetrating through the oxide layer, resulting in measurement of electron transport through the bulk substrate rather than through the nanoparticle film.

In order to enable the electrical characterization of the system, we opted to use silicon substrates with a thicker, thermally grown oxide layer (approximately 3 μm) to effectively isolate the nanoparticle monolayers from the underlying silicon. Nanoparticle monolayers formed on thermal silicon dioxide, however, were not as dense as those observed on the native oxide by TEM. The native oxide surface of silicon is hydrated and has a high concentration of silanol, so it reacts readily with $HfOCl_2$ to yield hafnium(IV)-modified SiO_2.[24] The resulting high level of hafnium coverage on native oxide guides the assembly of dense monolayers of phosphonic acid-functionalized nanoparticles, as observed in our previous studies.[23] Thermal silicon dioxide is grown at temperatures above 800 °C, at which the surface of silicon dioxide dehydrates, resulting in the conversion of silanol groups to relatively unreactive siloxanes.[25] In our studies, thermal silicon dioxide surfaces were less reactive toward $HfOCl_2$, resulting in lower coverage of nanoparticles than that observed on the native oxide. In order to observe electron transport in dense, surface-bound nanoparticle monolayers, it was first necessary to

improve the reactivity of thermal silicon dioxide toward HfOCl$_2$ by regenerating surface silanol.

Here we report the formation of extended, high-density gold nanoparticle monolayers on thermal silicon dioxide. Our surface modification strategy is based on regeneration of surface silanol functionality on thermal SiO$_2$ using a combination of oxygen plasma and wet chemical treatments. This method restores the reactivity of the oxide surface toward HfOCl$_2$ to the level previously observed on native oxide. We demonstrate the effectiveness of this approach by assembling dense films of functionalized gold nanoparticles on the hafnium-modified surface of thermal silicon dioxide. The nanoparticle monolayers are dense enough to support electron transport across a micrometer-scale electrode gap and show symmetric non-linear current-voltage curves characteristic of two-dimensional nanoparticle arrays.

Experimental

Materials. Hafnium dichloride oxide octahydrate (Alfa Aesar; 99.998%) was used as received. 2-Mercaptoethylphosphonic acid [HS(CH$_2$)$_2$P(O)(OH)$_2$] was synthesized as previously reported.[22] Deionized water (18.2 MΩ-cm) was purified with a Barnstead Nanopure Diamond system. Methanol was distilled from magnesium. Dichloromethane was distilled from calcium hydride.

Nanoparticle Synthesis and Functionalization. Functionalized gold nanoparticles (d$_{core}$ = 1.5 $\pm$ 0.4 nm) were synthesized first as triphenylphosphine-stabilized precursors according to a previously described synthesis.[26] Ligand exchange

was carried out under biphasic conditions, starting with 203 mg (~7.9 µmol) of the as-prepared gold nanoparticles in 80 mL dichloromethane and 117 mg (0.82 mmol, 114 molar equivalents) 2-mercaptoethylphosphonic acid in 100 mL H_2O, buffered to pH ≈ 7.4 with a KH_2PO_4/K_2HPO_4 buffer. The biphasic solution was stirred for 48 hours until the organic fraction was clear and no insoluble material was observed as a foamy interphase, indicating completion of the exchange reaction. The aqueous and organic fractions were separated, and the aqueous fraction was washed with dichloromethane (3 x 50 mL). Residual dichloromethane was removed by rotary evaporation. In order to remove excess free ligand, the nanoparticle solution was concentrated to 20 mL, and the water-soluble nanoparticles were purified by a diafiltration process using a Minimate 10 kD diafiltration membrane (Pall Life Sciences) and 50 volume equivalents (1 L) of deionized water.[27] The final purified product was concentrated to 20 mL and lyophilized overnight. ^1H NMR confirms the completion of the exchange reaction and the removal of free ligand from the prepared nanoparticles (see Appendix B).

Preparation of Substrates. The Si substrates used in this study were cut from n-type <100> wafers with 10-20 Ω-cm resistivity and a 3-µm thermal oxide (Wafer World). Silicon dioxide TEM grids were prepared as previously reported.[28] The SiO_2 surfaces were cleaned in a solution of dilute SC-1 (100:4:1 H_2O: 30% H_2O_2: 30% NH_4OH) at 70 °C for 15 min. Substrates were then rinsed with copious amounts of deionized water and dried under a stream of argon prior to further surface treatment. The oxide surfaces were activated using an oxygen plasma treatment (150W, 200 mT, 20 sec), followed by immediate immersion in deionized water. Plasma treatments were carried out using a

March Plasma Systems CS-1710 Plasma Etcher. Following this plasma treatment, the substrates were again treated in dilute SC-1 to remove adventitious carbon contamination and inorganic particulates, as well as to chemically generate surface silanol functionality. The substrates were rinsed with deionized water and transferred directly to a 5 mM aqueous solution of $HfOCl_2$ for four hours at 45 °C. $HfOCl_2$ solutions were filtered through a cellulose acetate syringe filter with 0.2 μm pore size prior to any assembly chemistry in order to remove insoluble particulates. Following the surface functionalization step, the substrates were rinsed with water and transferred to a solution of 2.5 mg nanoparticles per milliliter of 3:1 MeOH: H_2O for 24 hr at room temperature. Following nanoparticle assembly, the substrates were removed from solution, rinsed with copious amounts of deionized water, and dried under a stream of argon. Macroscopic gold electrodes (500 Å thick) were deposited (at 8×10^{-7} mT at 10 Å/s) on the nanoparticle array utilizing a 5-μm tungsten wire (California Fine Wire Co., Grover Beach, CA) as a shadow mask.

Analysis Techniques. X-ray photoelectron spectroscopy measurements were conducted using a Kratos AXIS Ultra Electron Spectrometer (Kratos Analytical, Chestnut Ridge, NY) with a monochromated Al Kα X-ray source, operated at 15.0 kV accelerating voltage and 15 mA emission current. TEM images were obtained using a Phillips CM-12 microscope operating at 120 kV accelerating voltage. Nanoparticle average core diameter and size distributions were obtained using ImageJ.[†] Nanoparticle monolayer

---

[†] TEM image analysis was performed using ImageJ ver. 1.36b, available free of charge from http://rsb.info.nih.gov/ij/.

densities were calculated by counting the number of nanoparticles within a region of known area in a series of TEM images for each sample type. Current-voltage measurements were carried out under vacuum using a Keithley 2361 Source Measure Unit to supply a dc voltage while measuring the resulting current. Voltages were applied in 0.1 V steps, with a 5 sec hold time between steps to allow the system to dissipate any capacitive charging.

Results & Discussion

In order to maximize the density of nanoparticles assembled on thermal silicon dioxide substrates, we first needed to maximize the surface silanol concentration of the oxide surface. Scheme 3.1 illustrates our surface modification strategy. The silicon dioxide surface is first treated in a dilute SC-1 (dSC-1) cleaning solution of 100:4:1 H_2O: 30% H_2O_2: 30% NH_4OH for 15 minutes at 70 °C to remove adventitious carbon contamination and inorganic particulates. The surface is then treated with oxygen plasma (200 mT, 150 W, 20 sec) to generate reactive surface silanol functionality. Following the plasma treatment, the substrate is immediately immersed in deionized water and treated again in dSC-1 solution for 15 minutes at 70 °C to remove organic and inorganic contaminants, as well as to chemically generate surface silanol groups. The substrates are thoroughly rinsed with water and immersed in a 5 mM aqueous solution of $HfOCl_2$ for four hours at 45 °C to deposit a monolayer of a hafnium(IV) linker.[28] Following deposition of the Hf(IV) linker layer, the substrates are immersed in a solution of 2.5 mg

gold nanoparticles per milliliter of 3:1 methanol: water to assemble a monolayer of gold

nanoparticles chemically bound to the underlying hafnium-modified silicon dioxide.
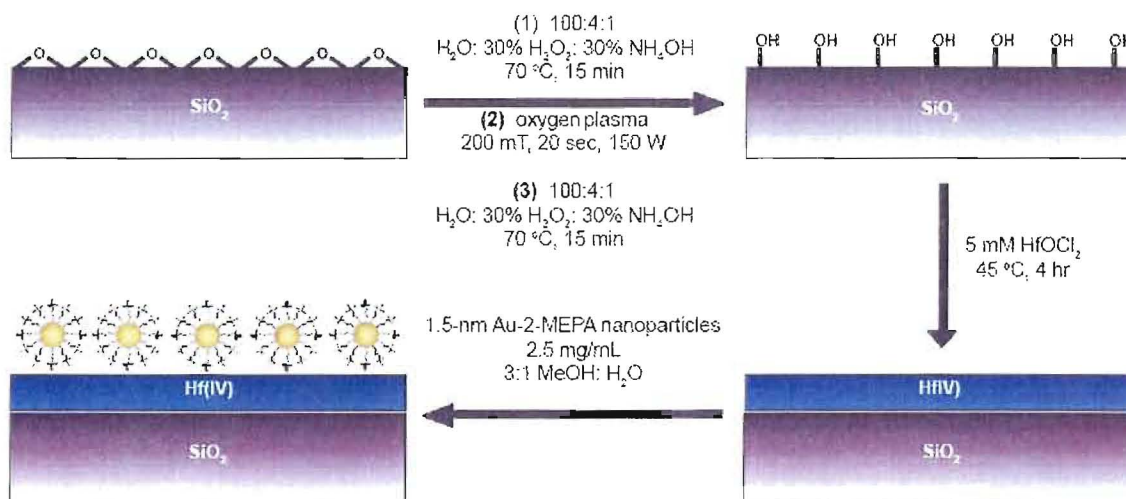
Scheme 3.1. Schematic of the surface modification strategy for generation of dense, surface-bound nanoparticle monolayers on thermally grown silicon dioxide. The wafer is first treated by a physical oxygen plasma etch, followed by a wet chemical treatment to convert surface siloxane groups to silanol. A monolayer of Hf(IV) linker is deposited from an aqueous solution of $HfOCl_2$. Phosphonic acid-functionalized gold nanoparticles bind to the hafnium linker to yield nanoparticle monolayers chemically anchored to the substrate.

In order to obtain the highest possible coverage of nanoparticles, we first wanted

to assess the effectiveness of our silanol regeneration strategy. We did not measure

surface silanol concentration directly but instead used XPS analysis. Because $HfOCl_2$

reacts with surface silanol groups, the efficacy of surface silanol regeneration treatments

was determined utilizing elemental atomic concentrations to calculate Hf: [Si+O] ratios.

In previous work involving only thermal SiO_2, we used Hf: Si ratios to assess hafnium

coverage (Appendix B). In this work, we wanted to compare native oxide and thermal

oxide surfaces. Because the native oxide (27-30 Å) is thinner than the sampling depth of the XPS experiment, photoelectrons emitted from the bulk Si contribute to the overall elemental composition. The thermal oxide (3 μm) is much thicker than the sampling depth and is composed mostly of oxygen atoms, so the contribution of Si to the overall composition of thermal oxide will be much lower than in native oxide. (In our analyses, Si accounted for approximately 40% and 60 % of the overall compositions for bare thermal oxide and native oxide substrates, respectively.) Consequently, the calculated Hf: Si ratio would be greater for thermal oxide than for a native oxide surface with equal hafnium coverage. For these reasons, we use the sum of silicon and oxygen concentrations in our determination of hafnium coverage.

Table 3.1 summarizes the atomic concentration of hafnium resulting from a series of different silanol regeneration treatments. The difference in surface silanol content between native silicon dioxide and thermal silicon dioxide, given identical surface pre-treatments, is evident in the resulting Hf surface coverages. For both untreated and dSC-1-treated substrates, native oxide surfaces showed higher hafnium content than thermal silicon dioxide. Plasma-treated thermal SiO_2 substrates, however, showed enhanced surface reactivity toward $HfOCl_2$ compared to the dSC-1-treated thermal oxide. Oxygen plasma treatment parameters, including pressure, RF power, and treatment time, were optimized, and it was determined that low oxygen plasma pressures (150-200 mT) and short treatment times (20-30 sec) lead to the highest eventual hafnium coverage (see Appendix B). Wet chemical treatment does not have as profound an impact on the reactivity of thermal SiO_2. In fact, additional wet chemical treatment following oxygen

plasma treatment did not increase the reactivity of plasma-treated thermal SiO_2 toward

$HfOCl_2$. This suggests that the physical plasma etch regenerates surface silanol more

effectively than the wet chemical treatments used in this study. Overall, the combination

of wet chemical and plasma treatments appears to improve thermal oxide surface silanol

content to the level observed on native oxide treated with dSC-1, evidenced by the nearly

equal hafnium coverages observed by XPS. We suspect that the physical plasma etch

treatment removes the topmost layers of thermal oxide, exposing reactive surface species

that form surface silanol upon exposure to water.

Table 3.1. Nanoparticle monolayer density, Hf: [Si +O] ratios, and Au: [Si+O] ratios on native and thermal silicon dioxide for a series surface pre-treatments.

Substrate	Treatment	Hf: [Si+O] Ratio[a]	Au: [Si+O] Ratio[a]	Particle Density (%ML)[b]
Thermal Oxide	Untreated	1:370	1:101	27 ($\pm$ 5)
Native Oxide	Untreated	1:200	1:59	-
Thermal Oxide	dSC-1 only	1:290	1:62	45 ($\pm$ 5)
Native Oxide	dSC-1 only	1:120	1:39	77 ($\pm$ 5)
Thermal Oxide	Plasma only	1:100	1:46	68 ($\pm$ 5)
Thermal Oxide	Plasma + dSC-1	1:100	1:41	68 ($\pm$ 5)

[a] Atomic concentrations were determined by XPS analysis using the areas under the Hf 4d, Si 2p, O 1s, and Au 4f peaks. Carbon also contributed to the overall surface composition; however, only Hf, Si, O, and Au were considered for determining atomic concentration ratios.

[b] Particle densities were calculated by counting the total number of nanoparticles present in a region of known area for a series of TEM images for each sample type using Image J. The percent of a total monolayer (%ML) values were calculated based on the model of a close-packed monolayer of nanoparticles with an average core size of 1.6 nm and a 2-MEPA ligand length (l) of 0.65 nm, which gives an interparticle spacing ($2l$) of 1.3 nm and 0.14 cores/nm^2 for a close-packed monolayer without voids or interdigitation of the ligands.

After determining that oxygen plasma treatment restores the surface silanol content on thermal oxide nearly to the level observed on native oxide, based on Hf: [Si+O] ratios, we wanted to verify that the density of assembled nanoparticles increases with hafnium concentration by XPS and TEM. Table 3.1 lists the Au: [Si+O] ratios determined from XPS analysis for nanoparticles assembled onto hafnium-modified SiO_2. The gold content of the films increases with increased hafnium coverage, and the Au: [Si+O] ratios for plasma-treated thermal SiO_2 are comparable to that observed on native SiO_2. Table 3.1 also lists the nanoparticle coverage resulting from various surface treatments. Utilizing SiO_2 TEM grids developed in our laboratory[28] and treated under conditions identical to those used in our XPS studies, nanoparticle densities on thermal silicon dioxide surfaces were visualized using TEM (Fig. 3.1). These substrates allow TEM to be used as a surface analytical method for assessing the effectiveness of the surface treatments employed. The number of particles per unit area were counted, and it was determined that particle density within the film increases with the atomic concentration of hafnium. Because the strong covalent interaction between the phosphonic acid head group on the nanoparticle ligand shell and the Hf^{4+} surface species provides the driving force for nanoparticle assembly in this system, we expected that the density of Hf sites on the substrate would correlate strongly to the density of assembled nanoparticles.
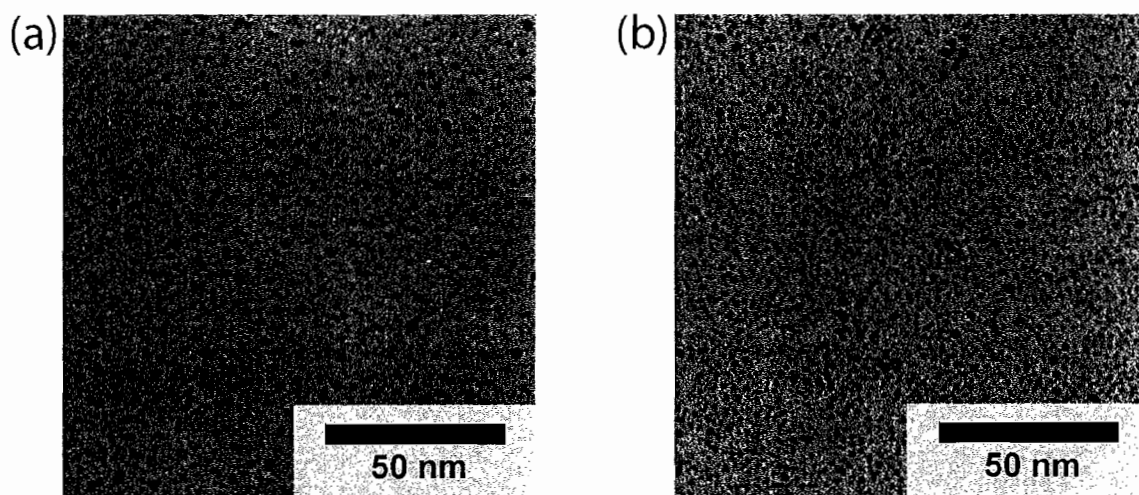
Figure 3.1. TEM images of phosphonic acid-derivatized gold nanoparticles on hafnium-modified silicon dioxide TEM grids. The particle density is much lower on untreated SiO_2 (a) than on substrates exposed to oxygen plasma and a wet chemical treatment (b). This is due to the higher surface concentration of hafnium linker on the treated sample and is in agreement with the higher Au: [Si + O] ratio observed by XPS.

We were able to significantly improve the density of assembled nanoparticles using oxygen plasma treatments, more than doubling the nanoparticle coverage from 27% of a full monolayer on untreated surfaces to 68% of a complete monolayer. While this is an improvement in the nanoparticle coverage and there are domains of close-packed particles (short-range order), there is no long-range crystalline order in these films. A significant fraction of voids (we estimate ~30%) can also be observed in the nanoparticle layer, but visual inspection suggests the assembled nanoparticles are dense enough to support electron transport across an in-plane electrode gap.

There are several reasons why long-range crystalline order might be difficult to achieve in these films. It is possible that the substrate is incompletely functionalized with hafnium. Voids in the hafnium(IV) layer would result in voids in the nanoparticle

monolayer. Additionally, because the particles are chemically anchored, there could be an energetic barrier to their reorganization on the surface resulting from the strong bonding interaction between the phosphonate head groups on the nanoparticle ligand shell and hafnium ions on the oxide surface. Several variations in self-assembly conditions (solvent mixtures, concentrations, temperature, and post-deposition annealing steps) were studied in attempts to promote reorganization of the particles into more well-ordered structures, but none of these attempts improved the long-range order or the nanoparticle coverage. Polydispersity has been shown strongly impact the ability of nanoparticles to organize into well-ordered structures in LB films, and it is possible that the polydispersity in the nanoparticles prepared for these studies limits the degree of order that can be realized in this system.[19] The assembled nanoparticles in our film had an average core size of 1.6 ± 0.6 nm, and it is likely that polydispersity disrupts close-packing in the film. LB films of nanoparticles in this size range also show a large area fraction of voids and structural disorder due to polydispersity.[19] While LB films of 1-2 nm particles exhibit some long-range order, dislocations and voids more significantly disrupt the continuity in those films than in these self-assembled nanoparticle monolayers. Another potential concern is that electron beam-induced sintering during TEM experiments could create some of the structural disorder observed in our studies. Small metal nanoparticles are known to sinter together under electron beam irradiation,[9] and this sintering process is observed after several minutes in our instrument. The extent to which sintering affects the size distribution and structural order of our nanoparticle

monolayers on the time scale of our imaging experiments has not yet been systematically determined, but it is likely a source of some of the observed structural disorder.

After maximizing the nanoparticle coverage obtained on thermal SiO_2 by our surface treatments, the nanoparticle layers appeared to be extended over several micrometers and dense enough to support electron transport across an electrode gap. Using the nanoparticle films comprising 68% of a full monolayer, we measured the current-voltage characteristics of the nanoparticle film. To contact the arrays, macroscopic gold electrodes (2 mm wide, 500 Å thick) with a 5-µm gap were evaporated onto the modified substrates by using a 5-µm tungsten wire as a shadow mask (Fig. 3.2).
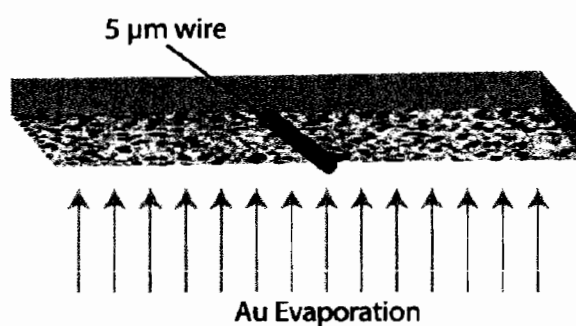
Figure 3.2. Schematic illustration showing the use of a 5-µm tungsten wire as a shadow mask for evaporation of macroscopic gold contacts onto the nanoparticle array.

In order to determine whether these films were dense enough to support electron transport across an in-plane electrode gap, current-voltage measurements were carried out using the macroscopic gold contacts. The nanoparticle films exhibited symmetric, nonlinear current-voltage properties, compared to a small background charging current

(~2 pA/V) observed in samples without nanoparticles present (Fig 3.3). Although our TEM studies led us to hypothesize that these films could support in-plane electron transport, we were somewhat surprised that electron transport could be measured over such a large electrode gap. This suggests the nanoparticle film extends continuously over the micrometer scale. One might not expect to observe a well-defined threshold voltage in such a large array because the large width of the electrodes relative to the length of the electrode gap creates a large number of charge transport pathways, with the lowest energy pathway determining the overall threshold voltage.[17,18] A clear current suppression region resulting from Coulomb blockade is not observed in these films.

In order to more clearly understand the charge transport characteristics of these assemblies, it will be instructive to utilize smaller, more well-defined electrode gaps on the order of 20-100 nm, patterned by electron beam lithography. The smaller dimensions of these electrode gaps allow for more accurate approximations of the number of particles in the active device region. This would not only allow investigations into the effect of ligand shell thickness on the electron transport in these types of nanoparticle arrays, but it would also allow any temperature dependence of the charge transport to be identified. It is possible that thermally activated charge transport processes (e.g., electron hopping, thermally-assisted tunneling) contribute to the overall charge transport characteristics of the system, giving rise to the observed non-zero current at very low biases. Future studies will focus on using electrode gaps patterned by electron beam lithography to investigate the nature of the charge transport in these films in more detail. The study of charge transport in this class of surface-bound nanoparticle films is made possible by our

surface modification strategy. We were able to improve the surface silanol coverage on thermal SiO$_2$, thereby significantly improving the nanoparticle coverage to the extent that in-plane electron transport is supported over the micrometer-scale in these assemblies.

Current vs. Voltage
Gold Nanoparticle Monolayer on Hf-SiO$_2$
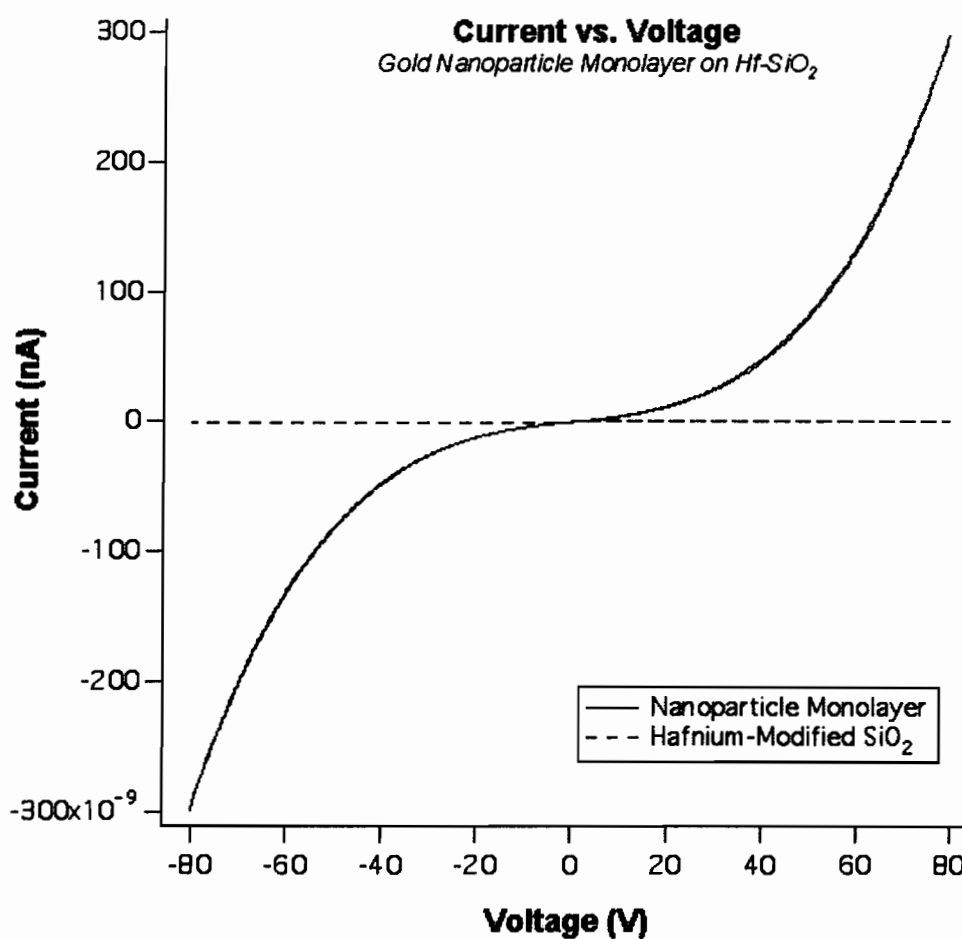
Figure 3.3. Current–voltage curve from a monolayer of 2-MEPA functionalized gold nanoparticles assembled onto hafnium-modified SiO$_2$. The measured IV curve is symmetric about the y-axis and shows nonlinear behavior; however, a Coulomb blockade region is difficult to define in such a large array of particles, and charge transport mechanisms other than tunneling might contribute to non-zero currents observed in the expected current suppression regime at low biases.

Conclusions

In summary, we have maximized the assembly of functionalized gold nanoparticles on hafnium-modified thermal silicon dioxide by developing surface silanol regeneration treatments. XPS analysis confirms that oxygen plasma treatments improve the reactivity of thermal silicon dioxide toward $HfOCl_2$ nearly to the level observed for native silicon dioxide. We propose that physical plasma treatment etches the topmost layers of the thermal oxide, exposing reactive surface species that are converted to silanol groups when the surface is hydrated. By utilizing SiO_2 TEM grids to assess the nanoparticle coverage on the hafnium-modified surface, we were able to determine that this surface treatment strategy more than doubled the coverage of nanoparticles from 27% to 68% of a full monolayer. The nanoparticle assemblies obtained by this approach extend over the micrometer scale and are sufficiently dense to support in-plane electron transport across a micrometer-scale electrode gap. Currently, we are examining this charge transport in greater detail by examining the effects of ligand shell thickness on the self-assembly and charge transport characteristics of this system. In addition, we will take advantage of this surface modification approach to examine post-deposition modification strategies on these robust nanoparticle films.

Bridge

After demonstrating the effectiveness of the surface modification strategy described in Chapter III, we wanted to examine other applications for our selective self-assembly strategy based on designed particle-substrate interactions. Because

functionalized nanoparticles had been selectively assembled on lithographically-defined hafnium(IV) patterns on SiO_2 in previous work in the Hutchison laboratory, we thought that gold nanoparticles could be assembled onto other patterned oxides. Chapter IV describes the directed self-assembly of functionalized gold nanoparticles onto patterned zinc oxide substrates. We demonstrate the growth of vertical zinc oxide nanowire arrays from ZnO seed films using the vapor-liquid-solid growth method and chemically anchored gold nanoparticles as the growth catalysts. This work was carried out with one of our collaborators from Sony Corporation in Japan, Dr. Daisuke Ito.

CHAPTER IV

SELECTIVE GROWTH OF VERTICAL ZINC OXIDE NANOWIRE ARRAYS USING

CHEMICALLY ANCHORED GOLD NANOPARTICLES

Note: The contents of Chapter IV are expected to appear in an upcoming publication, co-authored by Ito, D., Jespersen, M. L., and Hutchison, J. E., which has been submitted to *ACS Nano*. D. Ito conceived the nanowire synthesis method described, carried out nanowire growth experiments, and conducted most of the analyses reported. The first author also wrote the majority of the manuscript corresponding to Chapter IV. M. L. Jespesen devised and carried out the surface patterning and directed self-assembly experiments essential to this work and authored a significant portion of the manuscript. Both M. L. Jespersen and J. E. Hutchison provided experimental and editorial guidance.

Introduction

Self-assembled nanostructures have attracted much attention due to their wide range of potential applications in optics, electronics, and catalysis.[1-4] Zinc oxide is a particularly attractive material for optical devices that operate at room temperature because ZnO has a wide band gap (3.37 eV) and large exciton binding energy (60 meV). There have been many reports on different types of self-assembled zinc oxide nanostructures.[5-11] Among these structures, vertically aligned ZnO nanowire arrays are promising candidates for applications in nanoscale transistors,[12] sensors,[13] light emitting devices,[9,14] and field emitting devices.[15] In order to realize these and other applications,

techniques are necessary that permit vertical alignment, enable selective growth, are low

cost, and have potential for large-scale fabrication. Recently, aligned ZnO nanowires

have been synthesized by various processes, such as metal-organic vapor-phase epitaxy,[16]

thermal evaporation,[17] electrochemical deposition,[18] and vapor-liquid-solid (VLS)

deposition.[19] In each of these deposition processes, a patterned evaporated gold film is

used as a catalyst for the selective growth.[19] Although selectively placed ZnO nanowire

arrays show promise for use in novel devices, the use of evaporated gold films as a

catalyst presents a couple of disadvantages, including a lack of control over the diameter

and density of nanowires and the generation of large amounts of gold waste. The use of

self-assembled gold nanoparticle films as catalysts can potentially address these

disadvantages,[20] by reducing the amount of gold needed to produce the catalyst film,

offering an approach to selectively deposit nanowires in specific locations, and providing

opportunities to control the diameter and density of nanowires through variation of the

density and/or size of the assembled nanoparticle precursors. Thus far, growth of ZnO

nanowire arrays using self-assembled monolayers of gold nanoparticles has not been

described.

In this article, we demonstrate the selective growth of vertical ZnO nanowires

using self-assembled arrays of gold nanoparticles. The particles are modified with a

terminally functionalized thiol ligand shell, 2-mercaptoethylphosphonic acid (2-MEPA),

that selectively binds to a patterned ZnO seed layer to fabricate the vertical arrays on a

SiO_2 substrate (Fig. 4.1). Because ZnO exhibits spontaneous polarization in the wurtzite

structure and Si and SiO_2 have no surface charge, the phosphonic acid-functionalized

gold nanoparticles assemble onto the ZnO surface selectively. The utilization of the seed layer as a pattern and the functionalized gold nanoparticles as catalyst allows one to realize selectively positioned, vertical ZnO nanowire arrays without the disadvantages described for arrays derived from patterned evaporated gold layers.
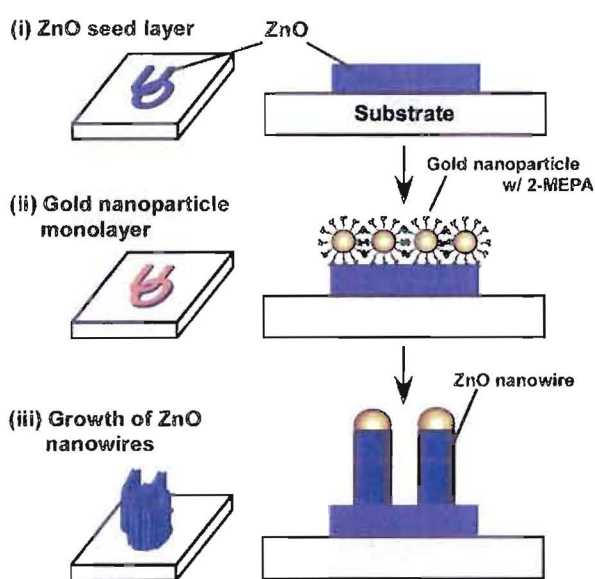
Figure 4.1. Schematic diagram of selective growth of ZnO nanowires on a chemically anchored array of gold nanoparticle catalysts.

Experimental

Nanoparticle Synthesis and Functionalization. Gold nanoparticles ($d_{core} = 1.4 \pm 0.4$ nm) were synthesized and functionalized with 2-mercaptoethylphosphonic acid (2-MEPA) as described previously.[21,22] Briefly, hydrogen tetrachloroaurate trihydrate ($HAuCl_4 \cdot 3H_2O$, 1.00 g, 2.54 mmol) in water reacts with triphenylphosphine (PPh_3, 2.33 g, 8.88 mmol) in toluene in the presence of the phase-transfer catalyst

tetraoctylammonium bromide (TOAB, 1.40 g, 2.56 mmol). Reduction with $NaBH_4$ (1.99 g, 52.6 mmol) yields 1.5 ± 0.4 nm PPh_3-stabilized gold nanoparticles. The PPh_3-stabilized particles were dissolved in dichloromethane, mixed with one mass equivalent of 2-MEPA dissolved in water, and stirred for 48 hours. When the organic layer was nearly colorless, the aqueous layer was separated, washed with dichloromethane, and purified by diafiltration using a 10 kD diafiltration capsule (Pall Life Sciences) and approximately 50 volume equivalents of deionized water.[23] Nanoparticles were considered pure when no free ligand was evident by ^1H NMR. The nanoparticle solution was diluted with deionized water to achieve the desired concentration for substrate soaking solutions.

Preparation of ZnO Films. ZnO seed films were deposited on Si substrates possessing a 3-μm SiO_2 layer by spin coating of a sol-gel precursor followed by an annealing step. The synthesis of a sol-gel precursor for ZnO has been reported by Kamalasanan et al.[24] Zinc acetate dihydrate $((CH_3COO)_2Zn \cdot 2H_2O)$ (5 g, 22 mmol) was dissolved in 2.5 mL ethylene glycol, and the mixture was heated at 150 °C for 15 min in a condensation system. After cooling the transparent solution to room temperature, 8 mL 1-propanol and 0.2 mL glycerol were added, followed by 5 mL triethylamine and 0.1 mL water. The resulting solution was stirred at 35 °C for 30 h. This precursor solution was diluted with isopropanol to a concentration of 50 mM, and ZnO seed layer films were prepared by spin coating of this solution at 3000 rpm for 60 seconds onto a 1-cm^2 wafer. The spin coated films were pre-baked at 150 °C for 10 min to drive off solvent and then baked at 350 °C for 30 min to obtain c-oriented ZnO seed films. Patterned ZnO seed films were prepared by photolithographic patterning of the substrate, followed by ZnO

seed film deposition and lift-off of the photoresist prior to annealing at 350°C for 30 min. Patterned ZnO surfaces were treated with UV-ozone for five minutes and rinsed with deionized water to remove adventitious carbon contamination[25] prior to immersion in an aqueous gold nanoparticle solution (0.25 mg/mL). The samples were rinsed with copious amounts of deionized water to remove any physisorbed or unbound particles and then dried under a stream of nitrogen prior to further modification or analysis.

Synthesis of ZnO Nanowire Arrays. ZnO nanowire arrays were grown by the VLS method. A mixture of ZnO and carbon powder was placed in a small quartz tube as a ZnO source, and the ZnO substrate was placed downstream from the source. The substrate temperature was controlled at 600 °C. The source temperature was raised to 900 °C and held for 20 min in N_2 gas flow (2.5 SCFH). Then, the furnace was shut down and cooled to room temperature while maintaining the nitrogen flow.

Results & Discussion

Figure 4.2 shows TEM images of gold nanoparticles (a) with PPh_3 ligand shell and (b) with 2-MEPA ligand shell following ligand exchange. TEM images indicate that the size distribution and dispersity of gold nanoparticles are similar before and after ligand exchange, exhibiting average diameters of 1.3 nm and 1.4 nm, respectively. As mentioned above, the 2-MEPA ligand is used as an anchoring agent between the gold nanoparticles and the ZnO surface (Figure 4.1). This ligand was shown to anchor gold nanoparticles selectively to hafnium-modified silicon dioxide in our previous work.[26] Others have reported the self-assembly of alkylphosphonic acid monolayers on indium

tin oxide[27,28] and a range of other oxide surfaces,[29-31] as well as on hafnium-modified SiO$_2$.[32]
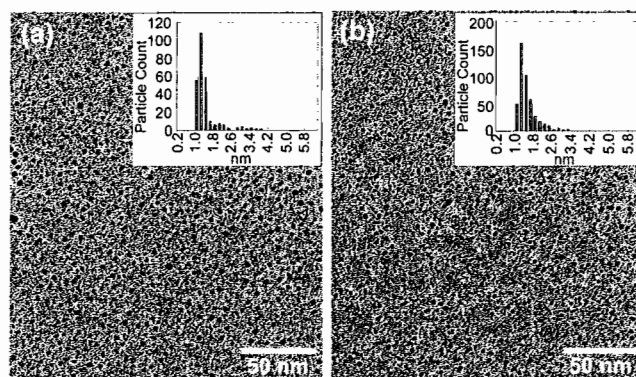
Figure 4.2. TEM images of gold nanoparticles (a) with PPh$_3$ ligand shell and (b) with 2-MEPA ligand shell. TEM images were acquired using a Philips CM12 Transmission Electron Microscope operating at an accelerating voltage of 120 kV.

To assemble the arrays, c-oriented ZnO patterned substrates are immersed into the 0.25 mg/mL gold nanoparticle solution for 10 seconds. Figure 4.3 shows TOF-SIMS positive ion mapping images for Zn^{2+} and Au^{3+} ions showing that the gold nanoparticles are anchored onto ZnO selectively. The ZnO surface is covered by a nanoparticle layer within 10 seconds, and no gold particles are observed on the bare SiO$_2$ substrate. Table 4.1 shows TOF-SIMS quantitative analysis of ion yields for a series of immersion times in gold nanoparticle solution. In this analysis, the peak intensities for ionic fragments of interest are divided by total ion intensity in each measurement to compare the relative compositions among samples. Peaks for Zn^{2+} and Au^{3+} positive ions and PO^{3-} and S^{2-} negative ions are observed even if the immersion time is only one second. The ratio of

Au to Zn is constant and independent of immersion time (Table 4.1), indicating the reaction time is less than one second. In our previous results on hafnium-modified SiO_2, the time required to achieve the maximum coverage of nanoparticles was approximately five days.[26]

This patterned, chemically anchored system provides a number of advantages over previously reported methods. Because terminal functionality of the thiol ligand shell dictates the interactions of the particles with the substrate, a number of specific and selective particle-substrate interactions for the generation of nanostructures can be envisioned. Since this system uses only the amount of gold required to cover the seed layer, the amount of generated gold waste is much smaller than in vapor deposition systems (approximately 16,000-fold reduction).[†]

(a) Zn^{2+} ion   (b) Au^{3+} ion
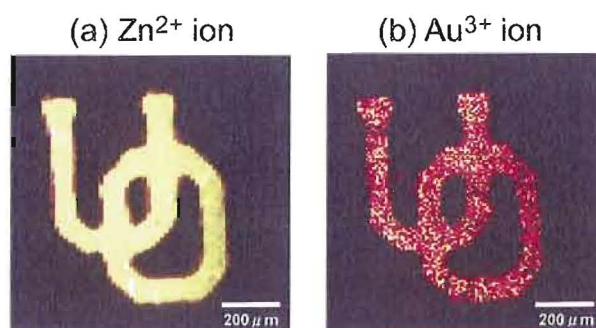
Figure 4.3. TOF-SIMS positive ion mapping images for Zn^{2+} and Au^{3+} ions. TOF-SIMS images were acquired with an ION-TOF Model IV Spectrometer using a bismuth liquid metal ion gun as the primary ion beam, operated at an accelerating voltage of 5 kV.

[†] Less than 50 µL of gold nanoparticle solution (0.25 mg/mL) was used for the preparation of zinc oxide nanowires in each experiment. The mass of gold consumed is less than 12.5 µg in this case. The source amount of gold in an evaporation system is about 0.2 g. So, the mass of gold consumed by using nanoparticle solution is at least 16,000 times less than that consumed in an evaporation system for deposition of patterned gold films.

Table 4.1. TOF-SIMS quantitative analysis of film composition for a series of immersion times in gold nanoparticle solution. Each individual ion peak intensity has been normalized by the total ion count.

Immersion time	Zn^{2+}	Au^{3+}	PO_3^-	S^{2-}
1 s	480.6	22.8	2171.9	224.9
3 s	461.0	21.3	2115.5	200.4
10 s	455.6	21.1	2118.2	233.8
30 s	450.7	20.8	1943.9	266.3

Figure 4.4 shows SEM images of VLS-deposited ZnO nanowires grown on the nanoparticle-modified ZnO seed layer. ZnO nanowires grow vertically only on the patterned gold particle/ZnO layer. The regions of growth correlate with gold patterns observed by TOF-SIMS ion mapping (Fig. 4.3(a) and 4.3(b)). Thus, the nanoparticle-modified seed layer serves as a selective template for nanowire growth. The average diameter and the height of ZnO nanowires are 30 nm and 1 μm, respectively. The size distribution of the diameter is less than 10 nm. The height of the ZnO nanowires is controllable from 100 nm to a few micrometers by varying the growth time. Figure 4.5 shows SEM images of ZnO grown by VLS with and without modification by nanoparticles. The VLS-deposited ZnO without gold nanoparticle modification shows the hexagonal columnar structure of ZnO (Fig. 4.5(b)), while the nanoparticle-modified ZnO shows a nanowire array (Fig. 4.5(c)). ZnO deposited by VLS method onto bare SiO_2 without a ZnO seed layer immersed in nanoparticle solution shows no structure (Fig.

4.5(a)). These results indicate that the gold nanoparticle array works as a catalyst for the growth of ZnO nanowires. The ZnO seed layer works as a template to fabricate vertical arrays and by anchoring the nanoparticles selectively.
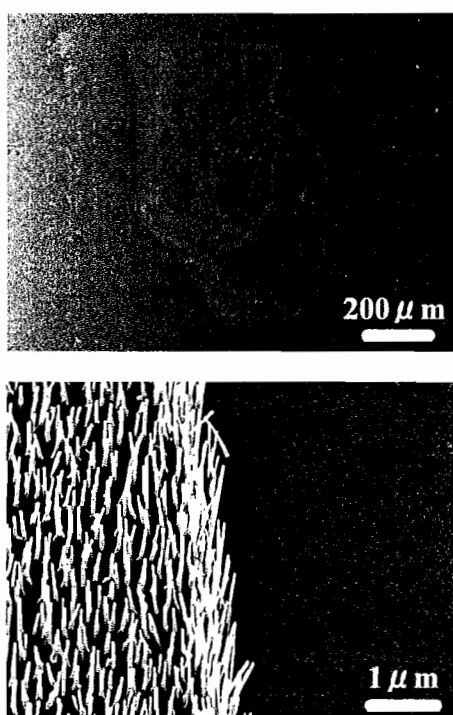
Figure 4.4. SEM images of VLS-deposited ZnO after immersion of substates into the gold nanoparticle solution for 10 seconds: (a) low magnification, (b) high magnification image, taken at a 30° tilt angle. SEM images were acquired with a Zeiss Ultra Scanning Electron Microscope operated at an accelerating voltage of 5 kV.

In Fig. 4.5(c), the nanowire arrays are tilted slightly relative to the surface normal and are not uniformly parallel. This is an effect of the non-epitaxial underlying substrate. Figure 4.5(d) shows vertical arrays on a c-sapphire substrate with a nanoparticle-modified ZnO layer. The alignment of the nanowires is more uniformly parallel and perpendicular to the underlying epitaxial substrate.
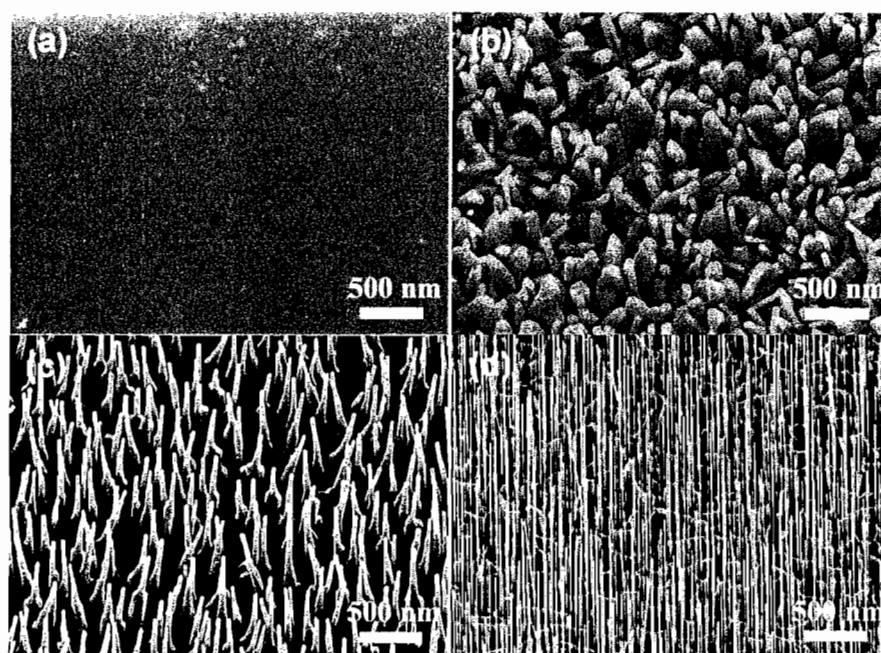
Figure 4.5. SEM images of VLS-grown ZnO (a) on SiO_2, (b) on an unmodified ZnO seed layer, (c) on a gold nanoparticle-modified ZnO seed layer on SiO_2, and (d) on a nanoparticle-modified ZnO seed layer on c-sapphire. SEM images were acquired with a Zeiss Ultra Scanning Electron Microscope operated at an accelerating voltage of 5 kV.

Photoluminescence (PL) measurements were performed at room temperature using 300 nm as the excitation wavelength. Figure 4.6 shows photoluminescence spectra of (a) VLS-grown ZnO on SiO_2, (b) VLS-grown ZnO grains from a bare ZnO seed layer, and (c) VLS-grown ZnO nanowires derived from a gold nanoparticle-modified ZnO seed layer. These samples are identical to those in Fig. 4.5. Only samples with ZnO nanowires (Fig. 4.6(c)) show a strong UV peak at 3.27 eV (379 nm). The UV emission band can be attributed to a near band-edge transition of ZnO, namely the recombination of free excitons through an exciton–exciton collision process.[10] The strong UV emission in the PL spectrum indicates that the ZnO nanowires are of good crystal quality with few

oxygen vacancies. In Fig. 4.6(a), the SiO_2 substrate immersed only in gold nanoparticle

solution showed no luminescence in the visible region. These results suggest that the

selective anchoring system is suitable for developing optical devices using patterned ZnO

nanowire arrays.
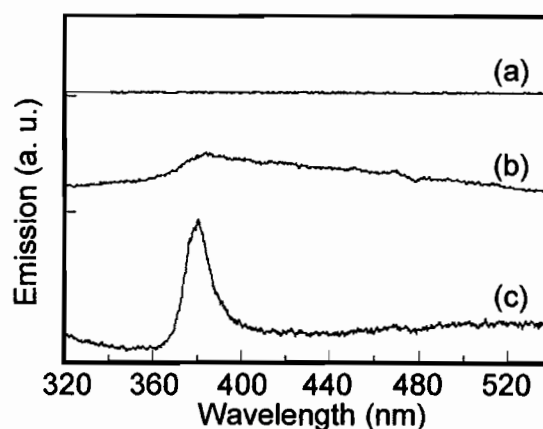
Figure 4.6. Photoluminescence spectra of (a) VLS-grown ZnO on SiO_2, (b) VLS-grown ZnO grains from unmodified ZnO seed films, and (c) VLS-grown ZnO nanowire arrays using nanoparticle-modified ZnO seed films. Photoluminescence measurements were carried out using a xenon lamp as the light source, with an excitation wavelength of 300 nm.

Conclusions

In summary, the selective anchoring of gold nanoparticles enables patterned

growth of ZnO nanowire arrays. A layer of phosphonic acid-functionalized gold

nanoparticles is deposited onto a ZnO seed layer in less than one second. The obtained

vertical ZnO nanowire arrays show strong UV luminescence with near band-edge energy.

User-defined arrays of this sort should be useful for sensors and field emitting devices, as

well as light emitting devices. This self-assembled system is able to incorporate many

different specific ligand-substrate interactions. Therefore, it should be useful for fabricating a range of oxide, nitride, and carbon nanostructures that are generated through a catalyst growth mechanism. In addition, use of self-assembled gold nanoparticles as the growth catalyst may enable the tuning of nanowire diameter and spacing through control of nanoparticle core diameter, ligand shell length, and growth temperature. This growth technique also poses benefits for low-cost, low-waste manufacturing.

Bridge

Up through the time of the studies described in Chapter IV, we had demonstrated through the use of particle-substrate interactions and directed self-assembly that it was possible to assemble monolayers of nanoparticles for two important applications: nanoparticle-based electronic devices (Chapter III) and selective growth of high-quality nanostructures using gold nanoparticles as the growth catalyst (Chapter IV). We next directed our efforts toward the manipulation of the nanoparticle-environment interface. Our initial experiments for post-deposition modification of surface-bound gold nanoparticles were based on thiol-thiol ligand exchange reactions. This research is discussed in Chapter V.

CHAPTER V

THIOL-THIOL LIGAND EXCHANGE REACTIONS ON SURFACE-BOUND GOLD

NANOPARTICLE MONOLAYERS

Note: The contents of Chapter V are expected to appear in an upcoming publication, co-authored by Jespersen, M. L. and Hutchison, J. E. The first author designed and carried out all experiments described herein. The first author also composed the manuscript corresponding to Chapter V. J. E. Hutchison provided experimental and editorial guidance. All materials syntheses and the majority of subsequent characterization were carried out at the University of Oregon, with some analysis performed at the Surface Characterization and Nanofabrication Laboratory at the University of Utah.

Introduction

A broad range of surface modification strategies are required to control the

interfacial properties of nanoscale materials and to allow their integration into useful

devices and materials applications.[1] Metal nanoparticles, in particular, have generated a

great deal of interest due to their unique size-dependent properties, which make them

promising candidates for use in catalysis,[2-4] electronics,[5-7] optics,[8,9] and sensors.[10]

Methods for the reliable assembly of nanoparticles and control over their interactions

with surfaces are required in order to take advantage of those properties in bottom-up

assembly strategies. In addition, techniques for controlling the interactions of self-

assembled arrays of nanoparticles with the surrounding environment will be necessary in order to explore the sensing capabilities of those systems,[10-12] interface them with other nanostructures,[13] improve their stabilities in a range of environmental conditions, and improve the durability of supported gold nanoparticle catalysts.[14,15] The surface chemistry required to assemble gold nanoparticles on surfaces, however, may not be optimal for promoting particular interfacial interactions with the environment. Instead, it is probable that tailoring nanoparticle-environment interactions will require the introduction of new surface functionalities to pre-assembled particles.

The solubility and assembly properties of gold nanoparticles are generally controlled by the terminal functionality of a protecting ligand shell, and it is natural that the same strategies employed in functionalizing nanoparticles in solution could be applied to introduction of new terminal functionalities to nanoparticle assemblies. Modification of gold nanoparticle surfaces with self-assembled monolayers (SAMs) is an effective route for tailoring the interactions of nanoparticles with their environments in solution. There are many examples of gold nanoparticles stabilized by SAMs of organothiolates,[16] organophosphines,[17-19] and organoamines.[20] Thiolate monolayers, in particular, have been extensively studied for the surface modification of gold nanoparticles to afford a library of materials with a wide range of terminal functional groups.[16, 21-23] The stabilizing ligand shell can be incorporated directly during the synthesis of the particles,[22,24,25] or post-synthesis through facile ligand exchange reactions.[16,20,21,23,26] While it is possible to design selective particle-substrate interactions through incorporation of specific terminal functionalities in the particle ligand shell[12,27] or

through electrostatic interactions,[28-30] thiol-thiol ligand exchange reactions for post-deposition modification of these nanoparticle assemblies has not yet been reported. One approach to engineering the nanoparticle-environment interface could be to immobilize two-dimensional assemblies of nanoparticles on surfaces by directed self-assembly and then introduce new functionality through ligand exchange chemistry.

In addition to thiol ligand exchange reactions on gold nanoparticles in solution, surface modification strategies based on thiol-thiol exchange have been studied on planar, polycrystalline gold surfaces, where the total surface area of gold is much lower than in solutions of gold nanoparticles. Based on research involving the exchange of ferrocene-terminated alkanethiols for long-chain alkanethiols[31,32] and for other adsorbates,[33,34] it has been established that exchange reactions occur first in regions of the SAM that are not perfectly crystalline (i.e., along step edges or grain boundaries) due to the lower packing density at these sites. This first exchange process is followed by a much slower exchange involving replacement of thiols at terrace sites within crystalline domains. Results from these studies are similar to those observed for place exchange reactions on thiol-protected gold nanoparticles,[35,36] where the fraction of reactive defect sites relative to terrace sites of crystalline domains increases with decreasing particle size. Given the utility of thiol-thiol exchange reactions on planar gold substrates and on gold nanoparticles in "bulk" solutions, it is reasonable to assume that thiol-stabilized gold nanoparticles immobilized on planar substrates via chemical bonding should readily undergo ligand exchange with incoming thiol ligands. In addition, it is expected that the particles will not desorb during post-assembly chemical modification of their surfaces because they are anchored to the

substrate. If the extent of such ligand exchange processes on surface-bound nanoparticles can be controlled, it should be possible to impart differential chemical functionality to surface-bound nanoparticles.

Our strategy is to assemble surface-bound monolayers of gold nanoparticles and then introduce new functionality through thiol-thiol ligand exchange reactions to tailor their surface properties. It has been previously demonstrated that silicon dioxide modified with hafnium(IV) guides the assembly of patterned gold nanoparticle monolayers that are dense enough to support electron transport across an in-plane electrode gap.[27,37] By taking advantage of the strong interaction between the phosphonate terminal functionality of the nanoparticle ligand shell and the hafnium(IV) layer on SiO_2, it is possible to assemble extended monolayers of nanoparticles that are covalently bonded to the underlying substrate. There are several advantages to assembling monolayers of nanoparticles in this fashion, when compared to Langmuir-Blodgett and Langmuir-Schaefer techniques,[38-40] kinetically driven self-assembly,[41,42] or interfacial capillary force-driven assembly,[43] all of which can be time-consuming, difficult to precisely control, or require external forces in order to produce ordered films. Nanoparticle monolayers assembled through covalent interactions with the substrate are patternable and readily obtained. They form by common solution phase self-assembly methods directly onto the target substrate and do not rely on transfer of nanoparticles from one substrate to another. Since the nanoparticle monolayers previously described are chemically bound to the surface, this opens up the possibility of modifying the exposed surfaces of the particles by exchanging the upper ligands for a variety of

functionalized thiols to tailor the interactions of the nanoparticles with the environment above the plane of the monolayer.

Here we report ligand exchange reactions carried out on surface-bound gold nanoparticle monolayers to yield stationary films of topochemically functionalized nanoparticles. Functionalized gold nanoparticles bearing phosphonic acid terminal groups are assembled onto hafnium-modified silicon dioxide substrates, and their surfaces are modified through ligand exchange reactions in solution. Contact angle measurements show the surface properties of the nanoparticle films can be manipulated. We use x-ray photoelectron spectroscopic analysis to investigate the changes in elemental composition of the nanoparticle layer, while TEM analysis indicates the nanoparticles remain firmly anchored to the substrates on which they are assembled, suggesting only the top surfaces of the nanoparticles undergo ligand exchange. This method for introducing new functionality to gold nanoparticles pre-assembled on surfaces should find many useful applications in the development of nanoparticle-based sensors and the preparation of new types of nanomaterials, such as small (1-2 nm) Janus nanoparticles. In addition, since the films consist of discrete gold particles, this strategy should enable sophisticated self-assembly schemes for the formation of mixed SAMs with non-interdiffusable domains for molecular electronics or biochip applications.

Experimental

Materials. Hafnium dichloride oxide octahydrate (Alfa Aesar; 99.998%), 1-octadecanethiol (Aldrich, 98%), 1-octanethiol (Aldrich, 98.5%), 1-propanethiol (Aldrich,

99%), and *1H,1H,2H,2H*-perfluorodecanethiol ([HS(CH$_2$)$_2$(CF$_2$)$_8$F]; Aldrich, 97%) were used as received. 2-Mercaptoethylphosphonic acid [HS(CH$_2$)$_2$P(O)(OH)$_2$] was synthesized as previously reported.[27] Deionized water (18.2 MΩ-cm) was purified with a Barnstead Nanopure system. Dichloromethane was distilled from calcium hydride. Water, absolute ethyl alcohol (Aaper), and hexane (Burdick & Jackson) were sparged with nitrogen for approximately 20 minutes prior to use.

Nanoparticle Synthesis and Functionalization. Gold nanoparticles (d$_{core}$ = 1.5 ± 0.5 nm) were synthesized first as triphenylphosphine-stabilized precursors according to a previously described synthesis.[17,19] Ligand exchange was carried out in a biphasic system, starting with 186 mg (~7.2 µmol) of the as-prepared gold nanoparticles in 60 mL dichloromethane and 148 mg (1.04 mmol, 144 molar equivalent) 2-mercapto-ethylphosphonic acid in 100 mL H$_2$O maintained at a pH of ~ 7.4 using a KH$_2$PO$_4$/K$_2$HPO$_4$ buffer. The biphasic solution was stirred for 48 hours until the organic fraction was clear and no insoluble material was observed as a foamy interphase, indicating completion of the exchange reaction. The aqueous and organic fractions were separated, and the aqueous fraction was washed with dichloromethane (3 x 50 mL). Residual dichloromethane was removed by rotary evaporation. In order to remove excess free ligand and buffer ions, the water-soluble nanoparticles were purified by a diafiltration process described elsewhere[44] using a 10 kD diafiltration capsule (Pall Life Sciences). The nanoparticle solution was concentrated to 30 mL and filtered with 50 volume equivalents (1.5 L) of deionized water. The purified product solution was

concentrated to 20 mL and lyophilized overnight. ^{1}H NMR confirms the completion of the exchange reaction and the removal of free ligand from the product.

Preparation of Substrates. The Si substrates used in this study were cut from n-type <100> wafers with 10-20 Ω-cm resistivity and a 3-μm thermal oxide (University Wafer, Boston, MA). Silicon dioxide TEM grids were prepared as previously reported.[45] The SiO_2 surfaces were cleaned using an oxygen plasma treatment (150W, 200 mT, 20 sec), followed by immediate immersion in a cleaning solution of 100:4:1 H_2O: 30% H_2O_2: 30% NH_4OH for two hours at 70 °C.[37] The substrates were then rinsed with deionized water and transferred immediately to a 5 mM aqueous solution of $HfOCl_2$ for four hours at 45 °C. Following this surface modification step, the substrates were rinsed with water and transferred to a solution of 2.0 mg nanoparticles per milliliter of 3:1 MeOH: H_2O for 24 hr at room temperature. Following nanoparticle assembly, the substrates were removed from solution, rinsed with copious amounts of water, and dried under a stream of argon.

Ligand Exchange on Surface-Bound Nanoparticle Monolayers. Hafnium-modified silicon dioxide substrates with surface-bound phosphonate-derivatized gold nanoparticles were immersed in 1.5 mM, nitrogen-sparged ethanolic solutions of 1-octadecanethiol, 1-octanethiol, or 1-propanethiol while stirring. Wafers were removed at various times throughout the exchange reaction, sonicated for 5 min in ethanol to remove any physisorbed material, then rinsed with copious amounts of ethanol and deionized water, and finally dried under a stream of argon prior to analysis. For exchange reactions with *1H,1H,2H,2H*-perfluorodecanethiol, substrates were immersed

in a nitrogen-spaged, stirring solution of 1.5 mM $HS(CH_2)_2(CF_2)_8F$ in hexane and rinsed in a similar manner to those from the alkanethiol exchange reactions, with the addition of a hexane rinse.

Analysis Techniques. Contact angle measurements were conducted using a microscope equipped with a goniometer, utilizing the sessile drop method.[46] TEM images were acquired using a Phillips CM-12 microscope operating at 120 kV accelerating voltage. Nanoparticle size analysis was carried out using a procedure developed for ImageJ and described elsewhere.[47]

X-ray photoelectron spectroscopic measurements were conducted using a Kratos AXIS Ultra Photoelectron Spectrometer (Kratos Analytical, Chestnut Ridge, NY) with a monochromated Al Kα x-ray source, operated at an accelerating voltage of 15 kV and an emission current of 15 mA. XPS region scans were acquired using a pass energy of 80 eV and 0.2 eV steps to maximize the signal-to-noise ratio.

Results & Discussion

In order to introduce new functionality to chemically anchored gold nanoparticle films, we first investigated ligand exchange reactions with alkanethiols as the incoming ligands. Because the pre-assembled particles contain hydrophilic functional groups (phosphonates) and the incoming alkanethiol ligands are hydrophobic, we anticipated the extent of ligand exchange could be monitored by contact angle measurements. One potential concern was that the nanoparticles would be desorbed during the exchange reaction, so we performed structural characterization of the films by TEM. These

analyses indicated the particles remain bound to the surface and that only the exposed ligands on the upper surfaces of the nanoparticles are modified. XPS analysis is utilized to quantify the extent of ligand exchange and suggests that although the gold nanoparticle surfaces can be modified and remain anchored to the substrate without observable changes in the average core size, they are likely asymmetrically etched. Finally, we extend this ligand exchange chemistry to perfluorinated alkanethiols to show that our strategy tolerates additional functionalized thiols.

Contact Angle and TEM Studies. Monolayers of phosphonic acid-derivatized gold nanoparticles were first assembled onto hafnium-functionalized SiO$_2$ substrates, followed by immersion in a solution of gold nanoparticles. This assembly method has been shown to yield dense, stable monolayers of nanoparticles that are chemically bound to the underlying substrate.[37] The nanoparticle films were then introduced into alkanethiol solutions to undergo thiol-thiol ligand exchange reactions (Scheme 5.1). The nanoparticle-modified substrates were removed from alkanethiol solution at different times throughout the exchange reactions, and their water contact angles were measured to determine the extent of ligand exchange. Before immersion in alkanethiol solutions, the phosphonic acid-terminated ligand shell surface was hydrophilic (15 ± 1 °). After immersion in alkanethiol solution, the contact angles increased with time until a maximum value was reached after approximately 4-5 hours (Fig. 5.1). The increased hydrophobicity of the surfaces indicates that hydrophilic phosphonic acid-containing ligands are exchanged for the more hydrophobic alkanethiols. Nanoparticle films remained immersed in solution for up to 24 hr. The maximum contact angle measured
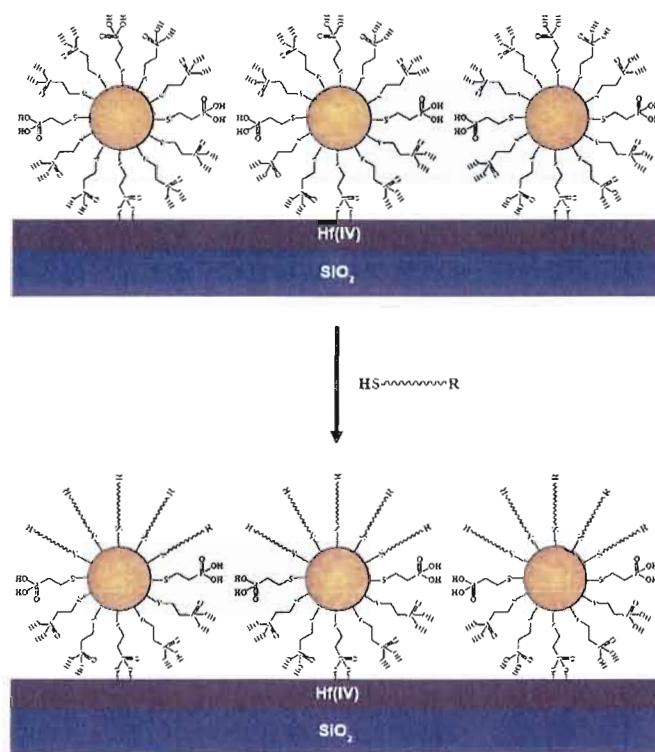
Scheme 5.1. Schematic illustration of ligand exchange on chemically-anchored gold nanoparticles. Surface-bound gold nanoparticles on hafnium-modified SiO_2 are immersed in dilute solutions of incoming thiol ligands, which exchange onto the exposed upper nanoparticle surface to yield topochemically functionalized nanoparticles.

after 24 hours increases with the chain length of the incoming alkanethiol. This trend is similar to that observed for alkanethiol monolayers on planar gold surfaces due to the increased ordering induced by van der Waal's interactions.[48,49] The maximum contact angles observed on the nanoparticle monolayer surface are lower than those observed on planar gold for well-packed monolayers of the same alkanethiols.[48] This result can be expected due to the higher curvature of the nanoparticle surface compared to planar gold. The same trend has been observed in post-deposition modification of citrate-stabilized gold nanoparticles deposited by polymer template-assisted assembly.[30]

Contact Angle vs. Immersion Time
Au101-2-MEPA NP on Hf/SiO2 in 1.5 mM Alkanethiol in EtOH
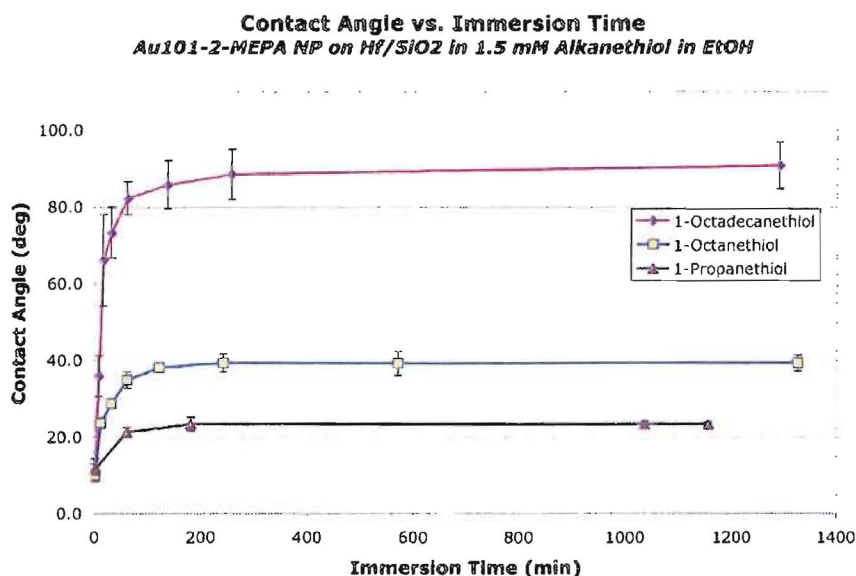
Figure 5.1. Water contact angles of nanoparticle monolayers as a function of immersion time in alkanethiol solution. The exposed phosphonic acid surfaces are hydrophilic, but the surfaces become increasingly hydrophobic with increased immersion time, as alkanethiol is exchanged onto the nanoparticle surface. The maximum contact angle obtained increases with chain length of the incoming alkanethiol ligand.

Contact angle measurements clearly indicated that the surface-bound nanoparticles undergo ligand exchange, but the extent of the exchange reaction was unknown. One potential concern was that the chemisorbed nanoparticles could be desorbed from the surface if the gold-thiol bonds on the lower surfaces of the particles were interrupted during the exchange reaction, thus disrupting the thiol-phosphonate linkage. In order to assess the stability of the nanoparticles to this exchange process, we conducted TEM imaging experiments of the modified nanoparticle films. Nanoparticle monolayers were assembled onto hafnium-modified SiO_2 TEM grids,[45] which were then immersed in stirring alkanethiol solutions for 24 hours. TEM images from before and

after the exchange reactions show that the nanoparticle films are stable to the exchange process (Fig. 5.2). The average core diameter before and after the exchange reactions were 1.3 ± 0.5 nm and 1.3 ± 0.4 nm, respectively. In addition, the density of nanoparticles on the surface did not change after 24 hours in alkanethiol solutions. This suggests that ligand exchange is only occurring on the exposed upper surfaces of the nanoparticles, while the lower surfaces remain chemically anchored to the surface through the thiol-phosphonate linker.
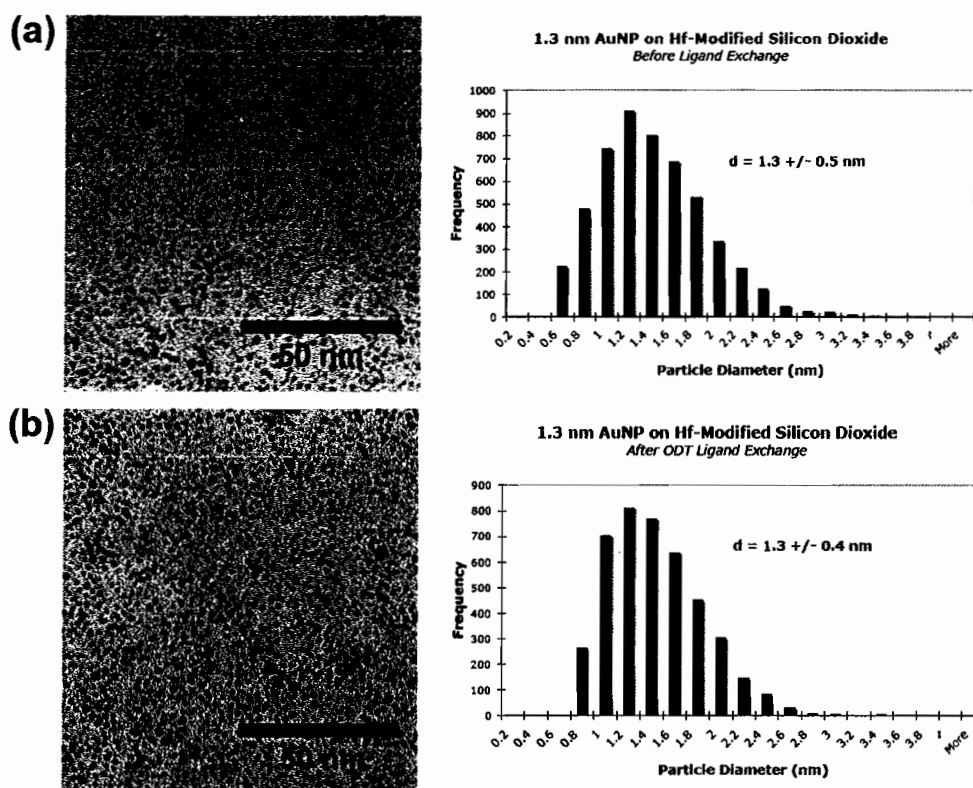
Figure 5.2. TEM images and size distributions for gold nanoparticle monolayers (a) before exchange and (b) after ligand exchange with octadecanethiol. The average core size is 1.3 nm (± 0.5 nm) in both cases. The density of cores per unit area is 0.1 cores/nm^2 both before and after ligand exchange.

The success of this approach to modification of the nanoparticle monolayer surface likely results both from steric crowding and from the relative concentrations of incoming and outgoing thiols. Figure 5.3 summarizes these effects. Given the large size of the incoming ligand relative to the interparticle spacing, it is unlikely that the incoming ligand can diffuse to the region near the particle-substrate interface, making only those sites on the top hemispheres of the particles accessible during the exchange. Additionally, the exchange likely proceeds readily on the exposed upper nanoparticle surface, as the outgoing ligand can rapidly diffuse away from the substrate into bulk solution. The relatively high concentration of incoming thiol drives the exchange reaction on the surface. In the region near the particle-substrate interface, the local concentration of surface-bound ligand is high, and in the event that a gold-sulfur bond were to be interrupted, the high local concentration of the stationary thiol-phosphonic acid would likely drive the immediate reformation of the Au-S bond. For these reasons, ligand exchange near the particle-substrate interface seems improbable. The stability of the surface-bound arrays in the presence of smaller incoming ligands like 1-propanethiol, which could much more easily diffuse into the particle-substrate interface region than a larger incoming ligand like octadecanethiol, suggests this could be the case.

XPS Composition Analysis Studies. To determine the extent of ligand exchange more quantitatively than by contact angle measurements, we utilized X-ray photoelectron spectroscopic analysis. Table 5.1 shows XPS composition data from nanoparticle monolayer substrates immersed in octadecanethiol solution as a function of immersion time. Two trends emerge from the XPS data. First, the atomic concentration of
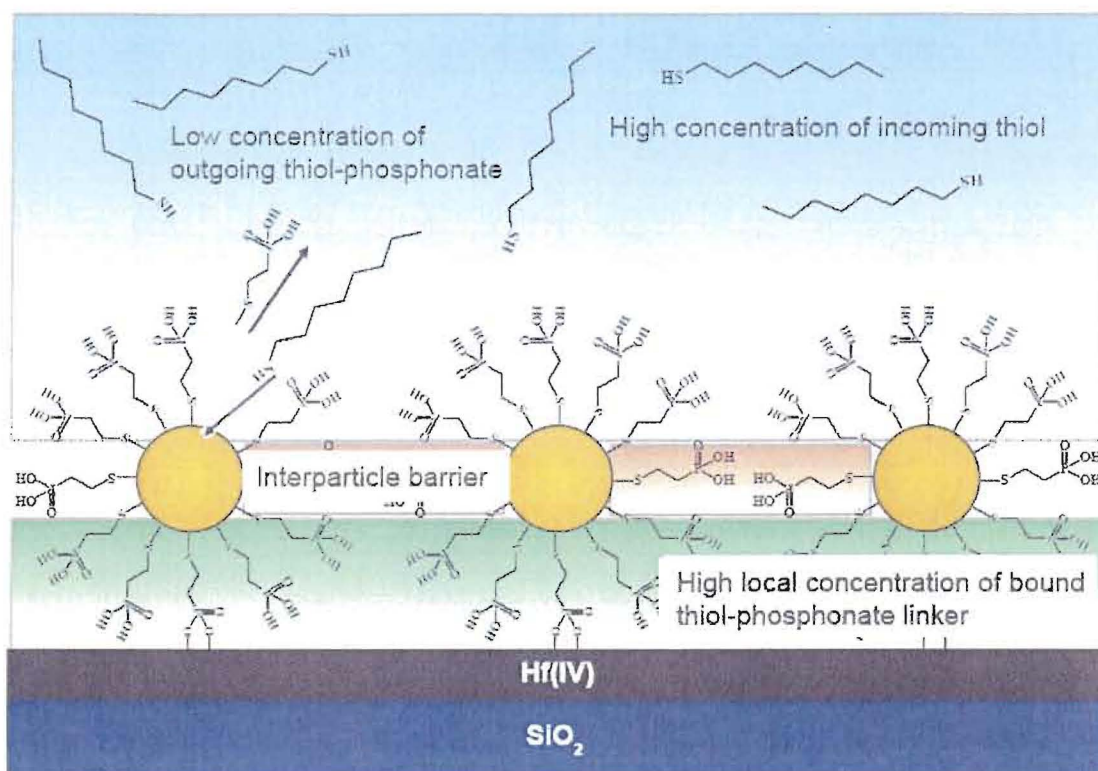
Figure 5.3. Schematic illustration summarizing the relative concentration and steric effects underlying the stability of surface-bound nanoparticle monolayers to thiol-thiol ligand exchange reactions. The high concentration of incoming thiol and extremely low concentration of the thiol-phosphonate in solution drives the exchange reaction on the upper surface. Diffusion to the particle-substrate interface is impeded, and the high local concentration of bound thiol-phosphonate linker makes nanoparticle desorption unlikely.

phosphorus decreases after 24 hr of the exchange reaction, while the atomic concentration of carbon increases, which is expected if the exposed thiol-phosphonates are replaced by alkanethiols with no phosphorus content and greater carbon content. The atomic concentration of sulfur is also constant within 0.1%, which is expected for a 1:1 exchange of thiols. Second, the atomic concentration of gold decreases throughout the exchange reaction with ODT. One might expect some attenuation of the gold signal due to the introduction of a thicker carbon overlayer of ODT, but this doesn't explain the

Table 5.1. Atomic concentrations determined by XPS for gold nanoparticle monolayers on hafnium-modified SiO_2 immersed in ODT solution. All reported values are percent atomic concentration (± 0.1%).

Immersion Time	Au 4f	P 2p	C 1s	S 2p	Hf 4d	Si 2p	O 1s
0 min	1.5	1.0	17.4	0.6	0.9	31.6	46.9
5 min	1.5	1.0	18.2	0.7	0.9	31.0	46.7
60 min	1.6	1.0	18.7	0.7	0.9	30.8	46.2
24 hr	1.2	0.8	19.5	0.6	0.9	30.5	46.5

trend because we would also expect the sulfur signal to be attenuated if this were the case. The atomic concentration of sulfur does not decrease even after 24 hr. Another explanation is that the ligand exchange reaction etches the gold nanoparticles. We were initially skeptical that the gold nanoparticles could have been etched, given the preservation of the average core size and size distribution throughout the exchange reaction, observed in our TEM studies. A closer examination of the ligand exchange reaction conditions, on the other hand, suggests it is not that surprising that the gold cores are etched to some degree throughout the exchange reaction. Decomposition of gold nanoparticles has been observed in ligand exchange reactions when the incoming thiol is present in high concentrations (300 molar equivalents or greater).[16] Given that the alkanethiol solutions used in our experiments were 1.5 mM in alkanethiol, and taking into account that the nanoparticles available for reaction were limited to those assembled as a *monolayer* on the surface of a 1 cm^2 wafer, it is clear that there is an extremely large excess (> 10^9 molar equivalent) of thiol ligand in solution.[†] This certainly suggests gold etching is possible in our experiments.

[†] Alkanethiol solutions for ligand exchange were 1.5 mM concentration and 150 mL volume, giving 0.23 mol of ligand in solution. The density of nanoparticles within the monolayer was approximately 0.11 cores/nm^2. For ten 1-cm^2 wafers, this gives 1.1 x 10^{14} nanparticles, or 1.8 x 10^{-10} mol. This represents a 1.3 x 10^9 molar excess of ligand.

Taken together, the contact angle and TEM data suggest that ligand exchange has occurred on the top surface of the nanoparticle film and that the nanoparticles remain chemically anchored to the substrate without exhibiting any change in the average core diameter. The XPS data for phosphorus, carbon, and sulfur are consistent with this model. The XPS data for gold and examination of the ligand exchange reaction conditions, however, suggest gold etching. One explanation for the decrease in gold concentration despite the apparent stability of the particles by TEM is that the nanoparticles are asymmetrically etched during ligand exchange (Fig. 5.4). By TEM, in which the nanoparticle layer is observed from the top down, asymmetric etching of the top surfaces of the particles would not necessarily result in a decrease of the observed average core size. Given our previous model (Fig 5.3), in which steric crowding from bound thiol-phosphonates limits access to the nanoparticle surface for relatively large incoming thiols, we hypothesized that smaller incoming thiols could access a greater fraction of the nanoparticle surface and perhaps etch the nanoparticles to a greater extent than long-chain alkanethiols.

In order to investigate the possibility of gold etching by incoming thiol ligands, we examined the composition of the nanoparticle films following exchange reactions using 1-octanethiol and 1-propanethiol. As previously shown, the water contact angles of the surfaces become increasingly hydrophobic with increased immersion time in alkanethiol solution, and the maximum water contact angles achieved after 24 hr increase with increasing chain length, as expected. We conducted XPS composition analysis of films immersed in solutions of 1-octadecanethiol, 1-octanethiol, and 1-propanethiol for
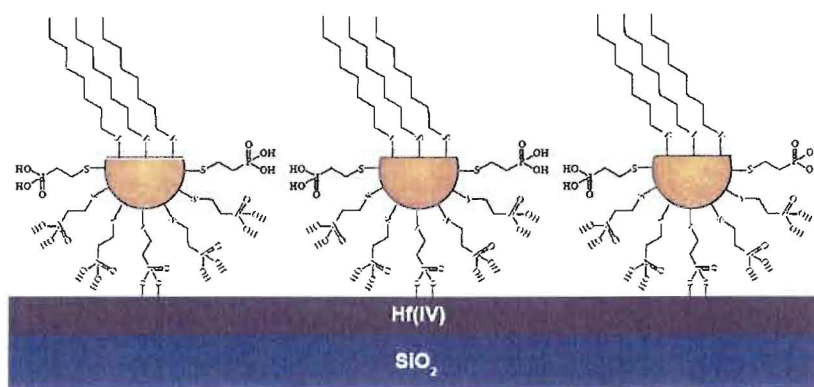
Figure 5.4. Schematic illustration of asymmetrically etched gold nanoparticles from ligand exchange reactions on chemically-anchored nanoparticles. The total surface area of the particle is decreased, thereby decreasing the number of thiols that can assemble onto the nanoparticle surface.

24 hours to examine the resulting changes in nanoparticle monolayer composition. Table 5.2 summarizes the XPS composition data from these experiments. The atomic concentration of gold decreases over 24 hr if alkanethiol is present in solution, as we also observed in our earlier experiments involving only ODT as the incoming ligand. It is interesting to note that the final atomic concentration of gold after 24 hr decreases with decreasing alkanethiol chain length. This is likely due to the ability of shorter-chain alkanethiols to access and etch the nanoparticle surface more easily than long-chain alkanethiols due to steric constraints induced by thiols exchanged onto adjacent particles (Fig. 5.5). Asymmetric etching of the upper particle surfaces would decrease the total surface area of the particles, along with the total number of thiols that could assemble onto the nanoparticle surface (Fig. 5.4). This is consistent with the decrease in sulfur concentration with decreasing chain length after 24 hr. The atomic concentration of

Table 5.2. XPS atomic concentration data determined for gold nanoparticle monolayers immersed in alkanethiol solutions for 24 hr. All reported values are percent atomic concentration (± 0.1%).

Incoming Thiol	Au 4f	P 2p	C 1s	S 2p	Hf 4d	Si 2p	O 1s
No Exchange	1.5	1.0	17.4	0.6	0.9	31.6	46.9
ODT	1.2	0.8	19.5	0.6	0.9	30.5	46.5
1-Octanethiol	1.1	0.8	15.4	0.5	1.0	32.1	49.2
1-Propanethiol	1.0	0.7	13.5	0.4	1.0	32.9	50.5

carbon diminishes with the chain length of the incoming thiol, as expected.[†] TEM studies indicated no change in average core size or number of particles per unit area for the exchange reactions with 1-octanethiol and 1-propanethiol. Again, we would not expect asymmetric etching of the nanoparticles to result in observable changes in the average core size or nanoparticle coverage because spherical particles and asymmetrically etched particles would appear the same from the top down by TEM. These data suggest that the nanoparticles are asymmetrically etched due to the large excess of incoming thiol in solution and that the extent of etching increases with decreasing chain length of the incoming thiol ligands.

Having demonstrated that the ligand exchange process with alkanethiols works to modify the surface properties of chemically anchored gold nanoparticles, we investigated semi-perfluorinated alkylthiols as another class of incoming ligands. Substrates with surface-bound monolayers of gold nanoparticles were immersed in a solution of *1H,1H,2H,2H*-perfluorodecanethiol. The contact angle of the nanoparticle film increases accordingly with immersion time in the thiol solution. XPS analysis shows that

---

[†] The atomic concentration of carbon does not scale exactly with alkyl chain length in our data because some portion of the C 1s signal originates from adventitious carbon.
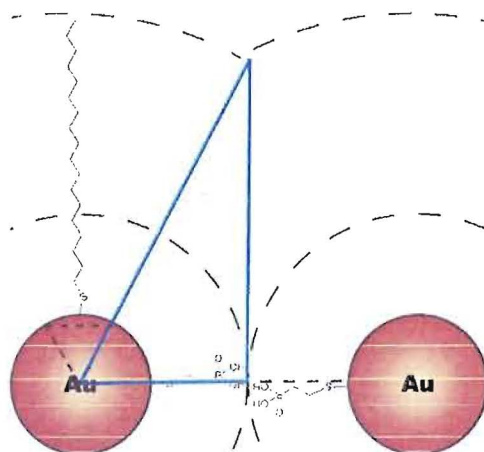
Figure 5.5. Illustration of two adjacent gold nanoparticles with 2-MEPA ligand shells. Also shown is a trace of the particle radius with an incoming ligand of n-octadecanethiol (ODT). Steric constraints dictate that the available surface area for incoming ODT consists of a small spherical cap on the topmost surface of the surface-bound nanoparticles. Based on the surface area of the cap, the maximum number of incoming ligands that can exchange onto a particle will increase with decreasing alkyl chain length of incoming ligand. Shorter-chain alkanethiols would be able to access a greater fraction of the total surface area of the nanoparticle.

the amount of fluorine in the film increases over the course of the exchange reaction up to 24 hr (Fig. 5.6), consistent with the chemisorption of a fluorinated overlayer. The atomic concentration of gold again decreases after ligand exchange (from 1.5 % to 1.3%), and the extent of the gold etching appears to be less than that observed for the short-chain alkanethiols, suggesting that the extent of gold nanoparticle etching varies inversely with chain length.
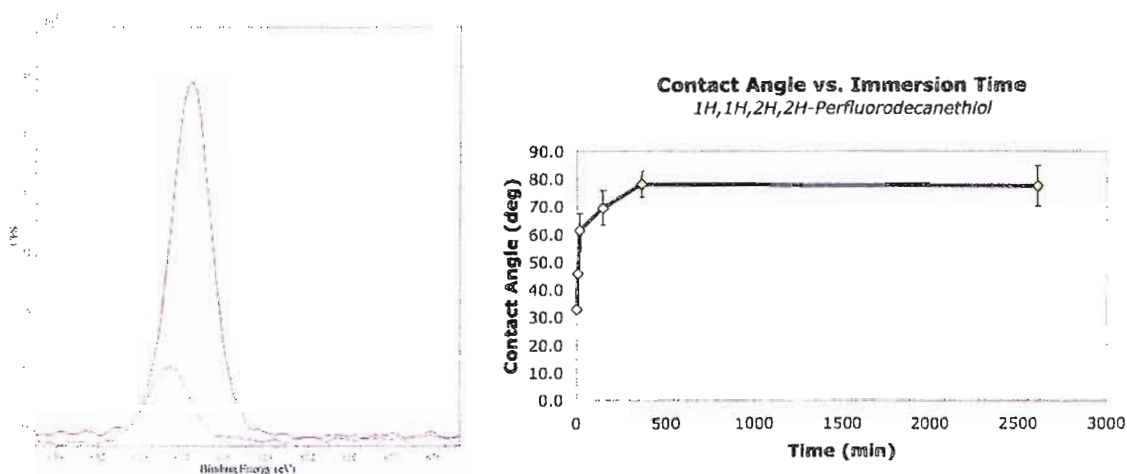
Figure 5.6. XPS F 1s region scan for chemically anchored gold nanoparticles immersed in a solution of *1H,1H,2H,2H*-perfluorodecanethiol for 5 min (red), 60 min (brown), and 24 hr (purple). The increase of F 1s signal with increased immersion time indicates the semi-perfluorinated alkanethiol has exchanged onto the nanoparticle surface. The water contact angle of the surface increases with longer immersion times.

Conclusions

In summary, we have used pre-functionalized nanoparticles to drive the assembly of surface-bound gold nanoparticle monolayers. We have demonstrated that thiol-thiol ligand exchange reactions can be used to introduce new surface functionality to pre-assembled monolayers of gold nanoparticles. Alkanethiols and other thiol ligands with variable terminal functionality exchange onto the exposed upper surfaces of the bound nanoparticles, while the thiol-phosphonic acid ligands anchoring the particles to the substrate remain in place. The average nanoparticle core diameter and density of gold cores per unit area do not change during the exchange reaction up to 24 hr, as determined by TEM. Etching of the gold cores may occur due to the extremely large excess of incoming thiols used in the exchange reactions, and we propose that this etching leaves chemically modified, asymmetric nanoparticles bound to the substrate. We are currently

investigating the versatility of this approach with a library of organic- and water-soluble incoming thiol ligands, the structure of the etched, surface-bound particles following exchange reactions, and whether this approach can be used to generate small ($d_{core} < 2$ nm) Janus nanoparticles.

Bridge

Having demonstrated that known thiol exchange chemistry for planar gold substrates and gold nanoparticles can be extended to two-dimensional nanoparticle assemblies, we wanted to assess the utility of other gold surface treatments in modification of gold nanoparticle films. Chapter VI describes our experiments utilizing UV/ozone treatment as a method of stripping the ligand shells from chemically anchored gold nanoparticle monolayers. Rather than functionalizing the gold cores, as in Chapter V, this method exposes the bare gold cores for interaction with the surrounding environment. We demonstrate this concept by producing gold nanoparticle catalysts on iron oxide using mild self-assembly conditions and convenient UV/ozone treatment to activate the particles toward low-temperature catalysis of $CO_{(g)}$ to $CO_{2(g)}$.

CHAPTER VI

UV/OZONE-MEDIATED STRIPPING OF ORGANIC THIOL LIGAND SHELLS

FROM SURFACE-BOUND GOLD NANOPARTICLE MONOLAYERS

Note: Portions of Chapter VI are expected to appear in an upcoming communication, co-authored by Jespersen, M. L. and Hutchison, J. E. The first author designed experiments and carried out all of the laboratory work described herein. The author also composed the manuscript corresponding to Chapter VI. J. E. Hutchison provided experimental and editorial guidance. All materials syntheses and the majority of subsequent characterization were carried out at the University of Oregon, with some analysis performed at the Surface Characterization and Nanofabrication Laboratory at the University of Utah.

Introduction

In contrast to the non-reactive behavior of gold in the bulk state, nanoscale gold supported on certain metal oxides has been shown to readily catalyze a number of transformations. Haruta and coworkers first demonstrated the low-temperature catalytic conversion of $CO_{(g)}$ to $CO_{2(g)}$ using nanoparticulate gold coprecipitated on several metal oxide supports.[1-3] Gold nanoparticles have since been shown to catalyze many reactions of technological and industrial significance, including oxidation of primary alcohols to aldehydes,[4] epoxidation of propene,[5,6] hydrogenation of CO and CO_2,[7] chemoselective hydrogenation of nitro compounds,[8] and the reduction of nitrogen oxides,[9,10] among

many others.[11-13] The vast potential of supported gold nanoparticles in heterogeneous catalysis has spawned a vigorous research effort into the origin of this catalytic activity and the preparation of supported gold catalysts.

A number of parameters have been investigated in attempts to elucidate the mechanisms underlying the enhanced catalytic activity of nanoscale gold. In particular, this activity has been shown to depend on the composition and structure of the metal oxide support,[2,14] the particle-support contact interface,[15] gold oxidation state,[16] and particle size and shape. The catalytic activity of gold nanoparticles strongly depends on particle size,[17-20] with peak activity observed for particles in the 2-4 nm size range, which exhibit nonmetallic electronic properties.[21] These size effects make the incorporation of small gold nanoparticles approximately 3 nm in diameter (or smaller) highly desirable targets in the design of supported gold nanoparticle catalysts.

There are several challenges to controlling the key structural attributes of supported gold catalysts, including the size of the gold nanoparticles, the catalyst loading, and establishment of contact between the support material and the particles. Common preparative methods for supported gold nanoparticle catalysts enable formation of the particle-support interface and a limited degree of control over catalyst loading. These methods include coprecipitation, which involves simultaneous precipitation of metal hydroxides or carbonates with Au precursors, and deposition-precipitation techniques, which generally involve formation of gold hydroxide in solution, followed by addition of the metal oxide support. Both approaches require calcination at elevated temperatures, which causes sintering of the supported particles. Sintering during catalyst preparation or

during use at elevated temperatures presents a large obstacle to the widespread incorporation of these materials in heterogeneous catalysis applications because gold nanoparticles larger than 8 nm in diameter do not appear to be catalytically active. In addition to nanoparticle growth by sintering,[22] the disadvantages of these high-temperature preparations include significant colloid polydispersity due to deposition of large Au precipitate crystals onto the metal oxide support[14] and incompatibility with a number of other support materials (e.g., carbon).[23]

In order to minimize sintering and polydispersity issues, some groups have investigated deposition of pre-synthesized gold nanoparticles, rather than coprecipitated gold, onto metal oxide supports. This approach offers the advantages that small, relatively monodisperse colloids can be used, and the interparticle spacing or catalyst loading can be controlled through the use of protecting ligands, usually in the form of thiolates.[24] One drawback of this approach is that in order to access the catalytic activity of these particles, the ligands must be removed post-deposition. Although thermal treatments effectively remove the protective ligand shell, they also induce nanoparticle aggregation, resulting in larger core diameters and increases in polydispersity. Because gold nanoparticles deposited on metal oxide supports by this method are still subject to sintering, and because it is difficult to control the catalyst loading and homogeneity by current catalyst preparative methods, a strategy for the low temperature removal of the protecting ligands should prove advantageous because thermal treatment would be unnecessary.

We propose the self-assembly of functionalized gold nanoparticles onto metal oxide supports as a strategy to overcome the disadvantages of current gold catalyst preparation methods. This approach utilizes mild self-assembly conditions, followed by ligand removal from the chemically anchored nanoparticles at low temperatures using UV-generated ozone (UV/O$_3$). Stripping of thiol ligands should expose bare gold cores, thus providing access to the catalytically active gold nanoparticle surface. In addition, interparticle spacing could potentially be manipulated by the ligand shell thickness, enabling control over the catalyst loading. Furthermore, it has been proposed that if supported gold nanoparticles can be confined to their own "sticky islands" to inhibit aggregation, this would represent a tremendous step forward in nanoparticle-based heterogeneous catalysis.[25] If the ligand shell can be partially removed, it is likely that residual surface-bound linker ligands will discourage nanoparticle aggregation.

Our strategy calls for the convenient removal of thiol ligand shells from gold nanoparticles at ambient temperatures using UV-generated ozone. UV/ozone treatment is an effective means for removal of adventitious organic contamination from planar gold substrates.[26, 27] In addition to removal of physisorbed contaminants, this strategy has been employed to remove self-assembled monolayers of alkanethiols from planar gold surfaces[26] and in the photopatterning of alkanethiol monolayers on gold.[28, 29] The effectiveness of UV/O$_3$ treatment in thiol monolayer removal from gold is due to oxidative conversion of chemisorbed alkylthiolates to physisorbed alkylsulfonates, which can be easily rinsed from the substrate with water or ethyl alcohol.[26, 30] Gaseous ozone treatment has been utilized as a method of ligand stripping in gold nanoparticle catalysts

supported on TiO_2.[31] While ozone treatment and ligand stripping did cause an increase in nanoparticle size in these catalysts, ligand removal by ozone results in gold particles that are appreciably more stable to subsequent thermal treatment than non-treated samples. These catalysts were then calcined at 400 °C but did not aggregate during thermal treatment after exposure to ozone. To date, such an approach has not yet been applied to monolayers of chemically anchored gold nanoparticles formed by directed self-assembly.

A potential concern is that nanoparticle aggregation occurs in many supported gold catalysts after prolonged use even at low temperatures because the particles are not chemically bound to the support. We address this concern by utilizing self-assembled films of surface-bound gold nanoparticles. Monolayers of alkylphosphonates are a well-known class of organic thin films that readily assemble onto a range of metal oxide surfaces,[32, 33] including iron oxide.[34] In addition, gold nanoparticles passivated with a thiol ligand shell containing terminal phosphonic acid functionality have been assembled onto patterned hafnium(IV) oxide on silicon dioxide.[35, 36] If gold nanoparticles can be chemically-bound to an underlying metal oxide support through the stabilizing ligand shell, it is possible that partial removal of the ligands by ozone treatment could leave gold nanoparticles tethered to the metal oxide support through residual thiol linker, while bare gold cores could be exposed for interaction with the gaseous environment and the underlying support material. Such an approach based on surface-bound nanoparticle monolayers would enable convenient, low-temperature activation of supported gold catalysts while inhibiting the mobility of nanoparticles that causes particle growth and diminished catalytic activity.

Here we report the production of catalytically active gold nanoparticles on metal oxide supports through mild self-assembly conditions followed by UV/O_3 treatment. The UV/O_3 treatment almost completely removes the ligand shell, exposing the catalytically active bare gold surface to the gaseous environment. A fraction of the thiol-phosphonate ligand shell remains after this treatment, so nanoparticle aggregation is limited despite their exposed gold cores. Functionalized gold nanoparticles are assembled onto iron oxide powders, and their ligand shells are removed by convenient UV/O_3 treatment. We demonstrate that the bare gold nanoparticles obtained through this strategy participate in the catalytic conversion of $CO_{(g)}$ to $CO_{2(g)}$ at room temperature.

Experimental

Materials. Iron nitrate nonahydrate [$Fe(NO_3)_3 \cdot 9H_2O$] was obtained from Mallinkrodt. Hydrogen tetrachloroaurate trihydrate ($HAuCl_4 \cdot 3H_2O$, 99+%) was acquired from Strem. 2-Mercaptoethylphosphonic acid [$HS(CH_2)_2P(O)(OH)_2$] was synthesized as previously reported.[35] Deionized water (18.2 $M\Omega$-cm) was purified with a Barnstead Nanopure Diamond system. Dichloromethane was distilled from calcium hydride.

Nanoparticle Synthesis and Functionalization. Gold nanoparticles (d_{core} = 1.5 $\pm$ 0.5 nm) were synthesized first as triphenylphosphine-stabilized precursors according to a previously described synthesis.[37] Ligand exchange was carried out in a biphasic system, starting with 203 mg (~7.9 μmol) of the as-prepared gold nanoparticles in 80 mL dichloromethane and 117 mg (0.82 mmol, 114 molar equivalents) 2-mercapto-ethylphosphonic acid in 100 mL H_2O, buffered to pH $\approx$ 8. The biphasic solution was

stirred for 24 hours until the organic fraction was clear and no insoluble material was observed as a foamy interphase, indicating completion of the exchange reaction. The aqueous and organic fractions were separated, and the aqueous fraction was washed with dichloromethane (3 x 50 mL). Residual dichloromethane was removed by rotary evaporation. In order to remove excess free ligand, the water-soluble nanoparticles were purified by a diafiltration process[38] using a 10 kD diafiltration capsule (Pall Life Sciences), concentrating the particle solution to 30 mL and then filtering with 50 volume equivalents (~1.5 L) of deionized water. The purified aqueous nanoparticle solution was concentrated to 20 mL and lyophilized overnight.

Preparation of Planar Substrates. The Si substrates used in this study were cut from n-type <100> wafers with 10-20 Ω-cm resistivity and a 3 μm thermal oxide (Wafer World). Silicon dioxide TEM grids were prepared as previously reported.[39] The SiO_2 surfaces of the grids were cleaned in a solution of dilute SC-1 (dSC-1, 100:4:1 H_2O: 30% H_2O_2: 30% NH_4OH) at 70 °C for 15 min. Substrates were then rinsed with copious amounts of deionized water and dried under a stream of argon prior to further surface treatment. SiO_2 surfaces were activated using an oxygen plasma treatment (150W, 200 mT, 20 sec), followed by immediate immersion in deionized water.[36] Plasma treatments were carried out using a March Plasma Systems CS-1701 reactive ion etcher. Following this plasma treatment, the substrates were again treated in dSC-1 at 70 °C for 15 min to remove adventitious carbon contamination and inorganic particulates, as well as to chemically generate surface silanol functionality.[36] The substrates were then rinsed with deionized water and were transferred immediately to a 5 mM aqueous solution of $HfOCl_2$

for four hours at 45 °C. HfOCl$_2$ solutions were filtered through a cellulose acetate syringe filter with 0.2 μm pore size prior to any assembly chemistry in order to remove insoluble particles. Following the surface functionalization step, the substrates were rinsed with water and transferred to a solution of 2.5 mg nanoparticles per milliliter of 3:1 MeOH: H$_2$O for 24 hr at room temperature. Following nanoparticle assembly, the substrates were removed from solution, rinsed with copious amounts of deionized water, and dried under a stream of argon prior to analysis.

UV/ozone treatment of planar substrates was carried out in a stainless steel box supplied with laboratory air at room temperature. Substrates were placed face up in a Boekel Industries UV Clean 135500 UV/ozone cleaning system supplied with laboratory air and were exposed to ozone generated by UV light for three minutes. Following this treatment, substrates were rinsed with copious amounts of deionized water and dried with a stream of argon prior to any surface analysis.

Preparation of Iron Oxide-Supported Gold Catalysts. Iron oxide powder was prepared by precipitation of iron hydroxide, followed by calcination. Briefly, 6.36 g (60 mmol) sodium carbonate was dissolved in 300 mL water in a round-bottom flask equipped with a stir bar, and heated to 70 °C. To this solution was added 90 mL 0.11 M Fe(NO$_3$)$_3$. The mixture was stirred for 1 hr at 90 °C and then filtered to retain the dark orange precipitate, which was washed with deionized water (3 x 100 mL). The product was collected in a glass dish and heated at 130 °C for one hour in air. The mixture was then calcined at 400 °C in air for 4 hours to yield a dark red-orange powder. Gold nanoparticles with a stabilizing ligand shell of 2-MEPA were dissolved in water (24 mg

in 15 mL) and added to a 50 mL round-bottom flask. Fe_2O_3 powder (0.277 g) was added to the reaction flask, and the mixture was stirred overnight. The insoluble, dark orange product was collected by vacuum filtration and washed with deionized water (5 x 20 mL). The product was dried at 50 °C in air for approximately 2 hours, yielding self-assembled monolayers of functionalized gold nanoparticles supported on iron oxide. Nanoparticle ligand shells were removed by exposure of the dried powder to UV-generated ozone in a Boekel Industries UV-ozone cleaning system for three min. The product was transferred into a fritted funnel and rinsed with deionized water (3 x 20 mL) to remove physisorbed alkylsulfonates. The product was again dried in air at 50 °C overnight, yielding ligand-stripped gold nanoparticles supported on iron oxide.

Analysis Techniques. X-ray photoelectron spectroscopy measurements were conducted using a Kratos AXIS Ultra Electron Spectrometer (Kratos Analytical, Chestnut Ridge, NY) with a monochromated Al Kα x-ray source operated at an accelerating voltage of 15 kV and an emission current of 15 mA. TEM images were acquired using a Phillips CM-12 microscope operated at 120 kV accelerating voltage.

Infrared spectra were acquired using a Thermo-Nicolet Magna IR Spectrometer. Carbon monoxide (4%) in air was obtained from AirGas. A 5-mL IR gas cell with KBr windows (New Era Enterprises, Inc.) was fitted with rubber septa at the inlet and outlet ports. This configuration was leak tested by filling the cell with 4% CO gas mixture and collecting IR spectra at various times over a 48-hour period, with no observable change in the IR spectra even after 48 hours. For qualitative measurements of catalytic conversion of CO to CO_2, a glass tube was packed with 150 mg of the test material, with

glass wool on either side. This glass tube was inserted into the gas line so any gas mixture entering the cell was passed once through the catalyst plug. The CO gas mixture was introduced to the cell at a flow rate of approximately 2 cm^3 sec^{-1} for 45 seconds to ensure complete purging of the cell. The infrared spectrum of the enclosed gas was then collected. In cases where CO_2 gas was observed, the cell was allowed to sit in a nitrogen atmosphere for up to 24 hours before the spectrum was collected again to ensure that any observed CO_2 could not be attributed to air leaking into the cell. In all cases, the initial and final IR spectra were identical, indicating no CO_2 was leaking into or out of the cell, and all CO_2 observed was the result of catalytic conversion of CO.

Results & Discussion

Our surface modification strategy is to assemble surface-bound gold nanoparticle monolayers and then partially remove the protective ligand shell by UV/ozone treatment. We suspect that the bound alkylthiolates are oxidized to alkylsulfonates by this approach and that these sulfonates can be easily removed from the film by simply rinsing the substrates in water to yield gold cores that are exposed to the surrounding environment and anchored to the surface through residual thiol-phosphonate linkers (Scheme 6.1). We investigate the extent of ligand removal from the film by XPS composition analysis. One concern is that the nanoparticles could be completely desorbed from the film if all thiolate ligands are oxidized, resulting in aggregation or rinsing of the nanoparticles from
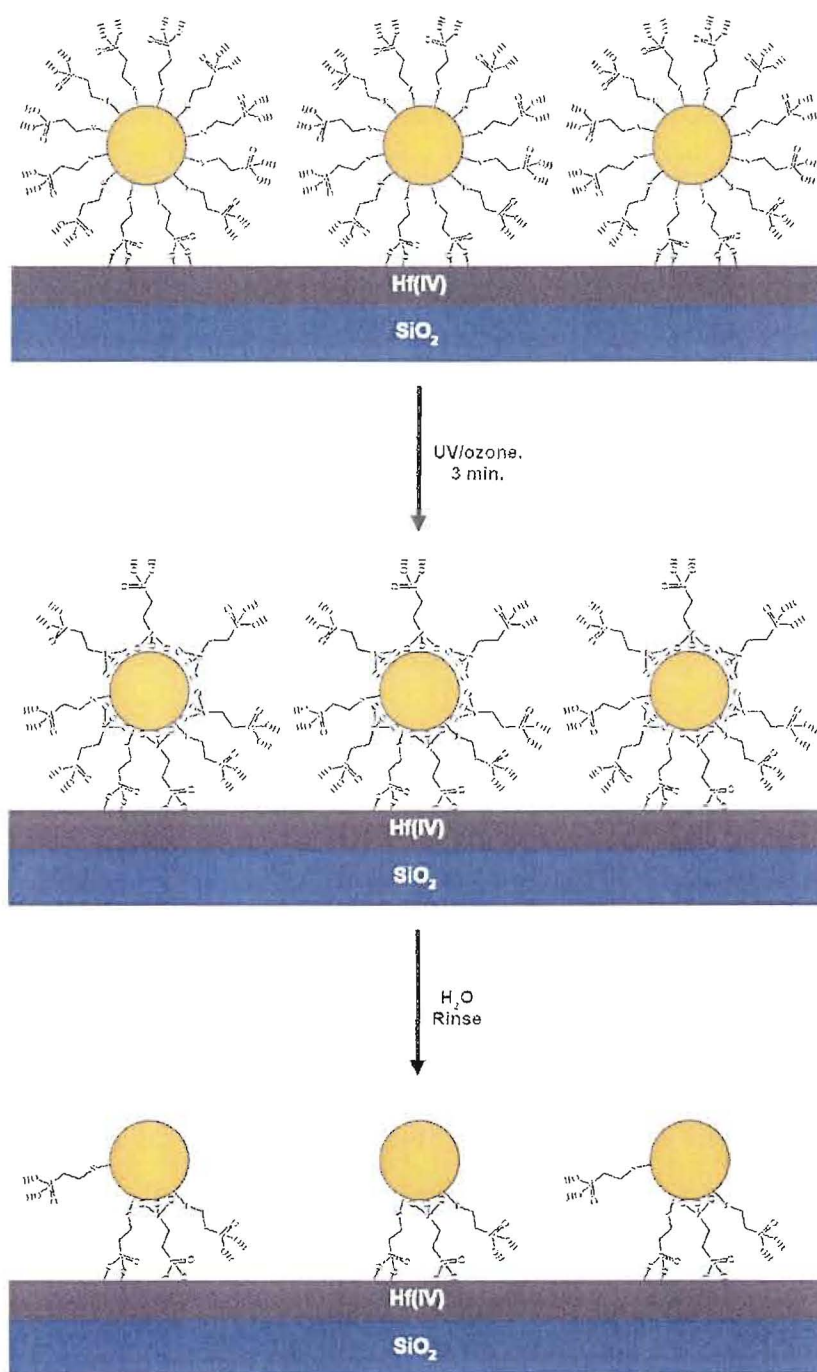
Scheme 6.1. Schematic illustration of UV/ozone-mediated ligand stripping on surface-bound gold nanoparticles. The UV/ozone treatment oxidizes the majority of bound thiolates to sulfonates, which can be easily rinsed from the film with water to yield bare gold cores exposed to the surrounding environment and still anchored to the underlying substrate.

the substrate. We examine the nanoparticle layers by TEM to assess the structural effects of UV/ozone treatment and show that the nanoparticles undergo limited aggregation but likely remain anchored to the substrate through residual ligands. Because the nanoparticle core sizes after ligand removal are in the ideal size range for gold nanoparticle catalysts, we demonstrate the utility of this surface treatment by stripping the ligands from pre-assembled gold nanoparticle films on iron oxide, thus activating the nanoparticles for catalytic conversion of CO to CO_2 at room temperature.

XPS Analysis of Model Planar Substrates. UV/ozone treatment was investigated as a ligand stripping method to produce catalytically active gold nanoparticles on metal oxide supports. In order to understand the changes in nanoparticle film composition in response to treatment with UV/O_3, we examined UV/O_3-treated monolayers of gold nanoparticles by x-ray photoelectron spectroscopic analysis. Although we intended to use gold nanoparticles assembled onto metal oxide powders as catalytic materials, XPS analysis of powder samples generally suffers from low count rates of emitted photoelectrons due to scattering caused by the rough surface topography. Poor signal-to-noise ratio, sample-dependent variation of differential surface charging, and the low sensitivity of phosphorus and sulfur in the XPS experiment suggested the use of planar substrates could yield more useful data than powder samples for these analyses. To this end, we utilized self-assembled monolayers of functionalized gold nanoparticles on hafnium-modified SiO_2 as a model substrate for XPS.

We have previously reported the formation of gold nanoparticle monolayers on modified silicon dioxide substrates by a directed self-assembly process.[35, 36] Using

assembled films of gold nanoparticles on hafnium-modified silicon dioxide, we examined

the composition of the nanoparticle film before and after treatment with UV-generated

ozone. Figure 6.1 shows XPS spectra from the S 2p region. Prior to UV/ozone treatment,

the S 2p signal from bound thiolates is clearly evident. After exposure to UV/O_3 for

three minutes, nearly all of the thiolates present are converted to sulfonates, evidenced by

the shift of the S 2p peak to higher binding energy (168 eV). After rinsing the substrate

in copious amounts of water to remove alkylsulfonates, a small amount of sulfonate

remains, and the S 2p peak from bound thiolates is not observed in the spectrum. The

relative atomic sensitivity of S 2p in the XPS experiment is very low, and the plasmon

loss peak from Si interferes with the S 2p signal. For these reasons, we suspect that a

small amount of thiolate ligand could remain in the film but that it is below the detection

limit of the instrument on this substrate.

Table 6.1 lists atomic concentrations of the nanoparticle films determined by

XPS. The S 2p signal from thiolates decreases to below the detection limit of the

instrument after UV/ozone treatment. The S 2p signal from sulfonates increases after

UV/ozone treatment and then diminishes almost entirely after rinsing of the

alkylsulfonates, as expected. The P 2p signal decreases in intensity, indicating that some

of the thiol-phosphonate is removed but that a small amount remains present in the film.

The majority of this residual phosphorus content is likely in the form of surface-bound

phosphonates. The carbon content of the film decreases after UV/ozone treatment, as

expected. The measured carbon content is higher after rinsing than after UV/ozone

treatment. This is unexpected, and we conclude that a significant portion of the carbon
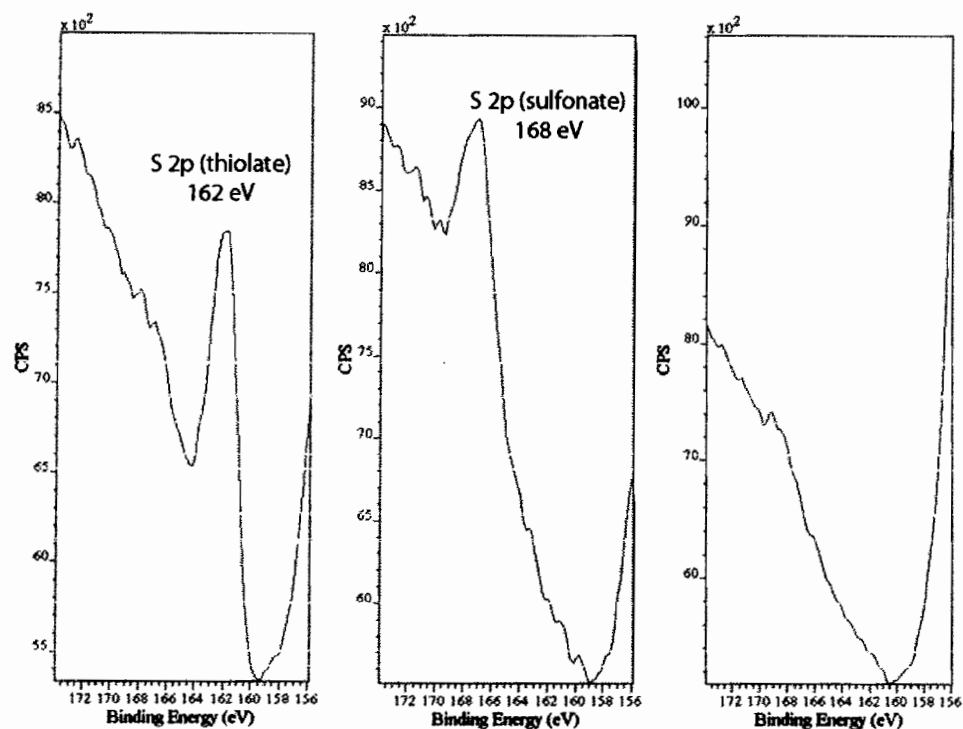
Figure 6.1. XPS spectra from the S 2p region showing bound thiolate prior to UV/ozone treatment (left), sulfonate following UV/ozone treatment (middle), and removal of sulfonates by rinsing (right).

content is adventitious in all three samples. The oxygen content increases following

oxidation of thiolates to sulfonates. We would also expect the Si and O concentrations to

increase after UV/ozone treatment and rinsing because the initial carbon-containing

overlayer probably attenuates the signals from both Si and O in the bulk SiO_2 substrate.

In addition, the atomic concentration of gold has decreased, but most of the gold content

of the film is retained. We suspected that this decrease in Au concentration resulted from

complete removal of the ligand shells from some of the nanoparticles, which were then

rinsed away with the physisorbed sulfonates. In order to determine the extent to which

Table 6.1. XPS atomic concentration data for UV/ozone-treated gold nanoparticle monolayers. All reported values are percent atomic concentrations ($\pm$ 0.1%).

Sample	Au (4f)	S (2p)	S (SO$_3$)	P (2p)	C (1s)	Hf (4d)	O (1s)	Si (2p)
No treatment	1.8	0.8	0	1.2	17.9	1.0	46.4	30.9
UV/O$_3$, 3 min.	1.0	0	0.7	1.3	9.3	1.0	54.5	32.1
UV/O$_3$ + rinse	1.0	0	0.1	0.6	11.6	0.9	53.1	33.3

the gold nanoparticles had been desorbed from the film, we conducted structural analysis of the nanoparticle monolayers using TEM.

TEM Analysis of UV/O$_3$-Treated Planar NP Films. Because XPS analysis of the UV/ozone-treated nanoparticle monolayers indicated removal of gold nanoparticles, we wanted to characterize the effects of UV/O$_3$ treatment on the nanoparticle film structure using TEM. Use of planar TEM substrates simplifies the structural characterization of the UV/O$_3$-treated nanoparticles because powder specimens exhibit very non-uniform electron transparency. To this end, we utilized self-assembled monolayers of gold nanoparticles on hafnium-modified SiO$_2$ TEM grids produced in our laboratory as model substrates for TEM analysis.

TEM images and particle size analysis before and after UV/O$_3$ treatment show that the average core size increases by a small amount after ozone exposure, from 1.5 $\pm$ 0.6 nm to 1.8 $\pm$ 1.0 nm (Fig. 6.2). In addition, the nanoparticle size distribution broadens. We suspect that some of the nanoparticles are able to migrate short distances on the surface because most of the ligands have been removed, although residual ligand is observed by XPS. This movement results in the aggregation of adjacent particles and could occur even if the ligand-stripped particles remain anchored to the substrate because
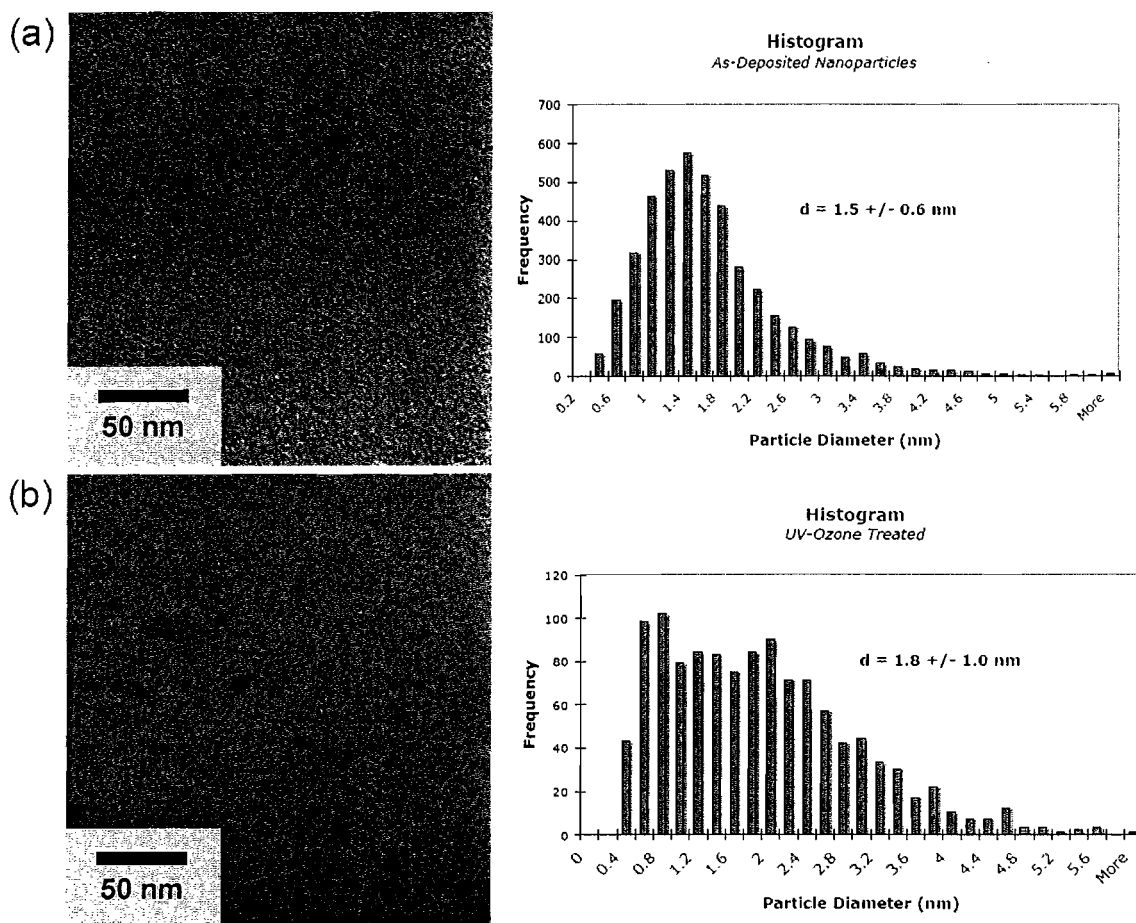
Figure 6.2. TEM images and nanoparticle size distributions from (a) assembled nanoparticles prior to UV/ozone treatment, and (b) the nanoparticle film after UV/ozone treatment and rinse step to remove akylsulfonates. The average core size increases following UV/ozone treatment, and some aggregates can be observed. The majority of the nanoparticles remain adsorbed to the surface, and the average core sizes in both cases fall into the ideal size range for oxide-supported gold nanoparticle catalysts.

the majority of the gold core is bare, and the initial interparticle distances afforded by the

2-MEPA ligand are short. By visual inspection, the nanoparticle layer has a greater

fraction of voids after UV/ozone treatment. Based on the average core sizes for either

sample and the model of a close-packed monolayer with an interparticle distance of twice

the ligand length, we calculate 67% of a complete monolayer for the as-deposited

particles, compared to 48% of a full monolayer for the UV/ozone treated sample.[†] While a fraction of the nanoparticles could have been rinsed from the substrate following complete ligand shell oxidation, it is important to note that the majority of the nanoparticles remain adsorbed on the surface, in agreement with our XPS analysis. In addition, these nanoparticle films are stable in water and air over several days without exhibiting further aggregation or desorption of nanoparticles. This suggests that some of the surface-bound ligand remains, limiting the mobility of the nanoparticles and preventing further aggregation. This is also consistent with our XPS data that shows the UV/ozone treated film retains some phosphorus content from the thiol-phosphonate ligand. It is likely the case that some of the remaining ligand resides randomly around the entire perimeter of the particle, but the majority of the gold surface is bare (Scheme 6.1), allowing the gold core to interact with its environment, the oxide support, and adjacent particles while still remaining surface-bound.

Based on our observation that the majority of the gold cores remain anchored to the surface after UV/O_3 treatment and the fact that the average core diameter remains in the ideal size range for oxide-supported gold nanoparticle catalysts, we hypothesized that this post-deposition modification strategy could serve as a convenient, low-temperature method for ligand removal in the preparation of oxide-supported gold nanoparticle catalysts. Although hafnium-modified SiO_2 serves as a useful model substrate for XPS

[†] Nanoparticle coverage calculations were based on a close-packed monolayer (ML) model, in which the interparticle distance was assumed to be twice the ligand length of 0.65 nm for a 2-MEPA ligand. Based on the average core diameter for the as-deposited particles, this gives 0.15 cores/nm^2. For the UV/ozone treated particles, this gives a maximum density of 0.12 cores/nm^2. Nanoparticles were counted within regions of known area in ImageJ to give 0.10 cores/nm^2 (67% ML) and 0.06 cores/nm^2 (48% ML) for the untreated and UV/O_3-treated samples, respectively.

composition analysis and TEM studies, this surface is not an ideal oxide support for catalysis because its surface area is extremely low. In addition, this type of hafnium-modified oxide support has not been studied in heterogenous catalysis involving gold nanoparticles. In order to determine whether or not UV/O_3 could be utilized to produce catalytically active gold nanoparticles, we employed iron oxide as the support material because Fe_2O_3/Au catalysts have shown excellent catalytic activity in other studies.[1,2]

IR Studies for Catalytic Conversion of CO to CO$_2$. Using iron oxide powders as support materials for self-assembled gold nanoparticles, we conducted gas phase IR studies to determine whether UV/O_3-mediated ligand stripping could expose bare gold cores for catalytic conversion of $CO_{(g)}$ to $CO_{2(g)}$ at room temperature. Functionalized gold nanoparticles (d_{core} = 1.5 ± 0.5 nm) stabilized by a 2-MEPA ligand shell were assembled onto iron oxide powders. Two control experiments were carried out in order to determine whether the bare iron oxide or the nanoparticle-coated iron oxide showed any catalytic activity prior to UV/O_3 treatment. A gas mixture of 4% CO in air was passed through a catalyst plug, consisting of a glass tube containing 150 mg of either test material, capped by glass wool on both ends. The product gas mixture was collected in an air-tight gas cell and analyzed by infrared spectroscopy (Fig. 6.3). No appreciable catalytic activity was observed for either material, as shown by the small amounts of CO_2 present in the gas mixture. This lack of activity was expected because iron oxide is not known to catalyze the room temperature oxidation of CO. In addition, the catalytically active gold nanoparticle surfaces in the iron oxide/gold nanoparticle hybrid material were passivated by the thiol ligand shell, blocking CO adsorption.
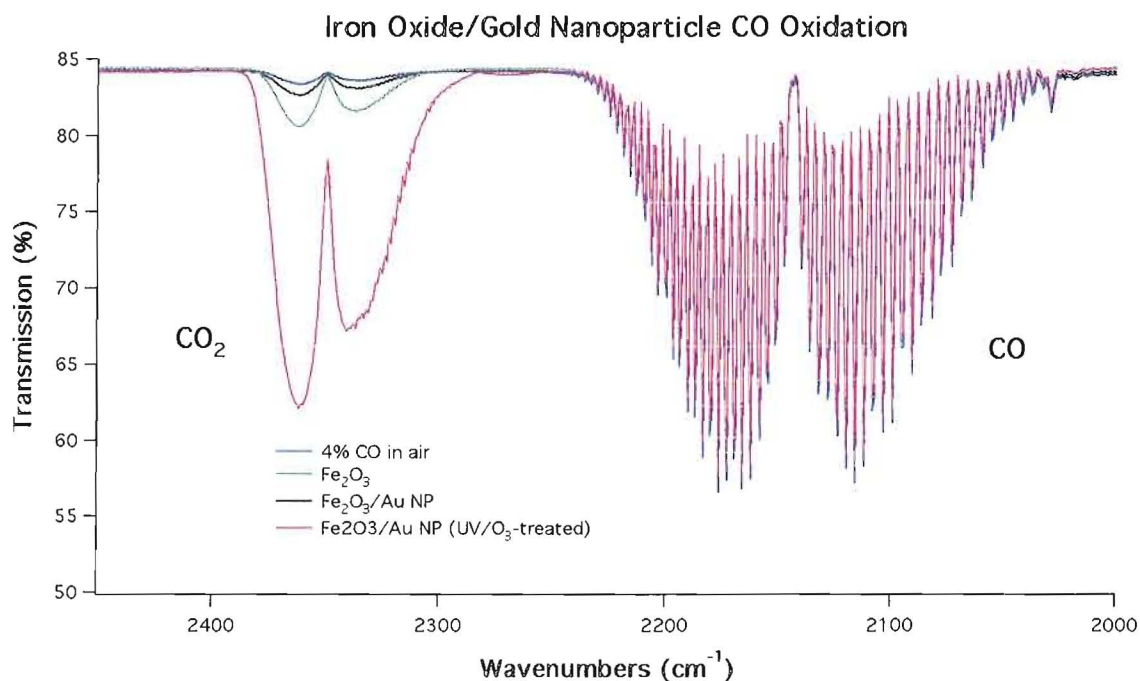
Figure 6.3. Infrared transmission spectra of 4% CO in air (blue) passed through a plug of UV/ozone-treated iron oxide powder (green), iron oxide powder with self-assembled gold nanoparticles (black), and UV/ozone-treated iron oxide/gold nanoparticle hybrid material (red). The UV/ozone-treated gold nanoparticles on iron oxide showed enhanced activity in conversion of CO to CO_2.

In order to assess the effectiveness of UV/ozone treatments for exposing the bare gold cores, the nanoparticle-loaded iron oxide powder was treated with UV-generated ozone for three minutes. After rinsing away any unbound sulfonates resulting from this treatment, the material was dried under vacuum. This UV/ozone-treated material showed considerably enhanced conversion of CO to CO_2 at room temperature (Fig. 6.3). Only after UV/ozone treatment did the oxide-supported nanoparticles show this enhanced catalytic activity. In addition, a 4% CO in air mixture allowed to sit in the sealed IR cell in the presence of excess catalyst showed continued conversion of CO to CO_2 over extended periods of time (Fig. 6.4). These experiments show that UV/ozone-mediated
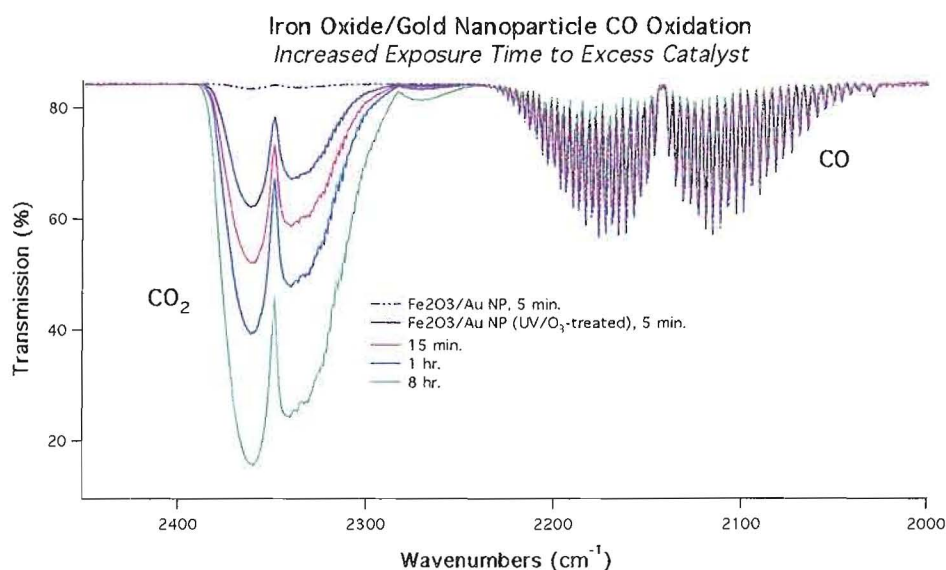
Figure 6.4. Infrared transmission spectra of 4% CO in air mixture exposed to excess UV/ozone-treated iron oxide/gold nanoparticle catalyst for 5 min (black), 15 min (red), 1 hr (blue), and 8 hr (green). For reference, an IR spectrum from the gas mixture exposed to untreated iron oxide/gold nanoparticle material is shown by the dashed line. Only the UV/ozone-treated material participates in the room temperature conversion of CO to CO_2 at room temperature, and the catalytic conversion continues over time until the signal from CO disappears almost entirely at longer reaction times.

ligand stripping is an effective strategy for exposing bare gold cores in self-assembled films of functionalized gold nanoparticles without the use of thermal treatments. Although the removal of ligand shells results in desorption of some of the assembled nanoparticles and a small amount of particle growth, the majority of the particles remain anchored to the surface, and their aggregation is limited. The nanoparticle films assembled on iron oxide and treated with UV/ozone participate in conversion of CO to CO_2. This convenient strategy for production of catalytically active gold nanoparticles on oxide supports should find use in many heterogeneous catalysis applications.

Conclusions

In summary, we have demonstrated a process for generating active nanoparticle catalysts on metal oxide supports by mild self-assembly conditions and UV/ozone-mediated stripping of protecting thiol ligands. Composition analysis reveals the conversion of bound thiolate ligands to physisorbed sulfonates, which can be easily rinsed from the film to expose bare gold cores. Due to the partial removal of the ligand shell, the majority of the nanoparticles remain bound to the substrate through the ligand terminal functionality. Ligand stripping results in a small increase in the average nanoparticle core size, broadening of the size distribution, and limited aggregation, as observed by TEM, but the average core size following UV/O_3 treatment is well-suited for accessing the enhanced catalytic activity of oxide-supported gold nanoparticles. Utilizing this surface modification strategy, we have shown that self-assembled monolayers of gold nanoparticles can be activated to participate in the catalytic conversion of CO to CO_2 at room temperature by rapid treatment with UV-generated ozone. We are currently examining in greater detail the nature of the nanoparticle-support interaction, the turnover frequencies of these catalytic materials, and the effects of nanoparticle structural parameters (ligand shell length, core size, etc.) on the loading levels of gold nanoparticles in these catalysts.

CHAPTER VII

CONCLUDING SUMMARY

In this dissertation, we have developed new surface chemistry on gold and demonstrated the use of designed interfacial interactions in nanoparticle monolayers to access the unique size-dependent properties of these materials. We have shown that ligand-substrate interactions enable the formation of extended surface-bound gold nanoparticle monolayers that support electron transport, as well as guide the precise placement of nanoparticles that catalyze nanowire growth on patterned substrates. In addition, the interactions of these nanoparticle films with the environment can be manipulated through thiol ligand exchange reactions or UV-ozone treatment to access uniquely functionalized nanoparticles and unlock the catalytic properties of gold nanoparticles on metal oxide supports.

While self-assembled monolayers of thiols on gold and organic acids on metal oxides have been well-studied, there still exists a need for new surface chemistries that are complementary to established systems in order to meet the demand for advanced functional materials requiring increasingly sophisticated self-assembly schemes. In Chapter II, we described a new class of monolayers based on modification of gold surfaces with hafnium ions. Monolayers of alkanephosphonic acids assembled on

hafnium-modified gold are readily obtained, patternable, well-ordered, and resistant to displacement by thiols. We demonstrated the compatibility of this new surface chemistry with well-known gold-thiol assembly strategies. This was accomplished through the formation of novel surface structures utilizing a bifunctional (thiol-phosphonic acid) molecule to simultaneously form a patterned phosphonic acid monolayer on hafnium-modified gold and a thiol monolayer on the bare gold. The success of this approach demonstrates that there are numerous new surface modification chemistries yet to be developed that should enable a range of novel and complex self-assembly schemes. Some exciting applications that should be explored for hafnium-phosphonate-modified gold include its use as a diffusion barrier for domains of thiol monolayers, its use as an etch resist for fabrication of nanoscale metal contacts and interconnects, as well as the development of test structures for electron tunneling experiments on conductive substrates in molecular electronics applications.

We next turned our attention toward the development of surface chemistries that allow control over the interfacial assembly properties of gold nanoparticles. In Chapter III, we described a surface modification strategy based on a combination of oxygen plasma and wet chemical treatments that restores the surface composition of thermal SiO_2 to that observed on the native oxide. This proved to be an easy method for improving reactivity of thermal silicon dioxide and perhaps a general route to the activation of otherwise non-reactive, insulating oxide substrates. We demonstrated the utility of this strategy by employing the subsequent increase in surface reactivity toward hafnium ions in solution to direct self-assembly of extended, high-density monolayers of gold

nanoparticles functionalized with thiol ligands containing terminal phosphonic acids. These nanoparticle monolayers are dense and extended enough to support electron transport across a 5-µm electrode gap. This was also an opportunity to showcase new thermal SiO_2 TEM substrates developed by Greg Kearns, which allow TEM to be used as a surface analysis technique, complementary to surface composition analysis methods such as XPS. Our surface modification strategy could be easily integrated into current semiconductor processing technologies, serving as an example of using selective surface chemistry to transition from traditional semiconductor device fabrication to the bottom-up assembly of nanoscale devices with nanoparticles as their active components.

In addition to the formation of nanoparticle films that have interesting electronic properties, we proposed that the design of specific ligand-substrate interactions could be used to pattern gold nanoparticles for the selective generation of other nanomaterials. We explored this unique application in Chapter IV. Using the directed self-assembly of phosphonic acid-functionalized gold nanoparticles onto patterned zinc oxide on SiO_2, we demonstrated the selective growth of high crystal quality, vertically-aligned zinc oxide nanowire arrays by the vapor-liquid-solid growth method. Careful design of the interaction between the nanoparticle ligand shell and the substrate can lead to environmentally-benign nanofabrication, and we estimate that the synthesis of nanowires using self-assembled gold nanoparticles as the growth catalyst reduces the amount of gold waste by 16,000 times when compared to deposition of the gold catalyst by evaporative methods. In addition, the use of chemically-anchored nanoparticles as the growth catalyst may facilitate fine control over certain properties (spacing, diameter, etc.)

of the nanowire arrays through judicious selection of nanoparticle core size, shape, and ligand shell thickness, avenues which should be explored in detail as an extension of this work.

The remainder of the research described within this dissertation focused on post-deposition modification of self-assembled nanoparticle monolayers. This aspect of engineering nanoparticle interfaces has not been studied as extensively as particle-substrate interactions. In many ways, the surface-bound nanoparticle assemblies explored in our work are optimal for further modification to manipulate particle-environment interactions. The chemically-bound nanoparticle films are stable, unlikely to desorb under further treatment when compared to physisorbed nanoparticle arrays, and are likely resistant to a range of chemical environments.

Thiol-thiol ligand exchange reactions on surface-bound nanoparticle monolayers were studied as a first example of post-deposition modification, described in Chapter V. Ligand exchange reactions influence the surface energies of nanoparticle films, as evidenced by changes in their water contact angles, measured by contact angle goniometry. The nanoparticles are stable to the exchange process, as both average particle core size and the number of cores per unit area are preserved. This approach should be compatible with current lithographic patterning techniques and could permit formation of thiol monolayer domains that, due to the discrete nature of the individual gold particles, cannot interdiffuse. Since this surface chemistry generates topochemically functionalized nanoparticles bound to an underlying support, a next logical extension of this work should be to develop a high-yield method for releasing the particles from the

substrate, in order to isolate and characterize 1-2 nm Janus nanoparticles. One way to accomplish this might be to use high surface area silica as the substrate, which can later be removed by selective etching.

In addition to employing ligand exchange reactions to modify the ligand shells of surface-bound nanoparticles, in Chapter VI we investigated the use of UV/ozone treatment to partially remove the ligand shells from chemically anchored gold nanoparticles. This treatment exposes the gold core for direct interaction with its environment. Gold nanoparticles exposed to UV-generated ozone lose a portion of the stabilizing ligand shell, and the majority of the nanoparticles remain anchored to the oxide support. The utility of this approach was demonstrated by self-assembly of phosphonic acid-functionalized gold nanoparticles onto iron oxide powders, ligand removal by UV-ozone treatment, and the subsequent activity of those gold nanoparticles in the catalytic conversion of $CO_{(g)}$ to $CO_{2(g)}$ at room temperature. It should be helpful to design a controllable method of ozone delivery in order to more precisely tune the extent of ligand removal by this approach. In addition, mass spectrometry studies should be carried out to determine catalyst turnover frequencies and the lifetimes of these catalyst materials.

There remains a great deal of work to be done in order to effectively manipulate the interfacial properties of nanoparticles and nanomaterials in general. One could envision seemingly countless self-assembly schemes taking advantage of a wide range of known surface chemistries to access the properties of nanomaterials in interesting and important applications. Here, we have only examined the manipulation of gold

nanoparticles in the 1-2 nm regime as a model system. The nanoparticle monolayers

formed by our approach lack long-range order, and if self-assembly conditions can be

tuned to induce greater long-range crystalline order in this system, it should be possible

to exercise control over the electronic properties of these films, achieve more finely

controlled dimensions of high-quality nanostructures generated from colloidal gold

catalysts, design sensors based on two-dimensional nanoparticle assemblies, and

precisely tune gold catalyst loading on metal oxide supports.

APPENDIX A

SUPPORTING INFORMATION FOR CHAPTER II:

ALKANEPHOSPHONATES ON HAFNIUM-MODIFIED GOLD:

A NEW CLASS OF SELF-ASSEMBLED ORGANIC MONOLAYERS

Introduction

The following sections describe the initial experiments that suggested hafnium

could bind to gold surfaces. Based on our initial observations using contact angle

goniometry, we characterized octadecylphosphonic acid monolayers on hafnium-

modified gold that were dense and well-ordered enough to resist displacement by thiols.

In addition, another set of experiments is described in which we attempted to elucidate

the nature of the hafnium-gold interaction based on TOF-SIMS imaging. Based on the

presence of $Hf-O_x-Au$ fragments and the absence of Hf-Au and Hf-Cl fragments, we

suggest that the hafnium(IV) species interacts with a partially oxidized gold surface and

not through a chloride bridging species, nor directly with gold itself.

Experimental

Materials. Hafnium dichloride oxide octahydrate (Alfa Aesar; 99.998%), n-octadecylphosphonic acid [$CH_3(CH_2)_{17}P(O)(OH)_2$] (Alfa Aesar), and allyl mercaptan (Avocado Research Chemicals, Ltd.; 70%) were used as received. Shipley 1818 Photoresist (Shipley Company, Marlborough, MA), and Microposit 351 Developer (Shipley Company) were used as received. Deionized water (18.2 MΩ-cm) was purified with a Barnstead Nanopure Diamond system. Absolute ethyl alcohol (Aaper Alcohol and Chemical Company) was sparged with nitrogen for approximately 20 minutes prior to use.

Preparation of Substrates. Glass microscope slides used in this study were cleaned in a piranha solution (7:3 conc. H_2SO_4: 30% H_2O_2) for 15 minutes, rinsed with copious amounts of deionized water, and dried under a stream of argon prior to any assembly chemistry. Gold substrates on glass were prepared by evaporating 10 nm of chromium to promote adhesion of the gold layer, followed by 100 nm of gold. Monolayers of n-octadecylphosphonic acid (ODPA) on hafnium-modified gold and glass were prepared by soaking gold-coated glass slides in a 5 mM aqueous solution of $HfOCl_2$ for 3 days at 50°C. Upon removal from this solution, the substrates were rinsed with deionized water, dried under a stream of argon, and soaked in a 1 mM ethanolic solution of ODPA for 24 hours. Modification of the gold surface with allyl mercaptan was accomplished by soaking gold substrates on glass in a 1 mM ethanolic solution of allyl mercaptan for 24 hours.

Preparation of Patterned Substrates. The Si substrates used in this study were cut from n-type <100> wafers with 10-20 Ω-cm resistivity (University Wafer, Boston, MA). The Si substrates were cleaned in a piranha solution (7:3 conc. H_2SO_4: 30% H_2O_2) for 15 minutes, rinsed with copious amounts of deionized water, and dried under a stream of argon prior to any assembly chemistry. Gold-coated Si surfaces were prepared by evaporating 10 nm of chromium to promote adhesion of the gold layer, followed by 100 nm of gold. The gold-coated substrates were exposed to ozone for 10 minutes in a UV/ozone cleaner supplied with laboratory air at room temperature prior to further modification.

Photolithographic patterning of the Si substrates was achieved using Shipley 1818 Photoresist. The resist was applied using a dropper and spin-coated onto each gold-coated wafer at a speed of 3,000 rpm for 60 seconds. Solvent was driven off by heating the wafer on an aluminum block at 110 °C for 60 seconds. The substrate was then placed under a pre-fabricated emulsion mask using an OAI Model 200 Contact Mask Aligner and exposed to UV light for 11 seconds (125 W/cm^2). The photoresist patterns were developed by agitating in a mixture of 3.5:1 deionized water: Microposit 351 Developer for 60 seconds. The substrates were rinsed again in deionized water and dried under a stream of nitrogen. The patterned substrates were heated at 120 °C for 1 hour to improve the adhesion of the photoresist to the substrate. Any photoresist residue remaining within the exposed gold regions was removed by an oxygen plasma treatment (300 W, 5 seconds, 400 mT). Following the oxygen plasma treatment, the substrates were rinsed with deionized water and immediately transferred to a 5 mM aqueous solution of HfOCl$_2$

at 50 ˚C for three days. The substrates were then sonicated in water for five minutes to remove any physisorbed material, rinsed with water, and dried with a stream of argon. Photoresist was removed by sonicating the substrates in acetone, followed by a short oxygen plasma treatment as described above.

Results & Discussion

Initial XPS Studies of Hf/ODPA on Gold. We initially investigated the use of hafnium/alkanephosphonate chemistry to generate a hydrophobic surface between the fingers of interdigitated gold electrode arrays on a silicon dioxide substrate. We first modified the silicon dioxide portion of the substate with hafnium (IV), expecting to selectively attach n-octadecylphosphonic acid (ODPA) to the hafnium-modified regions. By then selectively modifying the patterned gold surface with allyl mercaptan, we expected to generate a uniformly hydrophobic surface. However, after treatment with hafnium-ODPA and prior to treating the substrate with allyl mercaptan, we found a uniformly hydrophobic surface, even on the gold portion of the substrate, where we anticipated the surface would maintain its relative hydrophilicity. Subsequent x-ray photoelectron spectroscopic analysis of the substrates showed the presence of hafnium and phosphorus on both the silicon dioxide and gold regions; no sulfur was detected on either surface (Figure A.1(a)). When the order of the surface modification steps was switched, with the allyl mercaptan soak preceding the hafnium/ODPA treatment, sulfur was found only on the gold surface, while hafnium and phosphorus were observed exclusively on the glass surface (Figure A.1(b)). These data suggest that the

hafnium/ODPA binds to both the glass and gold surfaces and prevents subsequent

binding of the allyl mercaptan to the gold.
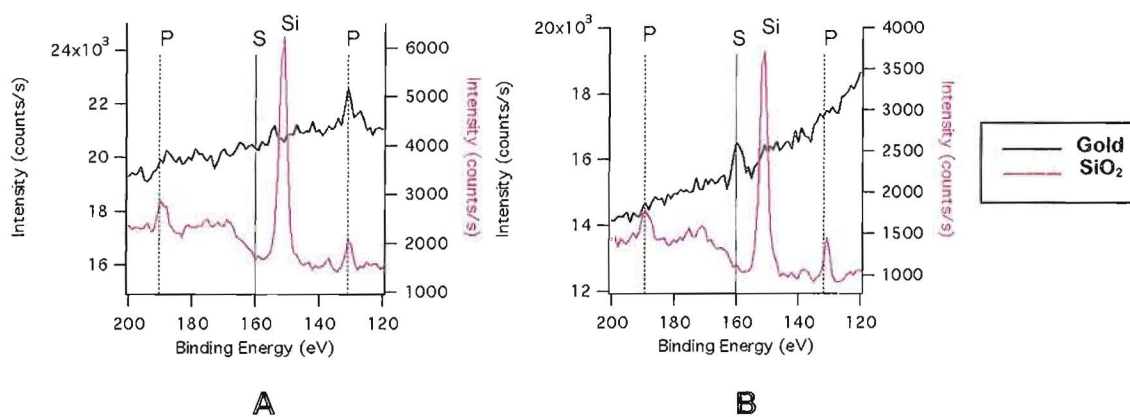
Figure A.1. XPS spectra for gold-patterned glass surfaces treated with (a) hafnium/ODPA followed by allyl mercaptan or (b) allyl mercaptan followed by hafnium/ODPA. The black traces are the spectra for the gold surfaces and the red traces are for the glass surfaces. The data show that when the substrate is first treated with hafnium/ODPA, phosphorus is found on both gold and glass, indicating that the hafnium/ODPA has prevented the adsorption of allyl mercaptan to the surface. These spectra were collected at 20 eV pass energy with a monochromated Al Kα x-ray source.

TOF-SIMS Imaging of Patterned Substrates. After preparing the hafnium-patterned gold substrates, the surfaces were analyzed using TOF-SIMS in an attempt to identify mass fragments that would help to elucidate the nature of the interaction between the hafnium species and the underlying gold. The images in Figure A.2 below show the ion yields for the HfO, AuOHf, AuO_2Hf, AuO_3Hf, and AuHf fragments. The patterning of HfO on the gold surface is easily observed. The ion yields corresponding to AuO_xHf can be discerned from the background and closely match the Hf-patterned regions,

though the overall ion yields are quite low for those species. In contrast, AuHf fragments cannot be distinguished from the background, suggesting this species is not present. This seems to indicate that the hafnium species on the surface interacts with gold through an oxygen bridge and does not interact directly with gold itself.
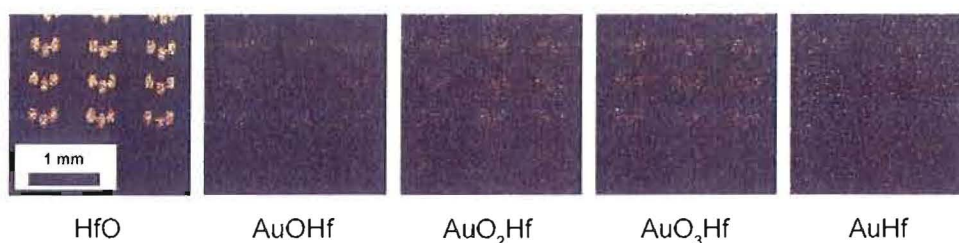
Figure A.2. TOF-SIMS imaging data from sample containing hafnium-patterned regions on gold. The bright areas correspond to higher ion yields. In the images for AuO_xHf fragments, the higher ion yields closely follow the HfO pattern at left. The absence of AuHf seems to suggest that the hafnium surface species does not interact with gold directly.

Considering the overall ion yields are quite low for the AuO_xHf species, one method for more clearly showing the contrast between regions of higher ion yields and regions of noise is to divide the images by the total ion image of the sample. Figure A.3 below shows the total ion image and the images for the HfO and sum of the AuO_xHf fragments. In addition, the HfO and AuO_xHf images have been normalized to the total ion image for comparison. The AuO_xHf ion yields track the pattern of the HfO fragments quite closely, and the pattern is more clearly distinguished from the background.

Total Ion   HfO   HfO/total ion AuO_xHf AuO_xHf/total ion
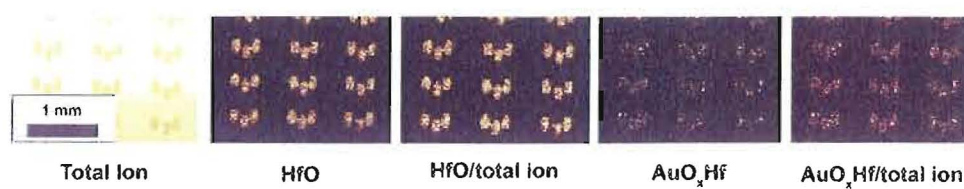
Figure A.3. TOF-SIMS image data of the sum of AuO_xHf fragments and HfO fragments normalized to the total ion image (at left). The AuO_xHf pattern is clearly distinguished from the background, and it matches the HfO pattern shown.

APPENDIX B

SUPPORTING INFORMATION FOR CHAPTER III:

SURFACE MODIFICATION STRATEGY FOR THE FORMATION OF EXTENDED,

HIGH-DENSITY GOLD NANOPARTICLE MONOLAYERS ON THERMALLY

GROWN SILICON DIOXIDE

Introduction

A series of experiments is described in which the optimum treatment conditions

are determined for regeneration of surface silanol functional groups on thermal silicon

dioxide substrates. The surface treatment steps involve both an oxygen plasma etch and a

wet chemical treatment. Optimization of wet chemical treatments has been described

elsewhere.[1] For the oxygen plasma etch, the optimized parameters were time, oxygen

pressure, and RF power. The resulting surface silanol content is not measured directly.

Rather, treated thermal silicon dioxide substrates are modified with a hafnium(IV) layer

by reaction in an aqueous solution of $HfOCl_2$, and the Hf content of these substrates is

determined by X-ray photoelectron spectroscopy. Since $HfOCl_2$ has been shown to react

with surface silanol functional groups and to be unreactive toward siloxane,[2] the efficacy

of surface silanol regeneration treatments is inferred from the resulting Hf: Si ratios.

This appendix also describes the removal of free ligand from aqueous solutions of gold nanoparticles functionalized with 2-mercaptoethylphosphonic acid after ligand exchange. Removal of free ligand is essential to the formation of dense gold nanoparticle monolayers in our studies because free ligand would compete with functionalized nanoparticles for binding sites on hafnium-modified SiO_2 and decrease the density of the nanoparticle monolayers obtained. ^{1}H NMR spectra acquired before and after diafiltration of the nanoparticle solution demonstrate the effectiveness of this purification method for removal of free ligand from aqueous solutions of nanoparticles.

Experimental

Materials. Hafnium dichloride oxide octahydrate (Alfa Aesar; 99.998%) was used as received. Deionized water (18.2 MΩ-cm) was purified with a Barnstead Nanopure Diamond system.

Nanoparticle Synthesis and Purification. Functionalized gold nanoparticles were prepared as described in Chapter III. Briefly, gold nanoparticles ($d_{core} \approx 1.5$ nm) were synthesized first as triphenylphosphine-stabilzed precursors according to a previously reported synthesis.[3] The phosphine-stabilized intermediates were functionalized with 2-mercaptoethylphosphonic acid through a biphasic ligand exchange reaction. The aqueous and organic fractions were separated, and the aqueous fraction was washed with dichloromethane (3 x 50 mL). Residual dichloromethane was removed by rotary evaporation. In order to remove excess free ligand and buffer ions, the nanoparticle solution was concentrated to 20 mL and was purified by diafiltration using a

Minimate 10 kD diafiltration membrane (Pall Life Sciences) and 50 volume equivalents (1 L) of deionized water.[4] The purified solution was concentrated to 20 mL and lyophilized overnight. ^{1}H NMR confirms the completion of the exchange reaction and the removal of free ligand from the product.

Preparation of Substrates. The Si substrates used in these experiments were cut from n-type <100> wafers with 10-20 Ω-cm resistivity and a 3-μm thermal oxide layer (Wafer World). Prior to plasma optimization studies, the SiO_2 surfaces were cleaned in a solution of dilute SC-1 (dSC-1; 100:4:1 H_2O: 30% H_2O_2: 30% NH_4OH) at 70 °C for 15 min to remove adventitious organic contamination and inorganic particulates. Substrates were rinsed with copious amounts of deionized water and dried under a stream of argon prior to oxygen plasma treatment. Oxygen plasma treatments were carried out using a March Plasma Systems CS-1701 Plasma Etcher. Following plasma treatment, the substrates were immediately immersed in a rinsing bath of deionized water and transferred to a 5 mM aqueous solution of $HfOCl_2$ for three days at 45 °C. Substrates were then removed from this solution, sonicated for 5 min in deionized water to remove any physisorbed material, rinsed with deionized water, and dried under a stream of argon prior to XPS analysis.

Analysis Techniques. X-ray photoelectron spectroscopy measurements were conducted using a Kratos AXIS HSi Electron Spectrometer (Kratos Analytical, Chestnut Ridge, NY) with a monochromated Al Kα X-ray source, operated at 13.5 kV accelerating

voltage and 10 mA emission current.[†] Hf: Si ratios were determined by calculating the areas underneath the Hf 4d and Si 2p peaks (Fig. B.1) and correcting these areas using the relative sensitivity factors for each element. The normalized areas were used to calculate atomic concentrations. ^{1}H NMR spectra of water-soluble gold nanoparticles were collected using a Varian Inova 300 NMR Spectrometer.
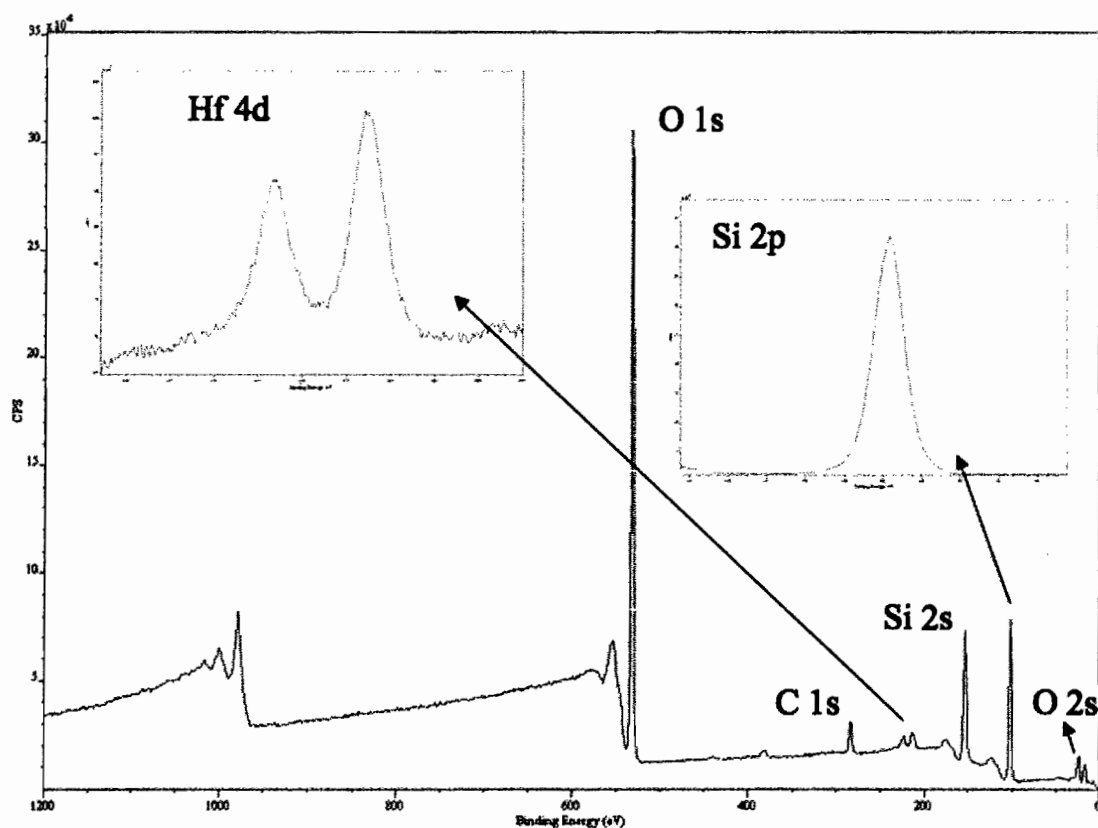
Fig. B.1. XPS spectrum of hafnium-modified SiO_2. Characteristic peaks for oxygen, carbon, silicon and hafnium are shown. The two peaks used for quantitative analysis (Hf 4d and Si 2p) are shown as region scans collected using 0.2 eV steps and 300 ms dwell time.

[†] The XPS data reported in this appendix was collected using the Kratos AXIS HSi spectrometer at the University of Oregon CAMCOR facility prior to instrument failure. XPS data in Chapter III was collected using the Kratos AXIS Ultra spectrometer at the University of Utah Surface Analysis and Nanofabrication Laboratory.

Results & Discussion

Optimization of Plasma Treatment Parameters. In order to determine the optimum oxygen pressure range for plasma treatment, a series of experiments were carried out in which SiO_2 substrates were treated in oxygen plasma pressures of 150 mT, 500 mT, and 600 mT. The lower-pressure treatment was selected as a physical etch, while the higher-pressure treatments were selected as chemical etch treatments.[5] The RF power was 400 W, and the treatment time ranged from one to four minutes. Immediately following plasma treatment, the substrates were immersed in deionized water and transferred to a 5 mM $HfOCl_2$ solution for three days at 45 °C. The Hf: Si ratio was determined for each sample and plotted versus the etch time (Fig. B.2).[†] The 150 mT oxygen plasma treatment resulted in the highest hafnium coverage for all treatment times. This is likely due to physical etching of the topmost surface layers, exposing reactive surface groups that, upon exposure to water in the air or upon immersion in water, react to form surface silanol functional groups.

In order to determine the optimum oxygen plasma treatment time for surface silanol regeneration, a series of experiments were carried out in which the oxygen pressure was held constant at 150 mT and the RF power at 400 W, while the treatment time was varied. After the plasma step, the substrates were treated with $HfOCl_2$ as previously described. The resulting Hf: Si ratios were determined by XPS and plotted

---

[†] In Chapter III, [Hf]:[Si+O] ratios were reported because both native and thermal SiO_2 substrates were utilized. Due to diminished count rates from the Kratos AXIS HSi XPS instrument at the University of Oregon CAMCOR facility at the time of these studies, only Hf and Si were analyzed in the interest of time. Since all samples described in this appendix were cut from the same thermal SiO_2 substrate, it is reasonable to neglect oxygen content so long as atomic concentration *ratios* are reported, rather than absolute atomic concentrations.

against plasma treatment time (Fig. B.3). The Hf: Si ratio reaches a maximum for plasma

treatments between 20 and 30 seconds. Following similar methods and utilizing XPS

quantitative analysis, the optimum plasma pressure and RF power were determined to be

200 mT and 150 W, respectively.

Hafnium Content of Plasma-Treated Silicon Dioxide
[Hf]:[Si] Ratio vs. Treatment Time for Selected Oxygen Pressures
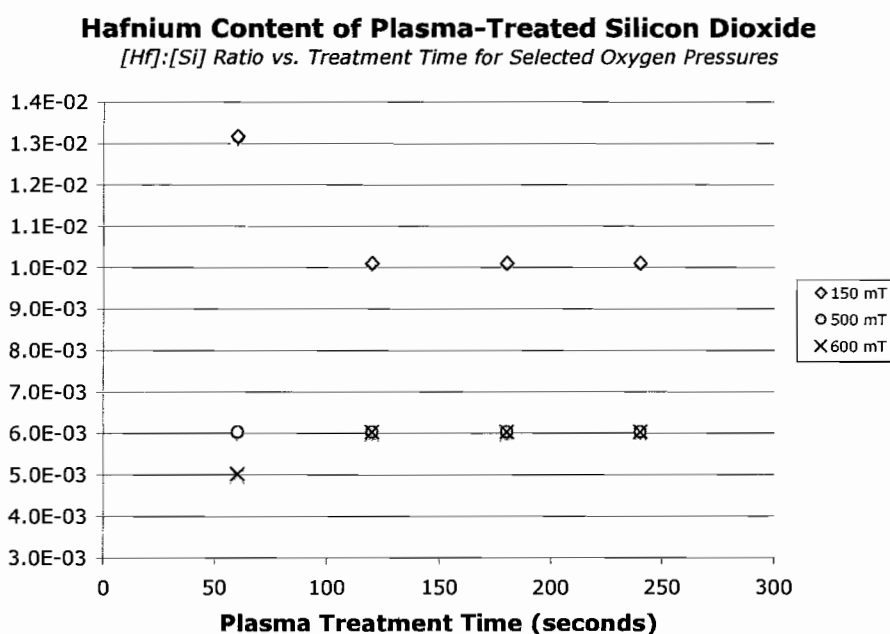
Figure B.2. Hf:Si ratio versus plasma etch time for a range of oxygen pressures. The hafnium coverage after 150 mT oxygen plasma treatment is higher than that observed for higher pressures.

Determination of HfOCl$_2$ Treatment Time. Finally, we wished to determine if

the previously utlilized treatment time of 72 hr in aqueous HfOCl$_2$ solution[2] was

necessary to ensure completion of this surface modification reaction. Thermal SiO$_2$

substrates were treated in oxygen plasma (150 mT, 400 W, 30 sec), rinsed with water,

and transferred to 5 mM HfOCl$_2$ solution. Substrates were removed from this solution at

various times and analyzed by XPS. Hf: Si ratios determined by XPS showed that the

hafnium content reached its maximum value after one hour rather than after 72 hours (not

shown). Given this information, we used an HfOCl$_2$ treatment time of at least four hours

for all studies in Chapter III to ensure complete modification of SiO$_2$ surfaces. No

differences in Hf coverage were noted for samples that underwent a 72-hour HfOCl$_2$

treatment versus those that underwent only a 4-hour treatment.

Hf:Si Ratio vs. Plasma Etch Time
400 W RF Power, 150 mT Oxygen Pressure
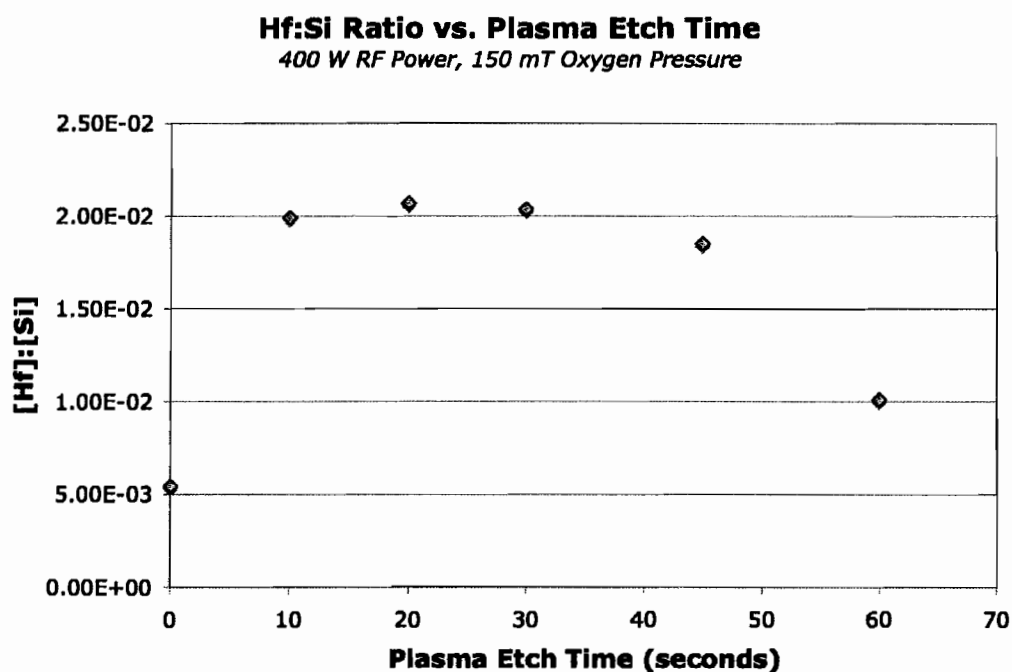
Figure B.3. Hf: Si ratio versus plasma treatment time. Plasma conditions were 150 mT oxygen pressure and 400 W RF power. The atomic concentration of hafnium reaches a maximum value after approximately 20-30 seconds of plasma treatment.

Removal of Free Ligand by Diafiltration. The removal of excess free ligand is

essential to purification of the nanoparticles used in this study. Free ligand competes

with the phosphonic acid-functionalized gold nanoparticles for binding sites on the Hf-modified silicon dioxide surface, so any residual free ligand in solution will inhibit the formation of extended, high-density gold nanoparticle monolayers. Diafiltration is a powerful tool for removal of small molecules from solutions of nanomaterials. Figures B.4 and B.5 below show ^{1}H NMR spectra of gold nanoparticles dissolved in D_2O before and after diafiltration using 50 volume equivalents of deionized water. The sharp resonances ($\delta = 2.1$ ppm and $\delta = 2.7$ ppm) from the free ligand can be easily distinguished from the broad resonances from nanoparticle-bound ligands. After diafiltration, no free ligand is observed in solution.
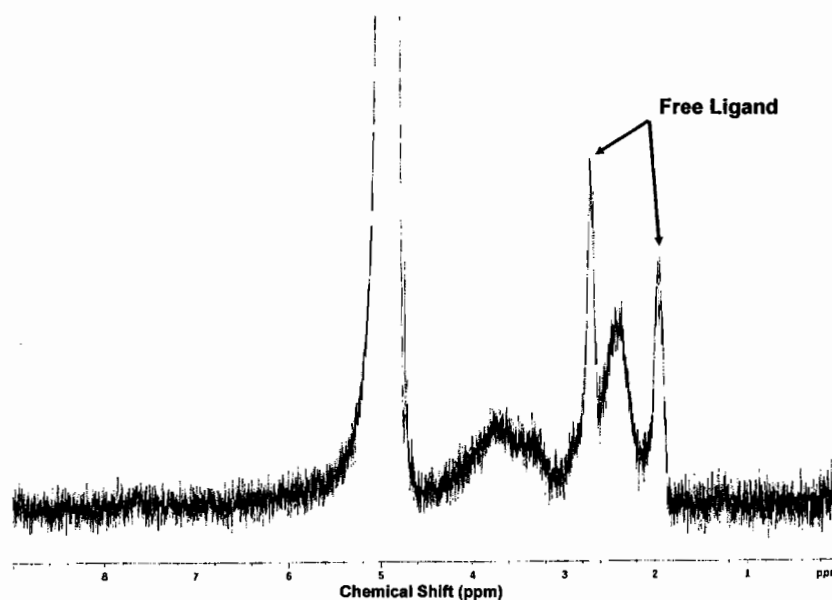
Figure B.4. ^{1}H NMR spectrum of unpurified phosphonic acid-functionalized gold nanoparticles in D_2O. The broad resonances ($\delta \approx 2.3$ ppm and $\delta \approx 3.6$ ppm) from bound 2-MEPA can be observed, along with sharp multiplets ($\delta \approx 2.0$ ppm and $\delta \approx 2.8$ ppm) from free 2-MEPA in solution.
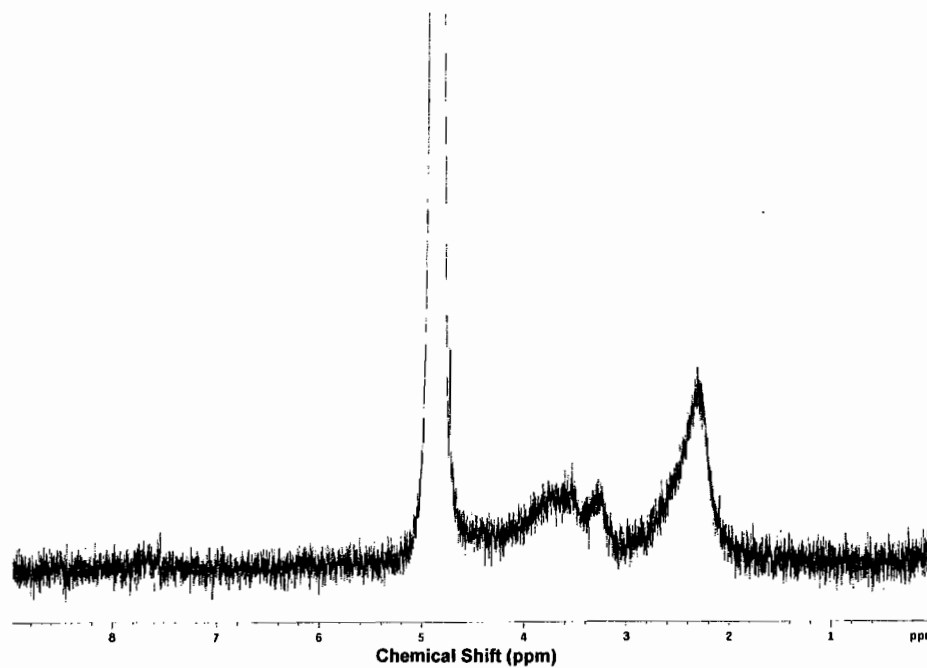
Figure B.5. ^{1}H NMR spectrum of phosphonic acid-functionalized gold nanoparticles in D_2O after diafiltration with 50 volume equivalents of water. Free ligand is no longer detectable, leaving only the broad resonances from bound 2-MEPA on the nanoparticles.

BIBLIOGRAPHY

CHAPTER I

1. Feynman, R. P. A lecture in engineering science. In California Institute of Technology, 1959.

2. Binning, G.; Rohrer, H.; Gerber, C.; Weibel, E. Surface Studies by Scanning Tunneling Microscopy. *Phys. Rev. Lett.* **1982,** *49,* 57-61.

3. Cuberes, M. T.; Schlittler, R. R.; Gimzewski, J. K. Room-Temperature Repositioning of Individual C_{60} Molecules at Cu Steps: Operation of a Molecular Counting Device. *Appl. Phys. Lett.* **1996,** *69,* 3016-3018.

4. Eigler, D. M.; Schweizer, E. K. Positioning Single Atoms with a Scanning Tunneling Microscope. *Nature* **1990,** *344,* 524-526.

5. Zeppenfeld, P.; Eigler, D. M.; Schweizer, E. K. Even Atoms Are Manipulated. *Recherche* **1992,** *23,* 360-362.

6. Zeppenfeld, P.; Lutz, C. P.; Eigler, D. M. Manipulating Atoms and Molecules with a Scanning Tunneling Microscope. *Ultramicroscopy* **1992,** *42,* 128-133.

7. Cao, G. *Nanostructures and Nanomaterials: Synthesis, Properties, and Applications.* Imperial College Press: London, 2004; p 433.

8. Schmid, G. *Nanoparticles: From Theory to Application.* Wiley-VCH: Weinheim, 2004.

9. Tian, Y. C.; Newton, T.; Kotov, N. A.; Guldi, D. M.; Fendler, J. H. Coupled Composite CdS-CdSe and Core-Shell Yypes of (CdS)CdSe and (CdSe)CdS Nanoparticles. *J. Phys. Chem.* **1996,** *100,* 8927-8939.

10. Hu, J. T.; Odom, T. W.; Lieber, C. M. Chemistry and Physics in One Dimension: Synthesis and Properties of Nanowires and Nanotubes. *Acc. Chem. Res.* **1999,** *32,* 435-445.

11. Wang, X. D.; Song, J. H.; Wang, Z. L. Nanowire and Nanobelt Arrays of Zinc Oxide from Synthesis to Properties and to Novel Devices. *J. Mater. Chem.* **2007,** *17,* 711-720.

12. Rao, C. N. R.; Govindaraj, A. Carbon Nanotubes from Organometallic Precursors. *Acc. Chem. Res.* **2002,** *35,* 998-1007.

13. Bastys, V.; Pastoriza-Santos, I.; Rodriguez-Gonzalez, B.; Vaisnoras, R.; Liz-Marzan, L. M. Formation of Silver Nanoprisms with Surface Plasmons at Communication Wavelengths. *Adv. Func. Mater.* **2006,** *16,* 766-773.

14. Millstone, J. E.; Metraux, G. S.; Mirkin, C. A. Controlling the Edge Length of Gold Nanoprisms via a Seed-Mediated Approach. *Adv. Func. Mater.* **2006,** *16,* 1209-1214.

15. Bachmann, H.-G. Gold for Coinage: History and Metallurgy. In *Gold: Progress in Chemistry, Biochemistry, and Technology*, Schmidbaur, H., Ed. John Wiley & Sons: New York, 1999; pp 3-63.

16. Enghag, P. *Encyclopedia of the Elements.* Wiley-VCH: Weinheim, 2004; p 1243.

17. Puddephatt, R. J. Gold Metal and Gold Alloys in Electronics and Thin Film Technology. In *Gold: Progress in Chemistry, Biochemistry, and Technology.*, Schmidbaur, H., Ed. John Wiley & Sons: New York, 1999; pp 237-256.

18. Chen, M. S.; Goodman, D. W. Catalytically Active Gold: From Nanoparticles to Ultrathin Films. *Acc. Chem. Res.* **2006,** *39,* 739-746.

19. Haruta, M.; Kobayashi, T.; Sano, H.; Yamada, N. Novel Gold Catalysts for the Oxidation of Carbon Monoxide at a Temperature Far Below 0 °C. *Chem. Lett.* **1987,** *2,* 405-408.

20. Haruta, M.; Yamada, N.; Kobayashi, T.; Iijima, S. Gold Catalysts Prepared by Coprecipitation for Low-Temperature Oxidation of Hydrogen and of Carbon-Monoxide. *J. Catal.* **1989,** *115,* 301-309.

21. Woehrle, G. H.; Warner, M. G.; Hutchison, J. E., Ligand Exchange Reactions Yield Subnanometer, Thiol-Stabilized Gold Particles with Defined Optical Transitions. *J. Phys. Chem. B* **2002,** *106,* 9979-9981.

22.   Parak, W. J.; Manna, L.; Simmel, F. C.; Gerion, D.; Alivisatos, A. P. Quantum
       Dots. In *Nanoparticles: From Theory to Applications*, Schmid, G., Ed. Wiley-
       VCH: Weinheim, 2004; pp 4-49.

23.   Ratner, M. A.; Ratner, D. *Nanotechnology: A Gentle Introduction to the Next Big
       Idea.* Prentice Hall: Upper Saddle River, NJ, 2003.

24.   Simon, U. Electrical Properties of Metal Nanoparticles. In *Nanoparticles: From
       Theory to Application*, Schmid, G., Ed. Wiley-VCH: Weinheim, 2004; pp 328-
       367.

25.   Wasshuber, C. *Computational Single-Electronics.* Springer: New York, 2001.

26.   Bansal, C.; Sarkar, S. Phase Transformations in Nanocrystalline Alloys
       Synthesized by Mechanical Alloying. *J. Mater. Sci.* **2004,** *39,* 5023-5029.

27.   Dick, K.; Dhanasekaran, T.; Zhang, Z. Y.; Meisel, D. Size-Dependent Melting of
       Silica-Encapsulated Gold Nanoparticles. *J. Am. Chem. Soc.* **2002,** *124,* 2312-
       2317.

28.   Ross, J.; Andres, R. P. Melting Temperature of Small Clusters. *Surf. Sci.* **1981,**
       106, 11-17.

29.   Brown, L. O.; Hutchison, J. E. Convenient Preparation of Stable, Narrow-
       Dispersity Gold Nanocrystals by Ligand Exchange Reactions. *J. Am. Chem. Soc.*
       1997, *119,* 12384-12385.

30.   Brust, M.; Fink, J.; Bethell, D.; Schiffrin, D. J.; Kiely, C. Synthesis and
       Reactions of Functionalized Gold Nanoparticles. *J. Chem. Soc., Chem. Commun.*
       1995, *16,* 1655-1656.

31.   Brust, M.; Walker, M.; Bethell, D.; Schiffrin, D. J.; Whyman, R. Synthesis of
       Thiol-Derivatized Gold Nanoparticles in a 2-Phase Liquid-Liquid System. *J.
       Chem. Soc., Chem. Commun.* **1994,** *7,* 801-802.

32.   Hostetler, M. J.; Green, S. J.; Stokes, J. J.; Murray, R. W. Monolayers in Three
       Dimensions: Synthesis and Electrochemistry of Omega-Functionalized
       Alkanethiolate-Stabilized Gold Cluster Compounds. *J. Am. Chem. Soc.* **1996,** *118,*
       4212-4213.

33.   Woehrle, G. H.; Brown, L. O.; Hutchison, J. E. Thiol-Functionalized, 1.5-nm
       Gold Nanoparticles through Ligand Exchange Reactions: Scope and Mechanism
       of Ligand Exchange. *J. Am. Chem. Soc.* **2005,** *127,* 2172-2183.

34. Foster, E. W.; Kearns, G. J.; Goto, S.; Hutchison, J. E. Patterned Gold-Nanoparticle Monolayers Assembled on the Oxide of Silicon. *Adv. Mater.* **2005,** *17,* 1542-1545.

35. Olofsson, L.; Rindzevicius, T.; Pfeiffer, I.; Kall, M.; Hook, F. Surface-Based Gold-Nanoparticle Sensor for Specific and Quantitative DNA Hybridization Detection. *Langmuir* **2003,** *19,* 10414-10419.

36. Warner, M. G.; Hutchison, J. E. Linear Assemblies of Nanoparticles Electrostatically Organized on DNA Scaffolds. *Nature Mater.* **2003,** *2,* 272-277.

37. Giaever, I.; Zeller, H. R. Superconductivity of Small Tin Particles Measured by Tunneling. *Phys. Rev. Lett.* **1968,** *20,* 1504-1507.

38. Andres, R. P.; Datta, S.; Dorogi, M.; Gomez, J.; Henderson, J. I.; Janes, D. B.; Kolagunta, V. R.; Kubiak, C. P.; Mahoney, W.; Osifchin, R. F.; Reifenberger, R.; Samanta, M. P.; Tian, W. Room Temperature Coulomb Blockade and Coulomb Staircase from Self-Assembled Nanostructures. *J. Vac. Sci. Technol., A* **1996,** *14,* 1178-1183.

39. Klein, D. L.; Roth, R.; Lim, A. K. L.; Alivisatos, A. P.; McEuen, P. L. A Single-Electron Transistor Made from a Cadmium Selenide Nanocrystal. *Nature* **1997,** *389,* 699-701.

40. Klein, D. L.; McEuen, P. L.; Katari, J. E. B.; Roth, R.; Alivisatos, A. P. An Approach to Electrical Studies of Single Nanocrystals. *Appl. Phys. Lett.* **1996,** *68,* 2574-2576.

41. Santhanam, V.; Andres, R. P. Microcontact Printing of Uniform Nanoparticle Arrays. *Nano Lett.* **2004,** *4,* 41-44.

42. Santhanam, V.; Liu, J.; Agarwal, R.; Andres, R. P. Self-Assembly of Uniform Monolayer Arrays of Nanoparticles. *Langmuir* **2003,** *19,* 7881-7887.

43. Brown, J. J.; Porter, J. A.; Daghlian, C. P.; Gibson, U. J. Ordered Arrays of Amphiphilic Gold Nanoparticles in Langmuir Monolayers. *Langmuir* **2001,** *17,* 7966-7969.

44. Bigioni, T. P.; Lin, X. M.; Nguyen, T. T.; Corwin, E. I.; Witten, T. A.; Jaeger, H. M. Kinetically Driven Self-Assembly of Highly Ordered Nanoparticle Monolayers. *Nature Mater.* **2006,** *5,* 265-270.

45. Parthasarathy, R.; Lin, X. M.; Jaeger, H. M. Electronic Transport in Metal Nanocrystal Arrays: The Effect of Structural Disorder on Scaling Behavior. *Phys. Rev. Lett.* **2001,** *87,* 186807.

46. Shipway, A. N.; Katz, E.; Willner, I. Nanoparticle Arrays on Surfaces for Electronic, Optical, and Sensor Applications. *ChemPhysChem* **2000,** *1,* 18-52.

47. He, H. X.; Zhang, H.; Li, Q. G.; Zhu, T.; Li, S. F. Y.; Liu, Z. F. Fabrication of Designed Architectures of Au Nanoparticles on Solid Substrate with Printed Self-Assembled Monolayers as Templates. *Langmuir* **2000,** *16,* 3846-3851.

48. Liu, S. T.; Maoz, R.; Schmid, G.; Sagiv, J. Template Guided Self-Assembly of Au_{55} Clusters on Nanolithographically Defined Monolayer Patterns. *Nano Lett.* **2002,** *2,* 1055-1060.

49. Bandyopadhyay, K.; Patil, V.; Vijayamohanan, K.; Sastry, M. Adsorption of Silver Colloidal Particles Through Covalent Linkage to Self-Assembled Monolayers. *Langmuir* **1997,** *13,* 5244-5248.

50. Colvin, V. L.; Goldstein, A. N.; Alivisatos, A. P. Semiconductor Nanocrystals Covalently Bound to Metal Surfaces with Self-Assembled Monolayers. *J. Am. Chem. Soc.* **1992,** *114,* 5221-5230.

51. Mafune, F.; Kohno, J.; Takeda, Y.; Kondow, T. Dissociation and Aggregation of Gold Nanoparticles Under Laser Irradiation. *J. Phys. Chem. B* **2001,** *105,* 9050-9056.

52. Mafune, F.; Kohno, J.; Takeda, Y.; Kondow, T.; Sawabe, H. Formation of Gold Nanoparticles by Laser Ablation in Aqueous Solution of Surfactant. *J. Phys. Chem. B* **2001,** *105,* 5114-5120.

53. Stoeva, S.; Klabunde, K. J.; Sorensen, C. M.; Dragieva, I. Gram-Scale Synthesis of Monodisperse Gold Colloids by the Solvated Metal Atom Dispersion Method and Digestive Ripening and Their Organization into Two- and Three-Dimensional Structures. *J. Am. Chem. Soc.* **2002,** *124,* 2305-2311.

54. Turkevich, J.; Stevenson, P. C.; Hillier, J. The Nucleation and Growth Processes in the Synthesis of Colloidal Gold. *Discuss. Faraday Soc.* **1951,** *11,* 55-75.

55. Dahl, J. A.; Jespersen, M. L.; Hutchison, J. E. Functionalization of Citrate-Stabilized Gold Nanoparticles with Water-Soluble Thiols. *Manuscript in Preparation* **2008.**

56. Lin, S. Y.; Tsai, Y. T.; Chen, C. C.; Lin, C. M.; Chen, C. H. Two-Step Functionalization of Neutral and Positively Charged Thiols onto Citrate-Stabilized Au Nanoparticles. *J. Phys. Chem. B* **2004**, *108*, 2134-2139.

57. Zhu, T.; Vasilev, K.; Kreiter, M.; Mittler, S.; Knoll, W. Surface Modification of Citrate-Reduced Colloidal Gold Nanoparticles with 2-Mercaptosuccinic Acid. *Langmuir* **2003**, *19*, 9518-9525.

58. Maier, S. A.; Brongersma, M. L.; Kik, P. G.; Meltzer, S.; Requicha, A. A. G.; Atwater, H. A. Plasmonics - A Route to Nanoscale Optical Devices. *Adv. Mater.* **2001**, *13*, 1501-1505.

59. Maier, S. A.; Kik, P. G.; Atwater, H. A. Optical Pulse Propagation in Metal Nanoparticle Chain Waveguides. *Phys. Rev. B* **2003**, *67*, 205402.

60. Schmid, G.; Pfeil, R.; Boese, R.; Bandermann, F.; Meyer, S.; Calis, G. H. M.; Vandervelden, W. A. $Au_{55}[P(C_6H_5)_3]_{12}Cl_6$ - A Gold Cluster of an Exceptional Size. *Chem. Ber.* **1981**, *114*, 3634-3642.

61. Kreutz, T. C.; Gwinn, E. G.; Artzi, R.; Naaman, R.; Pizem, H.; Sukenik, C. N. Modification of Ferromagnetism in Semiconductors by Molecular Monolayers. *Appl. Phys. Lett.* **2003**, *83*, 4211-4213.

62. Brown, L. O.; Hutchison, J. E. Controlled Growth of Gold Nanoparticles During Ligand Exchange. *J. Am. Chem. Soc.* **1999**, *121*, 882-883.

63. Donkers, R. L.; Song, Y.; Murray, R. W. Substituent Effects on the Exchange Dynamics of Ligands on 1.6-nm Diameter Gold Nanoparticles. *Langmuir* **2004**, *20*, 4703-4707.

64. Guo, R.; Song, Y.; Wang, G. L.; Murray, R. W. Does Core Size Matter in the Kinetics of Ligand Exchanges of Monolayer-Protected Au Clusters? *J. Am. Chem. Soc.* **2005**, *127*, 2752-2757.

65. Kassam, A.; Bremner, G.; Clark, B.; Ulibarri, G.; Lennox, R. B. Place Exchange Reactions of Alkyl Thiols on Gold Nanoparticles. *J. Am. Chem. Soc.* **2006**, *128*, 3476-3477.

66. Sweeney, S. F.; Woehrle, G. H.; Hutchison, J. E. Rapid Purification and Size Separation of Gold Nanoparticles via Diafiltration. *J. Am. Chem. Soc.* **2006**, *128*, 3190-3197.

67. Woehrle, G. H.; Warner, M. G.; Hutchison, J. E. Molecular-Level Control of Feature Separation in One-Dimensional Nanostructure Assemblies Formed by Biomolecular Nanolithography. *Langmuir* **2004,** *20,* 5982-5988.

68. Liao, J.; Bernard, L.; Langer, M.; Schonenberger, C.; Calame, M. Reversible Formation of Molecular Junctions in 2D Nanoparticle Arrays. *Adv. Mater.* **2006,** *18,* 2444-2447.

69. Xu, H.; Hong, R.; Wang, X. Y.; Arvizo, R.; You, C. C.; Samanta, B.; Patra, D.; Tuominen, M. T.; Rotello, V. M. Controlled Formation of Patterned Gold Films via Site-Selective Deposition of Nanoparticles onto Polymer-Templated Surfaces. *Adv. Mater.* **2007,** *19,* 1383-1386.

70. Love, J. C.; Estroff, L. A.; Kriebel, J. K.; Nuzzo, R. G.; Whitesides, G. M. Self-Assembled Monolayers of Thiolates on Metals as a Form of Nanotechnology. *Chem. Rev.* **2005,** *105,* 1103-1169.

71. Ulman, A. *An Introduction to Ultrathin Organic Films: From Langmuir Blodgett to Self-Assembly.* Academic Press, Inc.: San Diego, CA, 1991; p 442.

72. Ulman, A. Formation and Structure of Self-Assembled Monolayers. *Chem. Rev.* **1996,** *96,* 1533-1554.

73. Allara, D. L.; Nuzzo, R. G. Spontaneously Organized Molecular Assemblies. 1. Formation, Dynamics, and Physical Properties of Normal-Alkanoic Acids Adsorbed from Solution on an Oxidized Aluminum Surface. *Langmuir* **1985,** *1,* 45-52.

74. Allara, D. L.; Nuzzo, R. G. Spontaneously Organized Molecular Assemblies. 2. Quantitative Infrared Spectroscopic Determination of Equilibrium Structures of Solution-Adsorbed Normal-Alkanoic Acids on an Oxidized Aluminum Surface. *Langmuir* **1985,** *1,* 52-66.

75. Schlotter, N. E.; Porter, M. D.; Bright, T. B.; Allara, D. L. Formation and Structure of a Spontaneously Adsorbed Monolayer of Arachidic on Silver. *Chem. Phys. Lett.* **1986,** *132,* 93-98.

76. Nuzzo, R. G.; Zegarski, B. R.; Dubois, L. H. Fundamental Studies of the Chemisorption of Organosulfur Compounds on Au(111) - Implications for Molecular Self-Assembly on Gold Surfaces. *J. Am. Chem. Soc.* **1987,** *109,* 733-740.

77. Love, J. C.; Wolfe, D. B.; Haasch, R.; Chabinyc, M. L.; Paul, K. E.; Whitesides, G. M.; Nuzzo, R. G. Formation and Structure of Self-Assembled Monolayers of Alkanethiolates on Palladium. *J. Am. Chem. Soc.* **2003,** *125,* 2597-2609.

78. Li, Z. Y.; Chang, S. C.; Williams, R. S. Self-Assembly of Alkanethiol Molecules onto Platinum and Platinum Oxide Surfaces. *Langmuir* **2003,** *19,* 6744-6749.

79. Lim, H.; Carraro, C.; Maboudian, R.; Pruessner, M. W.; Ghodssi, R. Chemical and Thermal Stability of Alkanethiol and Sulfur Passivated InP(100). *Langmuir* **2004,** *20,* 743-747.

80. Yamamoto, H.; Butera, R. A.; Gu, Y.; Waldeck, D. H. Characterization of the Surface to Thiol Bonding in Self-Assembled Monolayer Films of $C_{12}H_{25}SH$ on InP(100) by Angle-Resolved X-Ray Photoelectron Spectroscopy. *Langmuir* **1999,** *15,* 8640-8644.

81. Sheen, C. W.; Shi, J. X.; Martensson, J.; Parikh, a. N.; Allara, D. L. A New Class of Organized Self-Assembled Monolayers - Alkane Thiols on GaAs(100). *J. Am. Chem. Soc.* **1992,** *114,* 1514-1515.

82. Angst, D. L.; Simmons, G. W. Moisture Absorption Characteristics of Organosiloxane Self-Assembled Monolayers. *Langmuir* **1991,** *7,* 2236-2242.

83. Dugas, V.; Chevalier, Y. Surface Hydroxylation and Silane Grafting on Fumed and Thermal Silica. *J. Colloid Interface Sci.* **2003,** *264,* 354-361.

84. Finklea, H. O.; Robinson, L. R.; Blackburn, a.; Richter, B.; Allara, D.; Bright, T. Formation of an Organized Monolayer by Solution Adsorption of Octadecyltrichlorosilane on Gold - Electrochemical Properties and Structural Characterization. *Langmuir* **1986,** *2,* 239-244.

85. Laibinis, P. E.; Whitesides, G. M.; Allara, D. L.; Tao, Y. T.; Parikh, A. N.; Nuzzo, R. G. Comparison of the Structures and Wetting Properties of Self-Assembled Monolayers of Normal-Alkanethiols on the Coinage Metal Surfaces, Cu, Ag, Au. *J. Am. Chem. Soc.* **1991,** *113,* 7152-7167.

86. Adden, N.; Gamble, L. J.; Castner, D. G.; Hoffmann, A.; Gross, G.; Menzel, H. Phosphonic Acid Monolayers for Binding of Bioactive Molecules to Titanium Surfaces. *Langmuir* **2006,** *22,* 8197-8204.

87. Curreli, M.; Li, C.; Sun, Y. H.; Lei, B.; Gundersen, M. A.; Thompson, M. E.; Zhou, C. W. Selective Functionalization of In_2O_3 Nanowire Mat Devices for Biosensing Applications. *J. Am. Chem. Soc.* **2005,** *127,* 6922-6923.

88.   Trammell, S. A.; Moss, J. A.; Yang, J. C.; Nakhle, B. M.; Slate, C. A.; Odobel, F.; Sykora, M.; Erickson, B. W.; Meyer, T. J. Sensitization of TiO_2 by Phosphonate-Derivatized Proline Assemblies. *Inorg. Chem.* **1999**, *38*, 3665-3669.

89.   Griep-Raming, N.; Karger, M.; Menzel, H. Using Benzophenone-Functionalized Phosphonic Acids to Attach Thin Polymer Films to Titanium Surfaces. *Langmuir* **2004**, *20*, 11811-11814.

90.   Kelley, T. W.; Boardman, L. D.; Dunbar, T. D.; Muyres, D. V.; Pellerite, M. J.; Smith, T. Y. P. High-Performance OTFTs Using Surface-Modified Alumina Dielectrics. *J. Phys. Chem. B* **2003**, *107*, 5877-5881.

91.   Pawsey, S.; Yach, K.; Reven, L. Self-Assembly of Carboxyalkylphosphonic Acids on Metal Oxide Powders. *Langmuir* **2002**, *18*, 5205-5212.

92.   Messerschmidt, C.; Schwartz, D. K. Growth Mechanisms of Octadecylphosphonic Acid Self-Assembled Monolayers on Sapphire (Corundum): Evidence for a Quasi-Equilibrium Triple Point. *Langmuir* **2001**, *17*, 462-467.

93.   Liakos, I. L.; Newman, R. C.; McAlpine, E.; Alexander, M. R. Study of the Resistance of SAMs on Aluminium to Acidic and Basic Solutions Using Dynamic Contact Angle Measurement. *Langmuir* **2007**, *23*, 995-999.

94.   Guang, C.; Hong, H. G.; Mallouk, T. E. Layered Metal Phosphates and Phosphonates - from Crystals to Monolayers. *Acc. Chem. Res.* **1992**, *25*, 420-427.

95.   Adolphi, B.; Jahne, E.; Busch, G.; Cai, X. D. Characterization of the Adsorption of Omega-(Thiophene-3-yl Alkyl) Phosphonic Acid on Metal Oxides with AR-XPS. *Anal. Bioanal. Chem.* **2004**, *379*, 646-652.

96.   Frey, B. L.; Hanken, D. G.; Corn, R. M. Vibrational Spectroscopic Studies of the Attachment Chemistry for Zirconium Phosphonate Multilayers at Gold and Germanium Surfaces. *Langmuir* **1993**, *9*, 1815-1820.

97.   Hong, H. G.; Sackett, D. D.; Mallouk, T. E. Adsorption of Well-Ordered Zirconium Phosphonate Multilayer Films on High Surface-Area Silica. *Chem. Mater.* **1991**, *3*, 521-527.

98.   Lee, H.; Kepley, L. J.; Hong, H. G.; Akhter, S.; Mallouk, T. E. Adsorption of Ordered Zirconium Phosphonate Multilayer Films on Silicon and Gold Surfaces. *J. Phys. Chem.* **1988**, *92*, 2597-2601.

99. Lee, H.; Kepley, L. J.; Hong, H. G.; Mallouk, T. E. Inorganic Analogs of Langmuir-Blodgett Films - Adsorption of Ordered Zirconium 1,10-Decanebisphosphonate Multilayers on Silicon Surfaces. *J. Am. Chem. Soc.* **1988,** *110,* 618-620.

100. Schilling, M. L.; Katz, H. E.; Stein, S. M.; Shane, S. F.; Wilson, W. L.; Buratto, S.; Ungashe, S. B.; Taylor, G. N.; Putvinski, T. M.; Chidsey, C. E. D. Structural Studies of Zirconium Alkylphosphonate Monolayers and Multilayer Assemblies. *Langmuir* **1993,** *9,* 2156-2160.

101. Zeppenfeld, A. C.; Fiddler, S. L.; Ham, W. K.; Klopfenstein, B. J.; Page, C. J. Variation of Layer Spacing in Self-Assembled Hafnium-1,10-Decanediylbis(Phosphonate) Multilayers as Determined by Ellipsometry and Grazing Angle X-Ray-Diffraction. *J. Am. Chem. Soc.* **1994,** *116,* 9158-9165.

102. Neff, G. A.; Page, C. J. Hydrolysis of Surface-Bound Phosphonate Esters for the Self-Assembly of Multilayer Films: Use of Solid State Magic Angle Spinning ^{31}P NMR as a Probe of Reactions on Surfaces. *Langmuir* **1996,** *12,* 238-242.

103. Gardner, T. J.; Frisbie, C. D.; Wrighton, M. S. Systems for Orthogonal Self-Assembly of Electroactive Monolayers on Au and ITO - An Approach to Molecular Electronics. *J. Am. Chem. Soc.* **1995,** *117,* 6927-6933.

104. Jespersen, M. L.; Inman, C. E.; Kearns, G. J.; Foster, E. W.; Hutchison, J. E. Alkanephosphonates on Hafnium-Modified Gold: A New Class of Self-Assembled Organic Monolayers. *J. Am. Chem. Soc.* **2007,** *129,* 2803-2807.

105. Laibinis, P. E.; Hickman, J. J.; Wrighton, M. S.; Whitesides, G. M. Orthogonal Self-Assembled Monolayers - Alkanethiols on Gold and Alkane Carboxylic-Acids on Alumina. *Science* **1989,** *245,* 845-847.

106. Kibel, M. H. X-Ray Photelectron Spectroscopy. In *Surface Analysis Methods in Materials Science,* 2nd ed.; O'Connor, D. J.; Sexton, B. A.; Smart, R. S. C., Eds. Springer: Berlin, 2003; pp 175-201.

107. Ratner, B.; Castner, D. Electron Spectroscopy for Chemical Analysis. In *Surface Analysis: The Principal Techniques,* Vickerman, J. C., Ed. John Wiley & Sons: New York, 1997; pp 43-96.

108. MacDonald, R. J.; King, B. V. SIMS - Secondary Ion Mass Spectrometry. In *Surface Analysis Methods in Materials Science,* 2nd ed.; O'Connor, D. J.; Sexton, B. A.; Smart, R. S. C., Eds. Springer: Berlin, 2003; pp 127-154.

109. Vickerman, J. C.; Swift, A. Secondary Ion Mass Spectrometry - the Surface Mass Spectrometry. In *Surface Analysis: The Principal Techniques*, Vickerman, J. C., Ed. John Wiley & Sons: New York, 1997; pp 135-213.

110. Turner, P. S.; Nockolds, C. E.; Bulcock, S. Electron Microscope Techniques for Surface Characterization. In *Surface Analysis Methods in Materials Science*, 2nd ed.; O'Connor, D. J.; Sexton, B. A.; Smart, R. S. C., Eds. Springer: Berlin, 2003; pp 85-105.

111. Kearns, G. J.; Foster, E. W.; Hutchison, J. E. Substrates for Direct Imaging of Chemically Functionalized SiO_2 Surfaces by Transmission Electron Microscopy. *Anal. Chem.* **2006,** *78,* 298-303.

112. Joy, D. C. Scanning Electron Microscopy. In *Characterization of Materials, Part I*, Cahn, R. W.; Haasen, P.; Kramer, E. J., Eds. VCH Publishers: New York, 1992; pp 221-249.

113. Goldstein, J. *Scanning Electron Microscopy and X-Ray Microanalysis: A Text for Biologists, Materials Scientists, and Geologists.* 2nd ed.; Plenum Press: New York, 1992.

114. Wasserman, S. R.; Tao, Y. T.; Whitesides, G. M. Structure and Reactivity of Alkylsiloxane Monolayers Formed by Reaction of Alkyltrichlorosilanes on Silicon Substrates. *Langmuir* **1989,** *5,* 1074-1087.

115. Bain, C. D.; Whitesides, G. M. Depth Sensitivity of Wetting - Monolayers of Omega-Mercapto Ethers on Gold. *J. Am. Chem. Soc.* **1988,** *110,* 5897-5898.

116. Bain, C. D.; Whitesides, G. M. Formation of Monolayers by the Coadsorption of Thiols on Gold - Variation in the Length of the Alkyl Chain. *J. Am. Chem. Soc.* **1989,** *111,* 7164-7175.

117. Cassie, A. B. D. Contact Angles. *Discuss. Faraday Soc.* **1948,** *3,* 11-16.

118. Bain, C. D.; Whitesides, G. M. A Study by Contact-Angle of the Acid-Base Behavior of Monolayers Containing Omega-Mercaptocarboxylic Acids Adsorbed on Gold - An Example of Reactive Spreading. *Langmuir* **1989,** *5,* 1370-1378.

CHAPTER II

1. Ulman, A. *An Introduction to Ultrathin Organic Films: From Langmuir-Blodgett to Self-Assembly*; Academic Press: San Diego, CA, 1991.

2. Love, J. C.; Estroff, L. A.; Kriebel, J. K.; Nuzzo, R. G.; Whitesides, G. M. Self-Assembled Monolayers of Thiolates on Metals as a Form of Nanotechnology. *Chem. Rev.* **2005,** *105,* 1103-1169.

3. Kikuchi, A.; Okano, T. Nanostructured Designs of Biomedical Materials: Applications of Cell Sheet Engineering to Functional Regenerative Tissues and Organs. *J. Control Release* **2005,** *101,* 69-84.

4. Witt, D.; Klajn, R.; Barski, P.; Grzybowski, B. A. Applications, Properties, and Synthesis of Omega-Functionalized *n*-Alkanethiols and Disulfides - The Building Blocks of Self-Assembled Monolayers. *Curr. Org. Chem.* **2004,** *8,* 1763-1797.

5. Li, X. M.; Huskens, J.; Reinhoudt, D. N. Reactive Self-Assembled Monolayers on Flat and Nanoparticle Surfaces, and Their Application in Soft and Scanning Probe Lithographic Nanofabrication Technologies. *J. Mater. Chem.* **2004,** *14,* 2954-2971.

6. Smith, R. K.; Lewis, P. A.; Weiss, P. S. Patterning Self-Assembled Monolayers. *Prog. Surf. Sci.* **2004,** *75,* 1-68.

7. Vericat, C.; Vela, M. E.; Salvarezza, R. C. Self-Assembled Monolayers of Alkanethiols on Au(111): Surface Structures, Defects, Dynamics. *Phys. Chem. Chem. Phys.* **2005,** *7,* 3258-3268.

8. Danahy, M. P.; Avaltroni, J. J.; Midwood, K. S.; Schwarzbauer, J. E.; Schwartz, J. Self-Assembled Monolayers of α, ω-Diphosphonic Acids on Ti Enable Complete or Spatially Controlled Surface Derivatization. *Langmuir* **2004,** *20,* 5333-5337.

9. Gawalt, E. S.; Avaltroni, M. J.; Danahy, M. P.; Silverman, B. M.; Hanson, E. L.; Midwood, K. S.; Schwarzbauer, J. E.; Schwartz, J. Bonding Organics to Ti Alloys: Facilitating Human Osteoblast Attachment and Spreading on Surgical Implant Materials. *Langmuir* **2003,** *19,* 200-204.

10. Helmy, R.; Fadeev, A. Y. Self-Assembled Monolayers Supported on TiO_2: Comparison of $C_{18}H_{37}SiX_3$ [X = H, Cl, $OCH_3C_{18}H_{37}Si(CH_3)_2Cl$, and $C_{18}H_{37}PO(OH)_2$]. *Langmuir* **2002,** *18,* 8924-8928.

11.   Hong, H. G.; Sackett, D. D.; Mallouk, T. E. Adsorption of Well-Ordered Zirconium Phosphonate Multilayer Films on High Surface-Area Silica. *Chem. Mater.* **1991,** *3,* 521-527.

12.   Zeppenfeld, A. C.; Fiddler, S. L.; Ham, W. K.; Klopfenstein, B. J.; Page, C. J. Variation of Layer Spacing in Self-Assembled Hafnium-1,10-Decanediylbis(Phosphonate) Multilayers as Determined by Ellipsometry and Grazing Angle X-Ray Diffraction. *J. Am. Chem. Soc.* **1994,** *116,* 9158-9165.

13.   Foster, E. W.; Kearns, G. J.; Goto, S.; Hutchison, J. E. Patterned Gold Nanoparticle Monolayers Assembled on the Oxide of Silicon. *Adv. Mater.* **2005,** *17,* 1542-1545.

14.   Imabayashi, S.: Hobara, D.; Kakiuchi, T. Voltammetric Detection of the Surface Diffusion of Adsorbed Thiolate Molecules in Artificially Phase-Separated Binary Self-Assembled Monolayers on a Au(111) Surface. *Langmuir* **2001,** *17,* 2560-2563.

15.   Houseman, B. T.; Gawalt, E. S.; Mrksich, M. Maleimide-Functionalized Self-Assembled Monolayers for the Preparation of Peptide and Carbohydrate Biochips. *Langmuir* **2003,** *19,* 1522-1531.

16.   Smith, E. A.; Wanat, M. J.; Cheng, Y. F.; Barreira, S. V. P.; Frutos, A. G.; Corn, R. M. Formation, Spectroscopic Characterization, and Application of Sulfhydryl-Terminated Alkanethiol Monolayers for the Chemical Attachment of DNA onto Gold Surfaces. *Langmuir* **2001,** *17,* 2502-2507.

17.   Frey, B. L.; Corn, R. M.; Weibel, S. C. Polarization-Modulation Approaches to Reflection-Absorption Spectroscopy. In *Handbook of Vibrational Spectroscopy;* Chalmers, J. M.; Griffitsh, P. R. Eds. John Wiley & Sons, Ltd.: West Sussex, United Kingdom, 2002; Vol. 2, pp 1042-1057.

18.   Cassie, A. B. D. Contact Angles. *Discuss. Faraday Soc.* **1948,** *3,* 11-16.

19.   Folkers, J. P.; Gorman, C. B.; Laibinis, P. E.; Buchholz, S.; Whitesides, G. M. Self-Assembled Monolayers of Long-Chain Hydroxamic Acids on the Native Oxides of Metals. *Langmuir* **2001,** *11,* 813-824.

20.   Brovelli, D.; Hähner, G.; Ruiz, L.; Hofer, R.; Kraus, G.; Waldner, A.; Schlösser, J.; Oroszlan, P.; Ehrat, M.; Spencer, N. D. Highly Oriented, Self-Assembled Alkanephosphonate Monolyaers on Tantalum(V) Oxide Surfaces. *Langmuir* **1999,** *15,* 4324-4327.

21. Hähner, G.; Klingenfuss, I. Order and Oreintation in Self-Assembled Long Chain Alkanephosphate Monolayers Adsorbed on Metal Oxide Surfaces. *Langmuir* **2001,** *17,* 7047-7052.

22. Clegg, R. S. Structure, Stability, and Electron Transfer Characteristics of Self-Assembled Monolayers Containing Internal Peptide Groups. Ph.D. Dissertation, University of Oregon, Eugene, OR, 1999.

23. (a) Pawsey, S.; Yach, K.; Reven, L. Self-Assembly of Carboxyalkylphosphonic Acids on Metal Oxide Powders. *Langmuir* **2002,** *18,* 5205-5212. (b) Gao, W.; Dickinson, L.; Grozinger, C.; Morin, F. G.; Reven, L. Self-Assembled Monolayers of Alkylphosphonic Acids on Metal Oxides. *Langmuir* **1996,** *12,* 6429-6435.

24. King, D. E. Oxidation of Gold by Ultraviolet Light and Ozone at 25 °C. *J. Vac. Sci. Technol., A* **1995,** *13,* 1247-1253.

25. Laibinis, P. E.; Hickman, J. J.; Wrighton, M. S.; Whitesides, G. M. Orthogonal Self-Assembled Monolayers - Alkanethiols on Gold and Alkane Carboxylic-Acids on Alumina. *Science* **1989,** *245,* 845-847.

CHAPTER III

1. Daniel, M. C.; Astruc, D. Gold Nanoparticles: Assembly, Supramolecular Chemistry, Quantum-Size-Related Properties, and Applications Toward Biology, Catalysis, and Nanotechnology. *Chem. Rev.* **2004,** *104,* 293-346.

2. McConnell, W. P.; Novak, J. P.; Brousseau, L. C.; Fuierer, R. R.; Tenent, R. C.; Feldheim, D. L. Electronic and Optical Properties of Chemically Modified Metal Nanoparticles and Molecularly Bridged Nanoparticle Arrays. *J. Phys. Chem. B* **2000,** *104,* 8925-8930.

3. Pradhan, S.; Sun, J.; Deng, F. J.; Chen, S. W. Single-Electron Transfer in Nanoparticle Solids. *Adv. Mater.* **2006,** *18,* 3279-3283.

4. Schmid, G.; Corain, B. Nanoparticulated Gold: Syntheses, Structures, Electronics, and Reactivities. *Eur. J. Inorg. Chem.* **2003,** *17,* 3081-3098.

5.   Liz-Marzan, L. M. Tailoring Surface Plasmons through the Morphology and Assembly of Metal Nanoparticles. *Langmuir* **2006,** *22,* 32-41.

6.   Maier, S. A.; Brongersma, M. L.; Kik, P. G.; Meltzer, S.; Requicha, A. A. G.; Atwater, H. A. Plasmonics - A Route to Nanoscale Optical Devices. *Adv. Mater.* **2001,** *13,* 1501-1505.

7.   Wilcoxon, J. P.; Abrams, B. L. Synthesis, Structure and Properties of Metal Nanoclusters. *Chem. Soc. Rev.* **2006,** *35,* 1162-1194.

8.   Chen, M. S.; Goodman, D. W. Catalytically Active Gold: From Nanoparticles to Ultrathin Films. *Acc. Chem. Res.* **2006,** *39,* 739-746.

9.   Chen, Y.; Palmer, R. E.; Wilcoxon, J. P. Sintering of Passivated Gold Nanoparticles under the Electron Beam. *Langmuir* **2006,** *22,* 2851-2855.

10.   Haruta, M.; Kobayashi, T.; Sano, H.; Yamada, N. Novel Gold Catalysts for the Oxidation of Carbon Monoxide at a Temperature Far Below 0 °C. *Chem. Lett.* **1987,** *2,* 405-408.

11.   Haruta, M.; Tsubota, S.; Kobayashi, T.; Kageyama, H.; Genet, M. J.; Delmon, B. Low-Temperature Oxidation of CO over Gold Supported on TiO_2, α-Fe_2O_3, and Co_3O_4. *J. Catal.* **1993,** *144,* 175-192.

12.   Hutchings, G. J.; Carrettin, S.; Landon, P.; Edwards, J. K.; Enache, D.; Knight, D. W.; Xu, Y. J.; Carley, A. F. New Approaches to Designing Selective Oxidation Catalysts: Au/C a Versatile Catalyst. *Top. Catal.* **2006,** *38,* 223-230.

13.   Hutchings, G. J.; Hall, M. S.; Carley, A. F.; Landon, P.; Solsona, B. E.; Kiely, C. J.; Herzing, A.; Makkee, M.; Moulijn, J. A.; Overweg, A.; Fierro-Gonzalez, J. C.; Guzman, J.; Gates, B. C. Role of Gold Cations in the Oxidation of Carbon Monoxide Catalyzed by Iron Oxide-Supported Gold. *J. Catal.* **2006,** *242,* 71-81.

14.   Santhanam, V.; Andres, R. P. Microcontact Printing of Uniform Nanoparticle Arrays. *Nano Lett.* **2004,** *4,* 41-44.

15.   Andres, R. P.; Datta, S.; Dorogi, M.; Gomez, J.; Henderson, J. I.; Janes, D. B.; Kolagunta, V. R.; Kubiak, C. P.; Mahoney, W.; Osifchin, R. F.; Reifenberger, R.; Samanta, M. P.; Tian, W. Room Temperature Coulomb Blockade and Coulomb Staircase from Self-Assembled Nanostructures. *J. Vac. Sci. Technol., A* **1996,** *14,* 1178-1183.

16. Klein, D. L.; McEuen, P. L.; Katari, J. E. B.; Roth, R.; Alivisatos, A. P. An Approach to Electrical Studies of Single Nanocrystals. *Appl. Phys. Lett.* **1996,** *68,* 2574-2576.

17. Middleton, A. A.; Wingreen, N. S. Collective Transport in Arrays of Small Metallic Dots. *Phys. Rev. Lett.* **1993,** *71,* 3198-3201.

18. Parthasarathy, R.; Lin, X. M.; Elteto, K.; Rosenbaum, T. F.; Jaeger, H. M. Percolating through Networks of Random Thresholds: Finite Temperature Electron Tunneling in Metal Nanocrystal Arrays. *Phys. Rev. Lett.* **2004,** *92,* 076801.

19. Brown, J. J.; Porter, J. A.; Daghlian, C. P.; Gibson, U. J. Ordered Arrays of Amphiphilic Gold Nanoparticles in Langmuir Monolayers. *Langmuir* **2001,** *17,* 7966-7969.

20. Santhanam, V.; Liu, J.; Agarwal, R.; Andres, R. P. Self-Assembly of Uniform Monolayer Arrays of Nanoparticles. *Langmuir* **2003,** *19,* 7881-7887.

21. Bigioni, T. P.; Lin, X. M.; Nguyen, T. T.; Corwin, E. I.; Witten, T. A.; Jaeger, H. M. Kinetically Driven Self-Assembly of Highly Ordered Nanoparticle Monolayers. *Nature Mater.* **2006,** *5,* 265-270.

22. Parthasarathy, R.; Lin, X. M.; Jaeger, H. M. Electronic Transport in Metal Nanocrystal Arrays: The Effect of Structural Disorder on Scaling Behavior. *Phys. Rev. Lett.* **2001,** *87,* 186807.

23. Foster, E. W.; Kearns, G. J.; Goto, S.; Hutchison, J. E. Patterned Gold-Nanoparticle Monolayers Assembled on the Oxide of Silicon. *Adv. Mater.* **2005,** *17,* 1542-1545.

24. Hong, H. G.; Sackett, D. D.; Mallouk, T. E. Adsorption of Well-Ordered Zirconium Phosphonate Multilayer Films on High Surface-Area Silica. *Chem. Mater.* **1991,** *3,* 521-527.

25. Lochmuller, C. H.; Kersey, M. T. Effect of Thermal Pretreatment on the Surface Reactivity of Amorphous Silica. *Langmuir* **1988,** *4,* 572-578.

26. Hutchison, J. E.; Foster, E. W.; Warner, M. G.; Reed, S. M.; Weare, W. W.; Buhro, W.; Yu, H. Triphenylphosphine-Stabilized Gold Nanoparticles. *Inorg. Synth.* **2004,** *34,* 228-232.

27.   Sweeney, S. F.; Woehrle, G. H.; Hutchison, J. E. Rapid Purification and Size Separation of Gold Nanoparticles via Diafiltration. *J. Am. Chem. Soc.* **2006,** *128,* 3190-3197.

28.   Kearns, G. J.; Foster, E. W.; Hutchison, J. E. Substrates for Direct Imaging of Chemically Functionalized SiO$_2$ Surfaces by Transmission Electron Microscopy. *Anal. Chem.* **2006,** *78,* 298-303.

CHAPTER IV

1.   Brust, M.; Kiely, C. J. Some Recent Advances in Nanostructure Preparation from Gold and Silver Particles: A Short Topical Review. *Colloids Surf., A* **2002,** *202,* 175-186.

2.   Oldenburg, S. J.; Averitt, R. D.; Westcott, S. L.; Halas, N. J. Nanoengineering of Optical Resonances. *Chem. Phys. Lett.* **1998,** *288,* 243-247.

3.   Braun, E.; Eichen, Y.; Sivan, U.; Ben-Yoseph, G. DNA-Templated Assembly and Electrode Attachment of a Conducting Silver Wire. *Nature* **1998,** *391,* 775-778.

4.   Gunter, P. L. J.; Niemantsverdriet, J. W.; Ribeiro, F. H.; Somorjai, G. A. Surface Science Approach to Modeling Supported Catalysts. *Catal. Rev.-Sci. Eng.* **1997,** *39,* 77-168.

5.   Li, Y; Meng, G. W.; Zhang, L. D.; Phillipp, F. Ordered Semiconductor ZnO Nanowire Arrays and Their Photoluminescence Properties. *Appl. Phys. Lett.* **2000,** *76,* 2011-2013.

6.   Lao, J. Y.; Wen, J. G.; Ren, Z. F. Hierarchical ZnO Nanostructures. *Nano Lett.* **2002,** *2,* 1287-1291.

7.   Vayssieres, L. Growth of Arrayed Nanorods and Nanowires of ZnO from Aqueous Solutions. *Adv. Mater.* **2003,** *15,* 464-466.

8.   Yao, B. D.; Chan, Y. F.; Wang, N. Formation of ZnO Nanostructures by a Simple Way of Thermal Evaporation. *Appl. Phys. Lett.* **2002,** *81,* 757-759.

9.   Huang, M. H.; Mao, S.; Feick, H.; Yan, H. Q.; Wu, Y. Y.; Kind, H.; Weber, E.; Russo, R.; Yang, P. D. Room-Temperature Ultraviolet Nanowire Nanolasers. *Science* **2001**, *292*, 1897-1899.

10. Kong, Y. C.; Yu, D. P.; Zhang, B.; Fang, W.; Feng, S. Q. Ultraviolet-Emitting ZnO Nanowires Synthesized by a Physical Vapor Deposition Approach. *Appl. Phys. Lett.* **2001**, *78*, 407-409.

11. Lee, C. J.; Lee, T. J.; Lyu, S. C.; Zhang, Y.; Ruh H.; Lee, H. J. Field Emission from Well-Aligned Zinc Oxide Nanowires Grown at Low Temperature. *Appl. Phys. Lett.* **2002**, *81*, 3648-3650.

12. Ng, H. T.; Han, J.; Yamada, T.; Nguyen, P.; Chen, Y. P.; Meyyappan, M. Single Crystal Nanowire Vertical Surround-Gate Field-Effect Transistor. *Nano Lett.* **2004**, *4*, 1247-1252.

13. Arnold, M. S.; Avouris, P.; Pan, Z. W.; Wang, Z. L. Field-Effect Transistors Based on Single Semiconducting Oxide Nanobelts. *J. Phys. Chem. B* **2003**, *107*, 659-663.

14. Johnson, J. C.; Knutsen, K. P.; Yan, H. Q.; Law, M.; Zhang, Y. F.; Yang, P. D.; Saykally, R. J. Ultrafast Carrier Dynamics in Single ZnO Nanowire and Nanoribbon Lasers. *Nano Lett.* **2004**, *4*, 197-204.

15. Bai, X. D.; Wang, E. G.; Gao, P. X.; Wang, Z. L. Measuring the Work Function at a Nanobelt Tip and at a Nanoparticle Surface. *Nano Lett.* **2003**, *3*, 1147-1150.

16. Park, J. Y.; Yun, Y. S.; Hong, Y. S.; Oh, H.; Kim, J. J.; Kim, S. S. Synthesis, Electrical and Photoresponse Properties of Vertically Well-Aligned and Epitaxial ZnO Nanorods on GaN-Buffered Sapphire Substrates. *Appl. Phys. Lett.* **2005**, *87*, 123108.

17. Zhang, Y.; Jia, H. B.; Wang, R. M.; Chen, C. P.; Luo, X. H.; Yu, D. P.; Lee, C. J. Low-Temperature Growth and Raman Scattering Study of Vertically Aligned ZnO Nanowires on Si Substrate. *Appl. Phys. Lett.* **2003**, *83*, 4631-4633.

18. Greene, L. E.; Law, M.; Tan, D. H.; Montano, M.; Goldberger, J.; Somorjai, G.; Yang, P. D. General Route to Vertical ZnO Nanowire Arrays Using Textured ZnO Seeds. *Nano Lett.* **2005**, *5*, 1231-1236.

19. Wang, X. D.; Summers, C. J.; Wang, Z. L. Large-Scale Hexagonal-Patterned Growth of Aligned ZnO Nanorods for Nano-Optoelectronics and Nanosensor Arrays. *Nano Lett.* **2004**, *4*, 423-426.

20. Kim, S. W.; Fujita, S.; Fujita, S. ZnO Nanowires with High Aspect Ratios Grown by Metalorganic Chemical Vapor Deposition Using Gold Nanoparticles. *Appl. Phys. Lett.* **2005,** *86,* 153119.

21. Weare, W. W.; Reed, S. M.; Warner, M. G.; Hutchison, J. E. Improved Synthesis of Small ($d_{core} \approx$ 1.5 nm) Phosphine-Stabilized Gold Nanoparticles *J. Am. Chem. Soc.* **2000,** *122,* 12890-12891.

22. Hutchison, J. E.; Foster, E. W.; Warner, M. G.; Reed, S. M.; Weare, W. W.; Buhro, W.; Yu, H. Triphenylphosphine-Stabilized Gold Nanoparticles. *Inorg. Synth.* **2004,** *34,* 228-232.

23. Sweeney, S. F.; Woehrle, G. H.; Hutchison, J. E. Rapid Purification and Size Separation of Gold Nanoparticles via Diafiltration. *J. Am. Chem. Soc.* **2006,** *128,* 3190-3197.

24. Kamalasanan, M. N.; Chandra, S. Sol-Gel Synthesis of ZnO Thin Films. *Thin Solid Films* **1996,** *288,* 112-115.

25. Ip, K.; Gila, B. P.; Onstine, A. H.; Lambers, E. S.; Heo, Y. W.; Baik, K. H.; Norton, D. P.; Pearton, S. J.; Kim, S.; LaRoche, J. R.; Ren, F. Improved Pt/Au and W/Pt/Au Schottky Contacts on n-Type ZnO Using Ozone Cleaning. *Appl. Phys. Lett.* **2004,** *84,* 5133-5135.

26. Foster, E. W.; Kearns, G. J.; Goto, S.; Hutchison, J. E. Patterned Gold-Nanoparticle Monolayers Assembled on the Oxide of Silicon. *Adv. Mater.* **2005,** *17,* 1542-1545.

27. Brewer, S. H.; Brown, D. A.; Franzen, S. Formation of Thiolate and Phosphonate Adlayers on Indium Tin Oxide: Optical and Electronic Characterization. *Langmuir* **2002,** *18,* 6857-6865.

28. Gardner, T. J.; Frisbie, C. D.; Wrighton, M. S. Systems for Orthogonal Self-Assembly of Electroactive Monolayers on Au and ITO - An Approach to Molecular Electronics. *J. Am. Chem. Soc.* **1995,** *117,* 6927-6933.

29. Gao, W.; Dickinson, L.; Grozinger, C.; Morin, F. G.; Reven, L. Self-Assembled Monolayers of Alkylphosphonic Acids on Metal Oxides. *Langmuir* **1996,** *12,* 6429-6435.

30. Gawalt, E. S.; Avaltroni, M. J.; Koch, N.; Schwartz, J. Self-Assembly and Bonding of Alkanephosphonic Acids on the Native Oxide Surface of Titanium. *Langmuir* **2001,** *17,* 5736-5738.

31.   Raman, A.; Dubey, M.; Gouzman, I.; Gawalt, E. S. Formation of Self-Assembled Monolayers of Alkylphosphonic Acid on the Native Oxide Surface of SS316L. *Langmuir* **2006,** *22,* 6469-6472.

32.   Zeppenfeld, A. C.; Fiddler, S. L.; Ham, W. K.; Klopfenstein, B. J.; Page, C. J. Variation of Layer Spacing in Self-Assembled Hafnium-1,10-Decanediylbis(Phosphonate) Multilayers as Determined by Ellipsometry and Grazing Angle X-Ray Diffraction. *J. Am. Chem. Soc.* **1994,** *116,* 9158-9165.

CHAPTER V

1.   Ulman, A. *An Introduction to Ultrathin Organic Films: From Langmuir-Blodgett to Self-Assembly.* Academic Press: San Diego, CA, 1991; p 442.

2.   Chen, Y.; Palmer, R. E.; Wilcoxon, J. P. Sintering of Passivated Gold Nanoparticles under the Electron Beam. *Langmuir* **2006,** *22,* 2851-2855.

3.   Haruta, M.; Tsubota, S.; Kobayashi, T.; Kageyama, H.; Genet, M. J.; Delmon, B. Low-Temperature Oxidation of CO over Gold Supported on TiO_2, α-Fe_2O_3, and Co_3O_4. *J. Catal.* **1993,** *144,* 175-192.

4.   Hutchings, G. J.; Carrettin, S.; Landon, P.; Edwards, J. K.; Enache, D.; Knight, D. W.; Xu, Y. J.; Carley, A. F. New Approaches to Designing Selective Oxidation Catalysts: Au/C a Versatile Catalyst. *Top. Catal.* **2006,** *38,* 223-230.

5.   Klein, D. L.; McEuen, P. L.; Katari, J. E. B.; Roth, R.; Alivisatos, A. P. An Approach to Electrical Studies of Single Nanocrystals. *Appl. Phys. Lett.* **1996,** *68,* 2574-2576.

6.   Lebreton, C.; Vieu, C.; Pepin, A.; Mejias, M.; Carcenac, F.; Jin, Y.; Launois, H. Coulomb Blockade Effect through a 2D Ordered Array of Pd Islands Obtained by Colloidal Deposition. *Microelectron. Eng.* **1998,** *41,* 507-510.

7.   Pradhan, S.; Sun, J.; Deng, F. J.; Chen, S. W. Single-Electron Transfer in Nanoparticle Solids. *Adv. Mater.* **2006,** *18,* 3279-3283.

8.   Maier, S. A.; Brongersma, M. L.; Kik, P. G.; Meltzer, S.; Requicha, A. A. G.; Atwater, H. A. Plasmonics - A Route to Nanoscale Optical Devices. *Adv. Mater.* **2001,** *13,* 1501-1505.

9. McConnell, W. P.; Novak, J. P.; Brousseau, L. C.; Fuierer, R. R.; Tenent, R. C.; Feldheim, D. L. Electronic and Optical Properties of Chemically Modified Metal Nanoparticles and Molecularly Bridged Nanoparticle Arrays. *J. Phys. Chem. B* **2000,** *104,* 8925-8930.

10. Chen, C.-C.; Tsai, C.-Y.; Ko, F.-H.; Pun, C.-C.; Chen, H.-L.; Chen, P.-H. Room Temperature Operation of a Coulomb Blockade Sensor Fabricated by Self-Assembled Gold Nanoparticles using Deoxyribonucleic Acid Hybridization. *Jpn. J. Appl. Phys.* **2004,** *43,* 3843-3848.

11. Nath, N.; Chilkoti, A. A Colorimetric Gold Nanoparticle Sensor to Interrogate Biomolecular Interactions in Real Time on a Surface. *Anal. Chem.* **2002,** *74,* 504-509.

12. Olofsson, L.; Rindzevicius, T.; Pfeiffer, I.; Kall, M.; Hook, F. Surface-Based Gold-Nanoparticle Sensor for Specific and Quantitative DNA Hybridization Detection. *Langmuir* **2003,** *19,* 10414-10419.

13. Ito, D.; Jespersen, M. L.; Hutchison, J. E. Selective Growth of Vertical Zinc Oxide Nanowire Arrays Using Chemically Anchored Gold Nanoparticles. *Manuscript in preparation* **2007**.

14. Menard, L. D.; Xu, F. T.; Nuzzo, R. G.; Yang, J. C. Preparation of TiO_2-Supported Au Nanoparticle Catalysts from a Au_{13} Cluster Precursor: Ligand Removal Using Ozone Exposure Versus a Rapid Thermal Treatment. *J. Catal.* **2006,** *243,* 64-73.

15. Ono, L. K.; Roldan-Cuenya, B. Effect of Interparticle Interaction on the Low Temperature Oxidation of CO over Size-Selected Au Nanocatalysts Supported on Ultrathin TiC Films. *Catal. Lett.* **2007,** *113,* 86-94.

16. Woehrle, G. H.; Brown, L. O.; Hutchison, J. E. Thiol-Functionalized, 1.5-nm Gold Nanoparticles through Ligand Exchange Reactions: Scope and Mechanism of Ligand Exchange. *J. Am. Chem. Soc.* **2005,** 127, 2172-2183.

17. Hutchison, J. E.; Foster, E. W.; Warner, M. G.; Reed, S. M.; Weare, W. W.; Buhro, W.; Yu, H. Triphenylphosphine-Stabilized Gold Nanoparticles. *Inorg. Synth.* **2004,** 34, 228-232.

18. Petroski, J.; Chou, M. H.; Creutz, C. Rapid Phosphine Exchange on 1.5-nm Gold Nanoparticles. *Inorg. Chem.* **2004,** *43,* 1597-1599.

19.   Weare, W. W.; Reed, S. M.; Warner, M. G.; Hutchison, J. E. Improved Synthesis of Small (d_{core} ≈1.5 nm) Phosphine-Stabilized Gold Nanoparticles. *J. Am. Chem. Soc.* **2000**, *122*, 12890-12891.

20.   Brown, L. O.; Hutchison, J. E. Controlled Growth of Gold Nanoparticles During Ligand Exchange. *J. Am. Chem. Soc.* **1999**, 121, 882-883.

21.   Brown, L. O.; Hutchison, J. E. Convenient Preparation of Stable, Narrow-Dispersity Gold Nanocrystals by Ligand Exchange Reactions. *J. Am. Chem. Soc.* **1997**, *119*, 12384-12385.

22.   Brust, M.; Fink, J.; Bethell, D.; Schiffrin, D. J.; Kiely, C. Synthesis and Reactions of Functionalized Gold Nanoparticles. *J. Chem. Soc., Chem. Commun.* **1995**, *16*, 1655-1656.

23.   Hostetler, M. J.; Green, S. J.; Stokes, J. J.; Murray, R. W. Monolayers in Three Dimensions: Synthesis and Electrochemistry of ω-Functionalized Alkanethiolate-Stabilized Gold Cluster Compounds. *J. Am. Chem. Soc.* **1996**, *118*, 4212-4213.

24.   Brust, M.; Walker, M.; Bethell, D.; Schiffrin, D. J.; Whyman, R. Synthesis of Thiol-Derivatized Gold Nanoparticles in a 2-Phase Liquid-Liquid System. *J. Chem. Soc., Chem. Commun.* **1994**, *7*, 801-802.

25.   Templeton, A. C.; Wuelfing, M. P.; Murray, R. W. Monolayer Protected Cluster Molecules. *Acc. Chem. Res.* **2000**, *33*, 27-36.

26.   Lee, K. J.; Lee, Y. I.; Shim, I. K.; Joung, J.; Oh, Y. S. Direct Synthesis and Bonding Origins of Monolayer-Protected Silver Nanocrystals from Silver Nitrate through in situ Ligand Exchange. *J. Colloid Interface Sci.* **2006**, *304*, 92-97.

27.   Foster, E. W.; Kearns, G. J.; Goto, S.; Hutchison, J. E. Patterned Gold-Nanoparticle Monolayers Assembled on the Oxide of Silicon. *Adv. Mater.* **2005**, *17*, 1542-1545.

28.   Warner, M. G.; Hutchison, J. E. Linear Assemblies of Nanoparticles Electrostatically Organized on DNA Scaffolds. *Nature Mater.* **2003**, *2*, 272-277.

29.   Woehrle, G. H.; Warner, M. G.; Hutchison, J. E. Molecular-Level Control of Feature Separation in One-Dimensional Nanostructure Assemblies Formed by Biomolecular Nanolithography. *Langmuir* **2004**, *20*, 5982-5988.

30.   Xu, H.; Hong, R.; Wang, X.; Arvizo, R.; You, C.; Samanta, B.; Patra, D.; Tuominen, M. T.; Rotello, V. M. Controlled Formation of Patterned Gold Films via Site-Selective Deposition of Nanoparticles onto Polymer-Templated Surfaces. *Adv. Mater.* **2007,** 19, 1383-1386.

31.   Chidsey, C. E. D.; Bertozzi, C. R.; Putvinski, T. M.; Mujsce, A. M. Coadsorption of Ferrocene-Terminated and Unsubstituted Alkanethiols on Gold - Electroactive Self-Assembled Monolayers. *J. Am. Chem. Soc.* **1990,** *112,* 4301-4306.

32.   Collard, D. M.; Fox, M. A. Use of Electroactive Thiols to Study the Formation and Exchange of Alkanethiol Monolayers on Gold. *Langmuir* **1991,** *7,* 1192-1197.

33.   Baralia, G. G.; Duwez, A. S.; Nysten, B.; Jonas, A. M. Kinetics of Exchange of Alkanethiol Monolayers Self-assembled on Polycrystalline Gold. *Langmuir* **2005,** *21,* 6825-6829.

34.   Lin, P. H.; Guyot-Sionnest, P. Replacement of Self-Assembled Monolayers of Di(phenylethynyl)benzenethiol on Au(111) by *n*-Alkanethiols. *Langmuir* **1999,** *15,* 6825-6828.

35.   Guo, R.; Song, Y.; Wang, G. L.; Murray, R. W. Does Core Size Matter in the Kinetics of Ligand Exchanges of Monolayer-Protected Au Clusters? *J. Am. Chem. Soc.* **2005,** *127,* 2752-2757.

36.   Kassam, a.; Bremner, G.; Clark, B.; Ulibarri, G.; Lennox, R. B. Place Exchange Reactions of Alkyl Thiols on Gold Nanoparticles. *J. Am. Chem. Soc.* **2006,** *128,* 3476-3477.

37.   Jespersen, M. L.; Foster, E. W.; Hutchison, J. E. Surface Modification Strategy for the Formation of Extended, High-Density Gold Nanoparticle Monolayers on Thermally Grown Silicon Dioxide. *Manuscript in preparation* **2008.**

38.   Brown, J. J.; Porter, J. A.; Daghlian, C. P.; Gibson, U. J. Ordered Arrays of Amphiphilic Gold Nanoparticles in Langmuir Monolayers. *Langmuir* **2001,** *17,* 7966-7969.

39.   Santhanam, V.; Andres, R. P. Microcontact Printing of Uniform Nanoparticle Arrays. *Nano Lett.* **2004,** *4,* 41-44.

40.   Santhanam, V.; Liu, J.; Agarwal, R.; Andres, R. P. Self-Assembly of Uniform Monolayer Arrays of Nanoparticles. *Langmuir* **2003,** *19,* 7881-7887.

41.   Bigioni, T. P.; Lin, X. M.; Nguyen, T. T.; Corwin, E. I.; Witten, T. A.; Jaeger, H. M. Kinetically Driven Self-Assembly of Highly Ordered Nanoparticle Monolayers. *Nature Mater.* **2006,** *5,* 265-270.

42.   Parthasarathy, R.; Lin, X. M.; Jaeger, H. M. Electronic Transport in Metal Nanocrystal Arrays: The Effect of Structural Disorder on Scaling Behavior. *Phys. Rev. Lett.* **2001,** *87,* 186807.

43.   Cui, Y.; Bjork, M. T.; Liddle, J. A.; Sonnichsen, C.; Boussert, B.; Alivisatos, A. P. Integration of Colloidal Nanocrystals into Lithographically Patterned Devices. *Nano Lett.* **2004,** *4,* 1093-1098.

44.   Sweeney, S. F.; Woehrle, G. H.; Hutchison, J. E. Rapid Purification and Size Separation of Gold Nanoparticles via Diafiltration. *J. Am. Chem. Soc.* **2006,** *128,* 3190-3197.

45.   Kearns, G. J.; Foster, E. W.; Hutchison, J. E. Substrates for Direct Imaging of Chemically Functionalized SiO_2 Surfaces by Transmission Electron Microscopy. *Anal. Chem.* **2006,** *78,* 298-303.

46.   Cassie, A. B. D. Contact Angles. *Discuss. Farady Soc.* **1948,** *3,* 11-16.

47.   Woehrle, G. H.; Hutchison, J. E.; Ozkar, S.; Finke, R. G. Analysis of Nanoparticle Transmission Electron Microscopy Data Using a Public-Domain Image-Processing Program, Image. *Turk. J. Chem.* **2006,** *30,* 1-13.

48.   Laibinis, P. E.; Whitesides, G. M.; Allara, D. L.; Tao, Y. T.; Parikh, A. N.; Nuzzo, R. G. Comparison of the Structures and Wetting Properties of Self-Assembled Monolayers of Normal-Alkanethiols on the Coinage Metal Surfaces, Cu, Ag, Au. *J. Am. Chem. Soc.* **1991,** *113,* 7152-7167.

49.   Porter, M. D.; Bright, T. B.; Allara, D. L.; Chidsey, C. E. D. Spontaneously Organized Molecular Assemblies. 4. Structural Characterization of Normal-Alkyl Thiol Monolayers on Gold by Optical Ellipsometry, Infrared-Spectroscopy, and Electrochemistry. *J. Am. Chem. Soc.* **1987,** *109,* 3559-3568.

CHAPTER VI

1.   Haruta, M.; Kobayashi, T.; Sano, H.; Yamada, N. Novel Gold Catalysts for the Oxidation of Carbon Monoxide at a Temperature Far Below 0 °C. *Chem. Lett.* **1987,** *2,* 405-408.

2.   Haruta, M.; Tsubota, S.; Kobayashi, T.; Kageyama, H.; Genet, M. J.; Delmon, B. Low-Temperature Oxidation of CO over Gold Supported on TiO_2, α-Fe_2O_3, and Co_3O_4. *J. Catal.* **1993,** *144,* 175-192.

3.   Haruta, M.; Yamada, N.; Kobayashi, T.; Iijima, S. Gold Catalysts Prepared by Coprecipitation for Low-Temperature Oxidation of Hydrogen and of Carbon Monoxide. *J. Catal.* **1989,** *115,* 301-309.

4.   Enache, D. I.; Edwards, J. K.; Landon, P.; Solsona-Espriu, B.; Carley, A. F.; Herzing, A. A.; Watanabe, M.; Kiely, C. J.; Knight, D. W.; Hutchings, G. J. Solvent-Free Oxidation of Primary Alcohols to Aldehydes Using Au-Pd/TiO_2 Catalysts. *Science* **2006,** *311,* 362-365.

5.   Sinha, A. K.; Seelan, S.; Tsubota, S.; Haruta, M. Catalysis by Gold Nanoparticles: Epoxidation of Propene. *Top. Catal.* **2004,** *29,* 95-102.

6.   Sinha, A. K.; Seelan, S.; Tsubota, S.; Haruta, M. A Three-Dimensional Mesoporous Titanosilicate Support for Gold Nanoparticles: Vapor-Phase Epoxidation of Propene with High Conversion. *Angew. Chem., Int. Ed. Engl.* **2004,** *43,* 1546-1548.

7.   Claus, P. Heterogeneously Catalysed Hydrogenation Using Gold Catalysts. *Appl. Catal., A* **2005,** *291,* 222-229.

8.   Corma, A.; Serna, P. Chemoselective Hydrogenation of Nitro Compounds with Supported Gold Catalysts. *Science* **2006,** *313,* 332-334.

9.   Debeila, M. A.; Coville, N. J.; Scurrell, M. S.; Hearne, G. R. The Effect of Calcination Temperature on the Adsorption of Nitric Oxide on Au-TiO_2: DRIFTS Studies. *Appl. Catal., A* **2006,** *297,* 247-247.

10. Ueda, A.; Oshima, T.; Haruta, M. Reduction of Nitrogen Monoxide with Propene in the Presence of Oxygen and Moisture over Gold Supported on Metal Oxides. *Appl. Catal., B* **1997,** *12,* 81-93.

11. Haruta, M. Catalysis and Applications of Gold Nanoparticles. *Sci. Technol. Catal.* **2003,** *145,* 31-38.

12. Hutchings, G. J.; Carrettin, S.; Landon, P.; Edwards, J. K.; Enache, D.; Knight, D. W.; Xu, Y. J.; Carley, A. F. New Approaches to Designing Selective Oxidation Catalysts: Au/C a Versatile Catalyst. *Top. Catal.* **2006,** *38,* 223-230.

13. Schmid, G.; Corain, B. Nanoparticulated Gold: Syntheses, Structures, Electronics, and Reactivities. *Eur. J. Inorg. Chem.* **2003,** *17,* 3081-3098.

14. Yan, W. F.; Chen, B.; Mahurin, S. M.; Schwartz, V.; Mullins, D. R.; Lupini, A. R.; Pennycook, S. J.; Dai, S.; Overbury, S. H. Preparation and Comparison of Supported Gold Nanocatalysts on Anatase, Brookite, Rutile, and P25 Polymorphs of TiO_2 for Catalytic Oxidation of CO. *J. Phys. Chem. B* **2005,** *109,* 10676-10685.

15. Pietron, J. J.; Stroud, R. M.; Rolison, D. R. Using Three Dimensions in Catalytic Mesoporous Nanoarchitectures. *Nano Lett.* **2002,** *2,* 545-549.

16. Guzman, J.; Gates, B. C. Catalysis by Supported Gold: Correlation between Catalytic Activity for CO Oxidation and Oxidation States of Gold. *J. Am. Chem. Soc.* **2004,** *126,* 2672-2673.

17. Campbell, C. T.; Parker, S. C.; Starr, D. E. The Effect of Size-Dependent Nanoparticle Energetics on Catalyst Sintering. *Science* **2002,** *298,* 811-814.

18. Haruta, M. Size- and Support-Dependency in the Catalysis of Gold. *Catal. Today* **1997,** *36,* 153-166.

19. Lee, S. S.; Fan, C. Y.; Wu, T. P.; Anderson, S. L. CO Oxidation on Au-*n*/TiO$_2$ Catalysts Produced by Size-Selected Cluster Deposition. *J. Am. Chem. Soc.* **2004,** *126,* 5682-5683.

20. Lim, D. C.; Lopez-Salido, I.; Dietsche, R.; Bubek, M.; Kim, Y. D. Electronic and Chemical Properties of Supported Au Nanoparticles. *Chem. Phys.* **2006,** *330,* 441-448.

21. Valden, M.; Lai, X.; Goodman, D. W. Onset of Catalytic Activity of Gold Clusters on Titania with the Appearance of Nonmetallic Properties. *Science* **1998,** *281,* 1647-1650.

22. Akita, T.; Lu, P.; Ichikawa, S.; Tanaka, K.; Haruta, M. Analytical TEM Study on the Dispersion of Au Nanoparticles in Au/TiO$_2$ Catalyst Prepared under Various Temperatures. *Surf. Interface Anal.* **2001,** *31,* 73-78.

23.   Meyer, R.; Lemire, C.; Shaikhutdinov, S. K.; Freund, H. Surface Chemistry of Catalysis by Gold. *Gold Bulletin* **2004,** *37,* 72.

24.   Zheng, N. F.; Stucky, G. D. A General Synthetic Strategy for Oxide-Supported Metal Nanoparticle Catalysts. *J. Am. Chem. Soc.* **2006,** *128,* 14278-14280.

25.   Cho, A. Connecting the Dots to Custom Catalysts. *Science* **2003,** *299,* 1684-1685.

26.   Worley, C. G.; Linton, R. W. Removing Sulfur from Gold Using Ultraviolet/Ozone Cleaning. *J. Vac. Sci. Technol., A.* **1995,** *13,* 2281-2284.

27.   King, D. E. Oxidation of Gold by Ultraviolet Light and Ozone at 25 °C. *J. Vac. Sci. Technol., A.* **1995,** *13,* 1247-1253.

28.   Huang, J. Y.; Dahlgren, D. A.; Hemminger, J. C. Photopatterning of Self-Assembled Alkanethiolate Monolayers on Gold - A Simple Monolayer Photoresist Utilizing Aqueous Chemistry. *Langmuir* **1994,** *10,* 626-628.

29.   Tarlov, M. J.; Burgess, D. R. F.; Gillen, G. UV Photopatterning of Alkanethiolate Monolayers Self-Assembled on Gold and Silver. *J. Am. Chem. Soc.* **1993,** *115,* 5305-5306.

30.   Huang, J. Y.; Hemminger, J. C., Photooxidation of Thiols in Self-Assembled Monolayers on Gold. *J. Am. Chem. Soc.* **1993,** *115,* 3342-3343.

31.   Menard, L. D.; Xu, F. T.; Nuzzo, R. G.; Yang, J. C. Preparation of TiO_2-Supported Au Nanoparticle Catalysts from a Au_{13} Cluster Precursor: Ligand Removal Using Ozone Exposure Versus a Rapid Thermal Treatment. *J. Catal.* **2006,** *243,* 64-73.

32.   Helmy, R.; Fadeev, A. Y. Self-Assembled Monolayers Supported on TiO_2: Comparison of $C_{18}H_{37}SiX_3$ [X = H, Cl, $OCH_3C_{18}H_{37}Si(CH_3)_2Cl$, and $C_{18}H_{37}PO(OH)_2$]. *Langmuir* **2002,** *18,* 8924-8928.

33.   Lee, H.; Kepley, L. J.; Hong, H. G.; Mallouk, T. E. Inorganic Analogs of Langmuir-Blodgett Films - Adsorption of Ordered Zirconium 1,10-Decanebisphosphonate Multilayers on Silicon Surfaces. *J. Am. Chem. Soc.* **1988,** *110,* 618-620.

34. Yee, C.; Kataby, G.; Ulman, A.; Prozorov, T.; White, H.; King, A.; Rafailovich, M.; Sokolov, J.; Gedanken, A. Self-Assembled Monolayers of Alkanesulfonic and -Phosphonic Acids on Amorphous Iron Oxide Nanoparticles. *Langmuir* **1999,** *15,* 7111-7115.

35. Foster, E. W.; Kearns, G. J.; Goto, S.; Hutchison, J. E. Patterned Gold-Nanoparticle Monolayers Assembled on the Oxide of Silicon. *Adv. Mater.* **2005,** 17, 1542-1545.

36. Jespersen, M. L.; Foster, E. W.; Hutchison, J. E. Surface Modification Strategy for the Self-Assembly of Extended, High-Density Gold Nanoparticle Monolayers on Thermally Grown Silicon Dioxide. *Manuscript in preparation* **2008.**

37. Hutchison, J. E.; Foster, E. W.; Warner, M. G.; Reed, S. M.; Weare, W. W.; Buhro, W.; Yu, H. Triphenylphosphine-Stabilized Gold Nanoparticles. *Inorg. Synth.* **2004,** *34,* 228-232.

38. Sweeney, S. F.; Woehrle, G. H.; Hutchison, J. E. Rapid Purification and Size Separation of Gold Nanoparticles via Diafiltration. *J. Am. Chem. Soc.* **2006,** *128,* 3190-3197.

39. Kearns, G. J.; Foster, E. W.; Hutchison, J. E. Substrates for Direct Imaging of Chemically Functionalized SiO_2 Surfaces by Transmission Electron Microscopy. *Anal. Chem.* **2006,** *78,* 298-303.

APPENDIX B

1. Foster, E. W. Self-Assembly of Extended, High-Density Gold Nanoparticle Monolayers on Silicon Dioxide. Ph.D. Dissertation. University of Oregon, Eugene, Oregon, 2006.

2. Hong, H. G.; Sackett, D. D.; Mallouk, T. E. Adsorption of Well-Ordered Zirconium Phosphonate Multilayer Films on High Surface Area Silica. *Chem. Mater.* **1991,** *3,* 521-527.

3. Hutchison, J. E.; Foster, E. W.; Warner, M. G.; Reed, S. M.; Weare, W. W.; Buhro, W.; Yu, H. Triphenylphosphine-Stabilized Gold Nanoparticles. *Inorg. Synth.* **2004,** *34,* 228-232.

4.   Sweeney, S. F.; Woehrle, G. H.; Hutchison, J. E. Rapid Purification and Size Separation of Gold Nanoparticles via Diafiltration. *J. Am. Chem. Soc.* **2006,** *128,* 3190-3197.

5.   Wolf, S.; Tauber, R. N. *Silicon Processing for the VLSI Era*; 2nd ed.; Lattice Press: Sunset Beach, CA, 2000; Vol. 1.